Lasing and strong coupling in inorganic and organic photonic structures

Dissertation

zur Erlangung des akademischen Grades

doctor rerum naturalium
(Dr. rer. nat.)

im Fach Physik
Spezialisierung: Experimentalphysik

eingereicht an der

Mathematisch-Naturwissenschaftlichen Fakultät

der Humboldt-Universität zu Berlin

von

Dipl.-Phys. Michael Höfner

Präsident der Humboldt-Universität zu Berlin:
Prof. Dr. Jan-Hendrik Olbertz

Dekan der Mathematisch-Naturwissenschaftlichen Fakultät:
Prof. Dr. Elmar Kulke

Gutachter/innen:

1. Prof. Dr. Oliver Benson
2. Dr. Hans-Jürgen Wünsche
3. Prof. Dr. Marius Grundmann

eingereicht am: 13.10.2015

Tag der mündlichen Prüfung: 25.01.2016

Abstract

This thesis presents the investigation of strong coupling and lasing in structures using ZnO, ZnCdO or organic molecules as active material. The ZnCdO based multi quantum well structures reach the lasing threshold by using scattering at air holes as the optical feedback. Such emitters are called random lasers. The dynamics of their emission under quasi-stationary condition is the point of interest presented. Highly reproducible excitations are used to investigate the single shot dynamics and their shot to shot differences. The experimental data is qualitatively reproduced by numerical simulation and interpreted by means of network theory.

The more common optical feedback by a cavity is applied in the investigation of the molecule L4P and its spiro-derivatives. Using two identical SiO_2/ZrO_2 based Bragg reflectors surrounding an active layer of L4P-SP2 in a polymer matrix of approximately 12 microns thickness reached single mode lasing (weak coupling). Reducing the active layer thickness to half the resonance wavelength pushes the system into the strong coupling regime. Angular resolved reflectivity shows the anticrossing of the tuned cavity resonance to two vibronic transitions of the molecule. The Rabi-splitting to both vibronic resonances reaches around 90 meV. The energetic position in resonance to ZnO makes this molecule a promising candidate for a hybrid inorganic/organic microcavity in the strong coupling regime.

This is used in a partially epitaxially grown microcavity composed of a ZnMgO based Bragg reflector (alternating layers of different Mg content) and six quantum wells. This is followed by a spincoated layer of L4P in a polymer matrix. The cavity is finished by a dielectric mirror. Low temperature reflectivity shows a clear anticrossing reaching an equal mixing of all resonances for the middle branch.

Zusammenfassung

Diese Arbeit beschäftigt sich mit der Untersuchung der starken Kopplung und Laseremission in Strukturen, die ZnO, ZnCdO oder organische Moleküle als aktives Material enthalten. Die ZnCdO basierten Vielfachquantengräben erreichen ihre Laserschwelle durch optische Ruckkopplung an streuenden Luftlöchern. Diese Emitter nennt man random laser. Die Dynamik ihrer Emission unter quasi-stationären Bedingungen ist der hier gezeigte Fokus. Hoch reproduzierbare Anregungen werden verwendet um sowohl die Dynamik eines einzelnen Beschusses aber auch die Unterschiede verschiedener Anregungen zu untersuchen. Die experimentellen Daten werden durch numerische Simulation qualitativ reproduziert und mit Methoden der Netzwerktheorie interpretiert.

Die verbreitetere optische Rückkopplung durch einen Resonator wird in der Untersuchung des Moleküls L4P und seiner Spiro-derivate benutzt. Zwei identische Braggspiegel umschließen die aktive Schicht aus L4P-SP2, das in eine Polymermatrix eingebettet ist, eine Dicke von 12 Mikrometer hat und in einer einzelnen Mode lasert (schwache Kopplung). Durch Verringerung der aktiven Schicht auf die Hälfte der Resonanzwellenlänge wird das System in den Bereich der starken Kopplung gebracht. Eine Rabi-Aufspaltung von 90 meV wird zu beiden vibronischen Resonanzen beobachtet. Die energetische Position in Resonanz zu ZnO macht dieses Molekül zu einem guten Kandidaten für die Fertigung einer hybriden Mikrokavität im Bereich der starken Kopplung.

Dies wurde in einer teilweise epitaktisch gewachsenen Mikrokavität angewandt, die aus einem ZnMgO basierten Braggspiegel und sechs Quantengräben besteht. Darauf folgt eine aufgeschleuderte Schicht von L4P in der Polymermatrix. Der Resonator wird mit einem dielektrischen Spiegel fertiggestellt. Tieftemperatur Reflektion zeigt eine deutlichen ausweichen und eine gleichverteilte Mischung der drei Resonanz im mittleren Polaritonzweig.

Contents

1 Introduction

The daily use of semiconductor based optoelectronics has influenced our life dramatically. By far the greatest innovation was introduced by the optically based data networks forming the internet. Remote controls, optical disc drives and hand-held electronic devices, like digital cameras and mobile phones, are all based on optoelectronic devices. Especially the latter have a fast pace of incorporating new technology into consumer devices. One example of such a new technology is the organic light emitting diode (OLED) used in digital displays. Simultaneously in the field of communication, the modulation of electrically pumped photon emitters brings the data transfer rates higher and higher.

Many of these optical devices use a wide variety of resonators. The success of resonator based optoelectronics started with the proposal that an emitter's properties could be influenced by the field distribution inside a cavity. This was already suggested by Purcell in 1946 [1]. The emission rate of an emitter can be enhanced or suppressed by placing it in a cavity. However, the real breakthrough of the resonator was achieved by the creation of the first laser by T. Maiman in 1960 [2]. During the investigation of this new light source the resonator was a point of design. Different active materials and the tuning of their emission characteristics were the driving force behind resonator development. With time, research focus has shifted from understanding the influence of the optical feedback on the spectral and temporal characteristics of the emission to the general question whether only the resonator mirrors can provide such a feedback.

In 1966 Letokhov predicted that scattering processes could also result in optical feedback. This was practically proven in 1986 by Makushev et al. [3]. From there on, many active materials have been shown to emit coherent light, when scattering feedback is provided. The low production cost of emitters, which only need an active material with scattering centres, made it a promising field of research. In classical laser systems a carefully fabricated cavity will cause a certain electro-magnetic field distribution, called modes, which means it will influence the emission wavelength and directionality. By using scattering feedback the mostly random position and distance will characterize the emission, reducing the directionality and result in a random spectral mode separation. This is the reason such a system is called a random laser. Their emission is characterized by wide divergence [4] and low spacial coherence [5]. In general, scattering is intrinsic to many materials, which appear opaque or white. Many transparent materials, like for example glass, will appear white if it is milled to a powder, increasing the number of scattering processes. In the investigation presented later, the density of scattering centres is still so low, that the sample looks still mostly transparent in ambient conditions.

Until the present day these random lasers have their appliance in specialized fields, where their emission characteristics are beneficial. While a wide range of time-integrated

investigations were focussed on the spectral characteristics and threshold behaviour, the time resolved studies are scarce. This is one of the reasons why chapter 4 focusses on the dynamics of random laser emission. The second is the appliance of network theory as a new form of random laser analysis. The presented measurement technique is combined with numerical simulation and discussed using an optical network approach. The network concept has paved its way into new fields of research from climate research [6] over neuroscience [7] to lasing networks [8]. By interpreting the random lasing as an optical network, a new angle is introduced to the simulation of random lasers. The presented approach can be used to predict the dynamical properties of the random laser emission making it a tool for sample design.

The combination of these two well developed fields, namely network theory and semiconductor laser physics, is a good example of the benefits of interdisciplinary research. This is of course also the aim of the International Research and Training Group 1740 providing the framework to develop such a connection.

The random laser is relying on relatively small feedback and is a manifestation of the weak light matter coupling regime. A much stronger feedback is realized in miniaturized cavities, which increase the light matter coupling with high reflective mirrors. When the coupling surpasses the damping of the resonances, the so called strong coupling regime is reached.

Since the beginning of the 90s, strong coupling in microcavities has developed, strongly fuelled by the impressive effects, like room temperature Bose-Einstein-condensation [9] and lasing without inversion [10]. A big step was achieved more recently with the creation of an electrically pumped strong coupling device. In 2013 Schneider et al. [11] presented an electrically excited polariton laser based on inorganic InGaAs quantum wells. Two years later an electrically pumped organic light emitting diode in the strong coupling regime followed [12]. Further effort is needed to produce polariton based optoelectronics with the necessary reliability and stability.

This leads to high expectations for hybrid polaritons, combining the efficient relaxation of inorganic semiconductors with the high quantum yield of π-conjugated organic molecules.

The idea of combining inorganic and organic semiconductors in a strong coupling cavity is not new. It was first developed theoretically in the work of Agranovich et al. in 1997 [13], hereby proposing the efficient relaxation in such systems. In 1996 the first realization of strong coupling in a hybrid microcavity was presented simultaneously by Holmes et al. [14] and Wenus et al. [15]. Their hybrid devices reached the strong coupling regime, proven by reflectivity measurements. Further improvement of fabrication is needed to overcome the limitations in emission.

New material systems like the specially synthesised organic molecule and ZnO, presented in this thesis, can help to tailor the polariton relaxation. This molecule was available and got my interest because of my colleagues working in the CRC 951 on the topic of hybrid inorganic organic systems.

Both areas, the random lasing and the strong coupling microcavities, have high potential to become a new sort of light emitters for research and commercial applications.

The investigation of the organic molecule in question, a ladder-type oligo(*p*-phenylene), is discussed in detail in chapter 5. The combination of this molecule with high quality, MBE grown ZnO structures is the focus of chapter 6.

2 Background

2.1 Material properties

The following sections will introduce the materials used for the different samples investigated in this work with a main focus on the optical properties of the structures.

2.1.1 Zinc oxide and its compounds

Zinc oxide (ZnO) is one of the two main components of this thesis serving as the inorganic semiconductor in all presented investigations. ZnO is a wide band gap, II-VI, semiconductor with high potential for technical applications. It is highly available, non-poisonous and emits light in the near ultra violet range. It can be processed with a lot of different deposition techniques and can be produced with high crystal and optical quality. This makes it feasible for optoelectronics and light emitters in the energy range now occupied by gallium nitride (GaN) structures, since the main emission is in the near ultra violet (UV) range at $\approx$ 380 nm.

By adding metals like gallium (Ga) and aluminium (Al) ZnO can be used as a cheap alternative to transparent conducting electrodes made from indium tin oxide (ITO) and opens a new field of investigation of plasmonics for optical sensors in the infra-red range [16]. While p-doping of ZnO has been achieved, its stability and carrier mobility is still an obstacle to overcome [17].

At room temperature the bulk material has a direct band gap of about 3.37 eV, which can be tuned to higher energies by adding magnesium (Mg) or to the blue and green range by adding cadmium (Cd). Fig. 2.2 shows the band gap of the different materials in particular ZnO, MgO and CdO, which can be alloyed with ZnO. ZnCdO based structures are used in the investigation of random lasing described in detail in chapter 4 and ZnMgO structures are used in the hybrid cavity experiments discussed in chapter 6. ZnO depositions can be done with a great variety of techniques like sputtering, sol-gel processing, pulsed laser deposition, electron beam evaporation, molecular beam epitaxy (MBE) and metal organic chemical vapour deposition (MOCVD) to give only a few examples [18]. Further description will focus on the techniques for epitaxial growth and especially on MBE since the investigated samples are mainly produced by the latter technique. For the description of the MBE setup used in this research see section 3.1.1.

The crystal structure of undoped ZnO is most stable as a hexagonal wurtzite structure. In the hexagonal lattice an O atom is surrounded by four Zn atoms in tetrahedral geometry. Fig. 2.1 represents this structure. The point group is 6_{mm} or C_{6v} depending on the notation with the space group $P6_3mc$. At room temperature the primitive translation vectors are a = b $\approx$ 3.252 $\mathring{A}$ and c $\approx$ 5.213 $\mathring{A}$ [19].

A common growth direction is perpendicular to the (0001) plane, which means growing on a polar surface, that can be either Zn or O terminated. By convention the oxygen terminated surface is marked as $(000\bar{1})$ and the zinc terminated (0001). For different polarities the growth and bulk properties deviate from each other in growth mode and the incorporation of impurities. ZnO is also commonly grown on sapphire substrates due to their excellent crystal and surface polishing quality and low cost commercial availability. All ZnO-based samples in this work were grown on sapphire substrates by radical source molecular beam epitaxy. These substrates were purchased from "Crystec GmbH" and have a thickness of 0.5 mm. They are cut into square pieces of 8 mm, 10 mm or 20 mm edge length depending on their use. Buffer layers are grown on most samples to improve the ZnO quality, which is necessary because of the big lattice mismatch to the substrate.

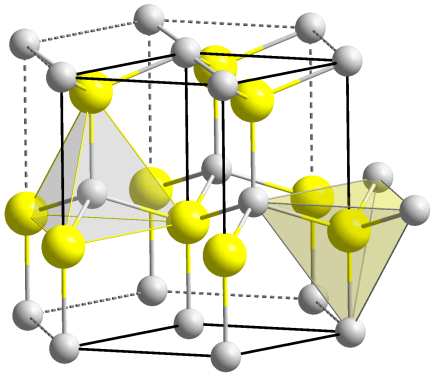

Figure 2.1: Schema of the hexagonal structure of ZnO (picture from ref. [20]). The grey spheres represent the zinc atoms, the yellow the oxygen atoms. Other representations and detailed information for the zinc oxide crystal structure can be found in [21].

Ternary alloys

Alloying the ZnO with Mg increases the band gap. At about 40 % molar concentration the crystal structure is changing to a mixed phase of hexagonal and cubic form. Above 65 % the crystal structure is stable in the cubic form of MgO. Fig. 2.3 presents the transmission spectra of ZnMgO layers of different molar fractions of Mg content, produced in our group. Layers of higher Mg contents with mixed crystal structure or the cubic phase are presented in [22]. The interference fringes in the transparent region show that the layers are a few hundred nm thick. These fringes are produced by a Fabry-Pérot cavity with low reflectivity created by the interface of the epilayer to air and the sapphire substrate. The transmission edge of the absorption varies depending on the composition from pure ZnO (about 380 nm) to $Zn_{60}Mg_{40}O$ (about 300 nm). The energy gap in the pure cubic phase increases from 5.5 eV (225 nm) to about 7.2 eV (200 nm) for the pure MgO. An example for the transmission of such mixed phases and rocksalt structures can be found in ref. [22], but only wurtzite structures are discussed further.

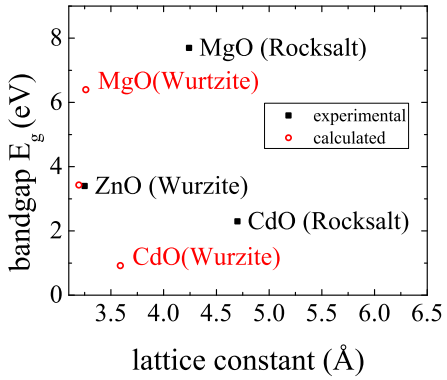

Figure 2.2: Lattice constant a and band gap energy E_g for wurtzite ZnO [19] and rocksalt MgO [19] and CdO [23]. Calculated values for wurtzite structures presented (circles) are taken from ref. [24].

To lower the band gap energy of ZnO, Cd can be incorporated to produce a ZnCdO alloy. Since CdO has a rocksalt structure as well, the Cd concentration in the alloy is similarly limited. The band gap tuning limits reached in our group using low temperature epitaxy is about 32% resulting in an energetic band gap of ≈ 2.2 eV at room temperature [25]. Both ternary alloys can be used to grow quantum well (QW) structures. For ZnCdO QW structures the well is created by a thin layer of the ZnCdO material and pure ZnO acts as the barrier material. Samples incorporating multiple of these QWs will be discussed in detail in chapter 4.

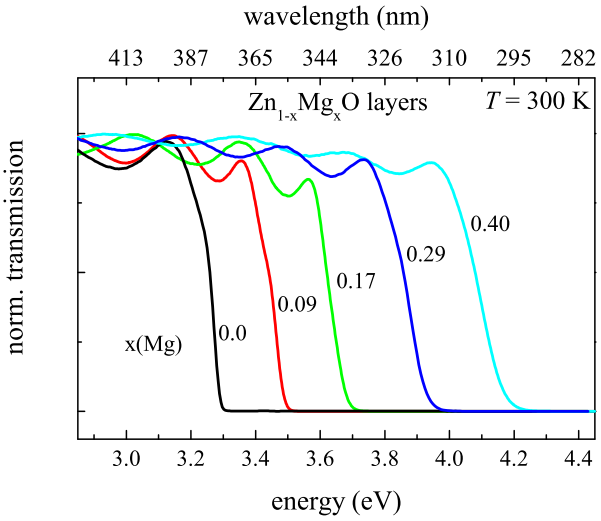

Figure 2.3: Shift of the absorption edge of ZnMgO layers depending on their Mg content produced in our group (presented with permission of S. Sadofev). Higher concentration can not be used practically since the change for wurtzite to rocksalt lattice will start in a mixed phase. At about 70% Mg a stable rocksalt structure with much higher band gap is formed.

An equivalent structure in a higher energy range can be created by using ZnMgO as the barrier and ZnO as the well. In all these structures the energy gap of the well is

smaller than in the barrier and a quantum confinement is realized by reducing the QWs thickness below the exciton Bohr radius. This creates a 2D system changing the density of states in the structure (see 2.2.3). Furthermore, efficient relaxation is possible from the barrier to the QW, which increases the emission of the well region. ZnMgO based QWs emit in UV range and ZnCdO can reach the blue and green region of the visible spectrum [26].

2.1.2 Ladder-type oligo(p-phenylene)s

The *para*-phenylenes (*p*-phenylenes) are well known organic molecules, which are used in dye lasers, because of their efficient light emission under optical excitation. They consist of a number of benzene rings in a row connected by a single bond. They have a conjugated π-electron system, which makes them highly efficient light emitters over a wide range of wavelengths. The following curves show the typical absorption and emission behaviour of *p*-quaterphenyl. They are reaching a high quantum yield of nearly 1 in solution. All *para*-phenylenes have broad emission spectra, which change their transition maxima depending on the length of the molecule. Terphenyl, having three aromatic rings, shifts to the UV, while sexiphenyl, incorporating six rings, shifts further to the visible. This energy dependence on the chemical structure makes *p*-phenylenes a highly versatile group for the combination with other materials.

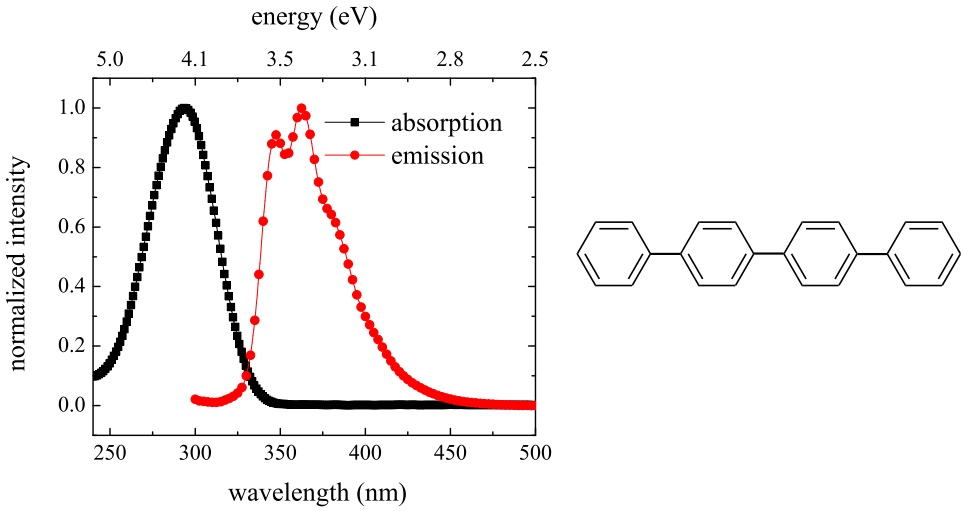

Figure 2.4: Normalized absorption and emission of *para*-quaterphenyl in a solution of chloroform. Presented with permission of F. Bianchi.

Since the absorption and emission of such molecules are too broad, they are not well suited for strong coupling or energy transfer to other resonances. Sharper resonances are beneficial in such experiments, so the molecules were chemically altered by giving them a more rigid backbone structure. These are the so called ladder-type oligo(*p*-phenylene)s. Synthesis of such ladder-type molecules were first presented by U. Scherf and K. Müllen

[27, 28]. A chemically altered version of *p*-quaterphenyl with a more rigid backbone structure is the active molecule in the presented microcavity structures. In this ladder-type form, the spectra for absorption and emission still shift depending on the number of aromatic rings [29]. Since we are interested in molecules with sharp resonances close to the resonance of ZnO, we worked with the Group of Prof. S. Hecht of the chemistry department of the Humboldt-Universität zu Berlin. Dr. Björn Kobin created a ladder-type quaterphenyl (L4P) with its main transition close to the ZnO transitions [29]. Fig 2.5 shows room temperature transmission spectra of ladder-type quaterphenyl and its spiro derivative (L4P-SP2) and a 14 times ZnO/ZnMgO MQW. One of the attached spiro groups is marked in Fig. 2.5 b with a frame.

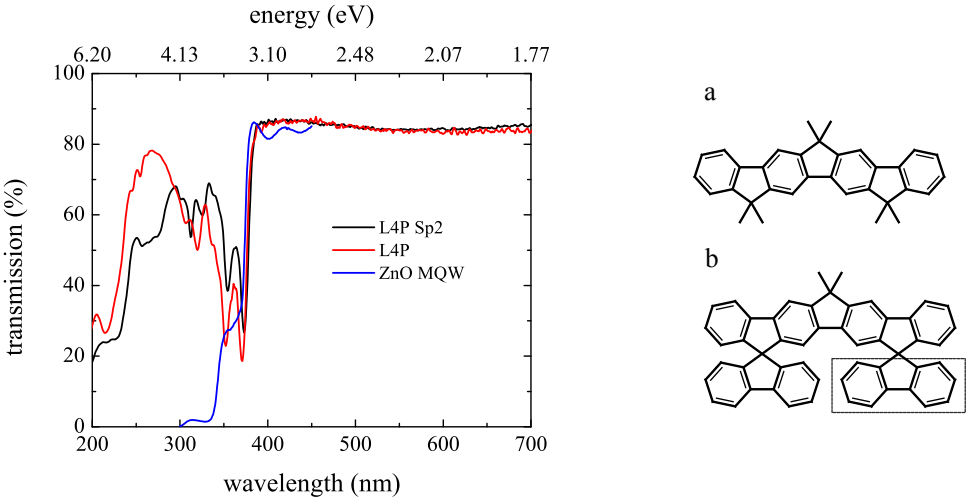

Figure 2.5: Transmission spectra of a 27 wt% L4P (red) in a polymer (Zenoex 480) and 20 wt% L4P-SP2 (black) in the same polymer layer about 110 ± 10 nm thick spin coated on sapphire and a 14 times ZnO/ZnMgO MQW. a: Molecular structure of L4P, b: Molecular structure of L4P-SP2.

The investigated samples were spin coated layers of L4P(L4P-SP2) in polymer (Zeonex 480) dissolved with the active molecule in toluene. The layers have nearly identical thicknesses clearly identifiable by the broad Fabry-Pérot oscillations. The main absorption peak is in resonance to the ZnO absorption, which starts at 380 nm. The second step in the transmission of the ZnO sample is caused by the barrier layer made of ZnMgO. Creating the ladder-type backbone structure clearly sharpened the molecular transition and placed the main transition in resonance to ZnO. Depending on the two spiro groups, the main absorption peak is shifted slightly to higher wavelength (≈ 2 nm or 18 meV). For more information on the chemical synthesis of this molecule see ref. [29].

Since *p*-quaterphenyl is used as a laser dye in commercial dye lasers, a characterization of the possible optical gain was necessary to see if the chemical alteration changes its capability as an active laser medium. Further information on the used techniques and the results will be presented in detail in section 5.4. Colleagues of mine also investigated

its stability under long time UV irradiation [30] and Förster-type energy transfer of ZnO and L4P [31], as well as the growth of high quality thin layers in organic molecular beam deposition of the similar sexiphenyl [32].

The optical characteristics of this molecule in combination with the versatile techniques for sample fabrication make it a promising active material in hybrid microcavities based on ZnO. Their investigation will follow in chapter 6.

2.2 Light absorption and emission of semiconductors

In inorganic semiconductors the absorption is described as the transition of an electron from the valence band (VB) to the conduction band (CB), hereby crossing an energy gap (E_g). In organic semiconductors these states are called highest occupied molecular orbital (HOMO) and lowest unoccupied molecular orbital (LUMO). This process can be reversible, this means an electron can relax from an excited state (CB, LUMO) to the ground state by emission of a photon. This emission, also called luminescence, can be investigated with spectral and temporal resolution to characterize samples.

2.2.1 Band structure of ZnO

The band structure of bulk semiconductors describes the energy of the electrons in a semiconductor, depending on the position (the k-vector) inside the Brillouin zone. The band structure of inorganic semiconductors can be calculated for example by using the empirical pseudo-potential method [33, 34]. They reveal the maximum/minimum energy of VB and CB at the Γ-point of the Brillouin zone making ZnO a direct semiconductor with $E_g = 3.37$ eV. For more information on the ZnO or ZnMgO band structure see [34]. Near the Γ-point at $k = 0$ the energy levels can be schematically drawn like in Fig. 2.6, showing a splitting into A, B and C band known for wurtzite structures [16].

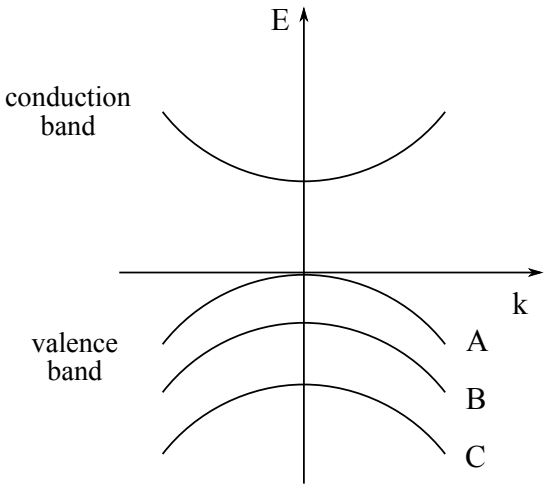

Figure 2.6: Schematic drawing of the band structure of a wurtzite type semiconductor like ZnO near the Γ-point of the Brillouin zone. The transitions to the A and B band are mostly perpendicular polarized, the transition to the C band mostly parallel to the c-axis.

When a semiconductor is excited an electron is transferred from the valence band (VB)

to the conduction band (CB) leaving a positively charged hole in the VB. The positive hole and the negative electron can interact to form a new hydrogen like quasi-particle called exciton.

2.2.2 Excitons

An exciton is a quasi-particle describing the excitation in semiconductors that creates a bound electron-hole pair. Excitons exist in inorganic and organic semiconductors, but are treated by different mathematical models.

Excitons in inorganic and organic semiconductors

In inorganic semiconductors excitons are mostly of the Wannier-Mott type. One way to calculate their energy levels is to assume a Coulomb potential with an effective mass approximation. The exciton is then a hydrogen like system. In general, inorganic semiconductors have binding energies in the range of 10 meV to 100 meV and a Bohr-radius bigger than the elementary cell of the semiconductor. The excitons in organic molecules are stronger localized and have higher binding energies by about one order of magnitude. They are called Frenkel excitons. If we use the hydrogen model, an approximation for the exciton energy is given by

$$E_n(k) = E_\mathrm{g} - \frac{\mathrm{Ry}^*}{n^2} + \frac{\hbar^2 k^2}{2(m_e + m_h)} \tag{2.1}$$

With E_g being the band gap energy, $\mathrm{Ry}^* = 13.6$ eV $\mu/(m_0 \cdot \epsilon^2)$ the exciton Rydberg energy and n the principle quantum number. $\mu = \frac{m_e m_h}{m_e + m_h}$ is the reduced exciton mass, m_0 the electron mass, m_e (m_h) the effective electron (hole) mass, $\hbar$ the reduced Planck constant, ϵ the dielectric constant and k the wave vector of the exciton [35].

The binding energy [36] and exciton Bohr radius a_B of an exciton can be calculated with

$$E_{bin}^n = \frac{\mathrm{Ry}^*}{n^2} = \frac{\mu e^4}{n^2 2\hbar^2 (4\pi\epsilon)^2} \tag{2.2}$$

$$a_B^{\mathrm{ex}} = \frac{\hbar}{\sqrt{2\mu \cdot \mathrm{Ry}^*}} = \frac{\hbar^2 4\pi\epsilon}{\mu e^2} \tag{2.3}$$

The exciton binding energy is an important material parameter, because if its value surpasses the thermal energy at room temperature ≈ 25 meV a thermal dissociation is unlikely.

The table 2.1 shows typical values for exciton binding energies calculated by this technique as well as useful other material constants.

Table 2.1: Values of the band gap (E_{g}), exciton binding energy ($E_{\mathrm{bin(H)}}$), the exciton Bohr radius (${a_B}^H$) and experimental values for the exciton binding energy (E_{bin}(exp.))[37]. Three exemplary organic molecules and their optical absorption energy E_{opt} and their binding energy E_{bin}.

material	structure	E_{g} (eV)	$E_{\mathrm{bin(H)}}$ (meV)	${a_B}^{\mathrm{ex}}$ (nm)	E_{bin}(exp.) (meV)
ZnO	wurtzite	3.44 (4.2 K)	37.5	2.4	60
GaN	wurtzite	3.51	22.0	3.3	23.4
AlN	wurtzite	6.25	36.3	2.3	57
organics		E_{opt} (eV)			E_{bin}(exp.) (eV)
Alq_3		3.2			1.4 [38]
PDCDA		2.6			0.6 [38]
Anthracene		4.15			1.0 [39]

These values represent the exciton binding energies smaller than 100 meV corresponding to the Wannier-Mott type. Their Bohr radius is of the order of a few nm. So they are bigger than one unit cell and can move through the crystal structure. This is also the reason why the hydrogen model can be applied.

The different binding energies in the experiment and the model shows that the model does not work well for ZnO. This can be improved by adding corrections to the model. They are not presented here, but the interested reader is asked to refer to literature like ref. [35].

The Frenkel excitons typically found in organic molecular crystals and materials differ strongly. Their binding energies are in the order of 1 eV, hereby reducing the Bohr radius to $\approx$ 1 nm or lower. These Frenkel excitons are mostly localized to one molecule.

The exciton properties presented in table 2.1 are for bulk materials. In many cases semiconductor materials can be layered during growth changing the potential depending on the material in use. If a semiconductor of lower band gap is grown between two layers of higher band gap, a potential well (quantum well) is created in growth direction. If the well width is in the order of the exciton Bohr radius, the exciton is confined in one direction changing its optical properties. The dimensions perpendicular to the growth direction are not confined.

2.2.3 Inorganic quantum wells

Semiconductor structures grown in layers with a well and a barrier are commonly used to introduce a confinement in the sample. This makes them more efficient light emitters at a certain wavelength. In most configurations the well thickness is set around the exciton Bohr radius of the material.

For our samples typical values are around 3 nm and a barrier thickness about twice as much creating a multi quantum well structure. The schema in Fig 2.7 gives a possible sample design for a QW structure.

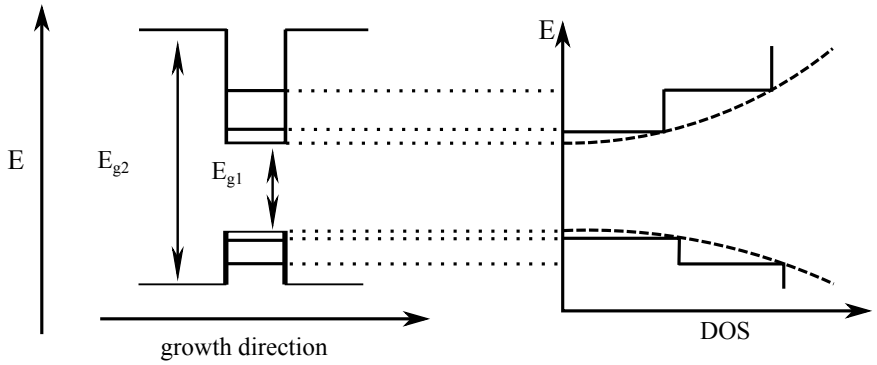

Figure 2.7: Left: Representation of a quantum well structure. Right: The corresponding density of states (DOS). The dashed lines represent the DOS in a bulk material (adapted from [40]).

The confinement modifies the density of states (DOS) which depends on the square root of energy in the bulk material. The DOS is directly connected to the kinetic energy of electrons and holes in the semiconductor. They follow a distribution of states which is altered compared to the bulk structure. This confinement shifts the emission energy to higher energies for smaller thicknesses [41]. An exemplary low temperature (4 K) photoluminescence is presented in Fig. 2.8.

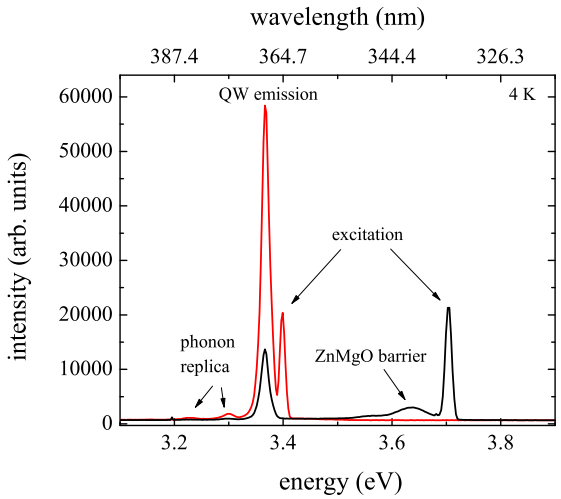

Figure 2.8: Photoluminescence of a 14 times multi quantum well excited by a xenon lamp with a double monochromator. The measurement was performed at helium temperature (4 K) with the excitation above the barrier (3.82 eV, black) and below (3.40 eV, red).

The 14 time MQW has a well thickness of 3.8 nm and a barrier thickness of 8 nm. They are grown on a buffer layer of $Zn_{0.65}Mg_{0.35}O$, which is about 600 nm thick. Suggested by the barrier luminescence, its Mg constant is around 18%.

2.2.4 Molecular transitions

Light emitters and lasers based on organic molecules have a long tradition of using materials based on aromatic rings with a delocalized π-electron system because of their broad emission range of up to 60 nm for a single type of molecule. Different types of molecules were employed to either produce sharper substructures in emission or broadened emission due to their vibrational states. These dyes typically used in laser sources have no strong vibrational features. The broad emission is necessary to reach tunability over a wide range, with only minor changes in intensity. Dye lasers were also widely used for short pulse generation by passive mode locking in the femtosecond range. They are now mostly replaced by tunable titan-sapphire laser systems, even in the continuous wave systems, which makes reaching the UV range only possible with high technical effort, like electronically stabilized frequency doubling. The emission of organic molecules is quite strongly depending on their surrounding. It varies for different solvents, thin layers produced by evaporation, crystals and polymer matrices.

Depending on the chemical structure of the molecule the vibrational states can be resolved in spectroscopic investigations. For the ladder-type oligo(*p*-phenylene)s used in this work their rigid backbone structure makes the different vibrational states visible even in solutions [29] as well as in evaporated layers [31]. The schema in Fig. 2.9 shows the Franck-Condon principle describing the intensity distribution of the vibronic states, typical for organic molecules.

The figure 2.9 presents a ground state (black) with a harmonic potential. The excited state has a similar (not identical) potential slightly shifted in the nuclei coordinate in equilibrium. Inside the potential there are energy levels corresponding to the vibrational transitions of the molecules. Rotational levels are not taken into account. If the molecule is excited by an optical pulse, an electron from the lowest vibrational level in the ground state (HOMO) gets to an excited state depending on the absorbed energy. Since this electronic change is fast, the heavier nuclei will stay constant in their distance, hence the transition is drawn as a vertical line. Then the electron relaxes non-radiatively to the lowest level of the excited state (LUMO). The electron can now relax to one of the vibrational levels of the ground state without a change in the nuclei coordinate.

The transition probability depends on the overlap of the wavefunctions of the ground and the excited state. Fig. 2.9 only shows one excited state. There is also a triplet state absorbing light, which is meta stable with life times up to seconds. Especially for laser applications the triplet states have to be considered, at least for some molecules, because their long life time making the pumping process less efficient over time. This is the main reason dye lasers have a circulation system with a reservoir to avoid a high occupation of the triplet state in the active material. In the experiments presented in chapter 5 the triplet occupation is of minor influence, but the values of optical amplification will depend on the repetition rate of the excitation source. More information about the triplet state can be found in ref. [42]. Since the absorption and the intersection crossing rate is small only the singlet transitions are discussed further.

Assuming the energy levels can be approximated at least for the lower levels by a harmonic oscillator, we know that the electron probability density depends on the po-

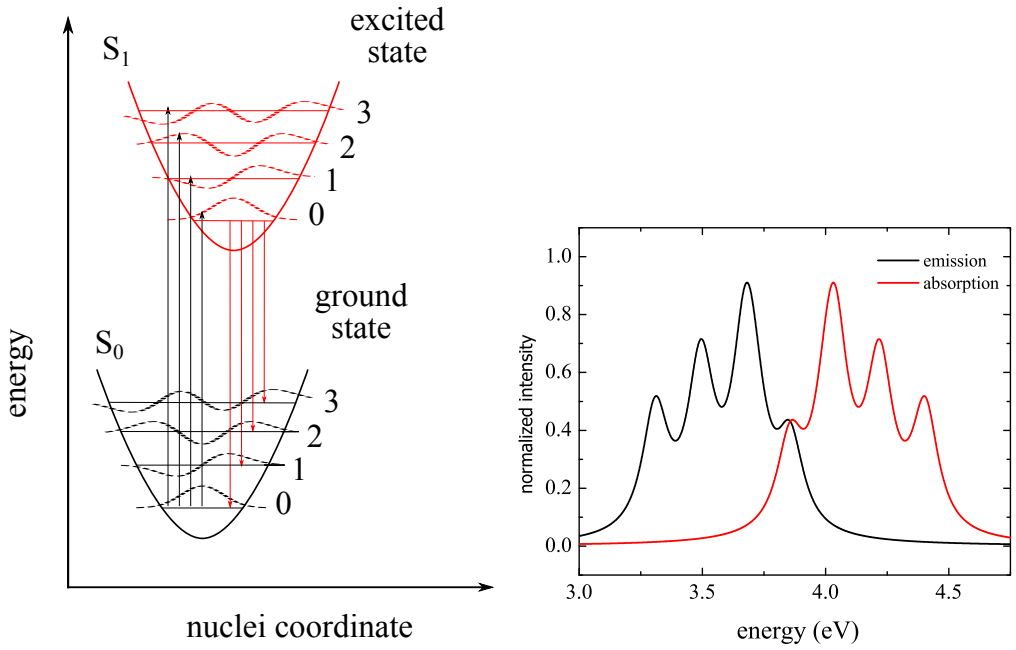

Figure 2.9: Left: Diagram of the Franck-Condon principle of the vibronic transitions in molecules, with the wavefunction drawn for every level to visualize the overlap resulting in the different transition strength. Right: Schematic representation of a molecular absorption and emission spectrum with re-absorption at the (0,0) transition. The drawn harmonic potential is not really applicable for the L4P molecule, but it gives one possible realization of a mirrored absorption and emission spectrum.

sition inside the potential. Transitions hitting a high probability, the square of the wavefunction, are more likely, following a high intensity in the spectrum. For the drawn example the mirrored progression of the vibrational states is visible. This is also true for our real active molecule but the vibrational states show a substructure presented in the transmission Fig. 2.5. In the experiments the (0,0) transition of L4P is lowered due to re-absorption, if the concentration is high enough. In diluted solutions re-absorption is weak and the (0,0) line is the strongest transition [29].

2.3 Lasing principles

Since the first realization of the ruby laser (**L**ight **A**mplification by **S**timulated **E**mission of **R**adiation) in 1960 [2], lasers have influenced everyday life as well as the work in optical laboratories. Especially small sized lasers based on semiconductor structures have found many applications because of the cost efficient fabrication and energetic efficiency. Active materials in lasers can amplify light, so they produce optical gain. This gain material is placed in a resonator to increase the light passes through the active

medium.

2.3.1 Stimulated emission

Stimulated emission is an optical transition making the optical amplification possible.

If a material is excited strongly and the occupation in the excited state is high enough, the stimulated emission rate is bigger than the absorption, which makes the medium an optical amplifier.

For this to be possible, the material has to be excited to such an extend that an occupation inversion is reached. The schema in Fig 2.10 visualizes the energetic level alignment to realize an inversion.

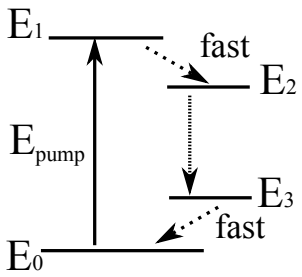

Figure 2.10: 4 level laser system. E_0 is the ground state and electrons are excited from here to E_1. Fast non-radiative relaxation is depicted with dotted lines to the level of E_2, which has higher occupation than E_3 creating the inversion. Keeping the inversion is only possible, if a fast relaxation depopulates E_3 to E_0.

Using this optical amplifier with a single path and without an optical feedback is called superluminescence or amplified spontaneous emission (ASE). In chapter 4 such a system will serve as an excitation source, but in general a laser resonator is needed or at least beneficial for lasing operation. Resonators increase the efficiency, coherence and directionality of the emission.

One of the standard resonators is the Fabry-Pérot cavity, which is characterized by two (partially) reflecting flat mirrors. These types of cavities are mostly used in short laser systems, since they are not very stable but easy to fabricate. They are a common choice for micro resonators and Vertical Cavity Surface Emitting Lasers (VCSEL). They are also used in optical measurements as optical filters (metal interference filters) and as interferometers in high spectral resolution detection systems. Most of the samples presented in this work make use of such cavities.

2.3.2 Fabry-Pérot resonators

Depending on the resonator geometry the cavity allows only certain longitudinal and transversal modes to exist. They are (almost) standing waves and strongly influencing the parameters of the emission. Hereby, one important parameter is the cavity length determining the free spectral range (FSR) of the resonator given by the spectral distance of two longitudinal modes. This distance is given by

$$\Delta\omega = \frac{c_n}{2L_{\text{cav}}} \tag{2.4}$$

With $\Delta\omega$ the difference in frequency, c_n the group velocity of light in the medium and L_{cav} the length of the cavity. If a laser is build with such a resonator and the FSR is wider than the spectrum of the gain distribution, one single mode will be emitted. In Fig. 2.11 we see the transmission of two distributed Bragg reflectors (DBRs) with no active cavity material realizing an interference filter with a cavity mode in the centre of the stopband at ≈ 390 nm.

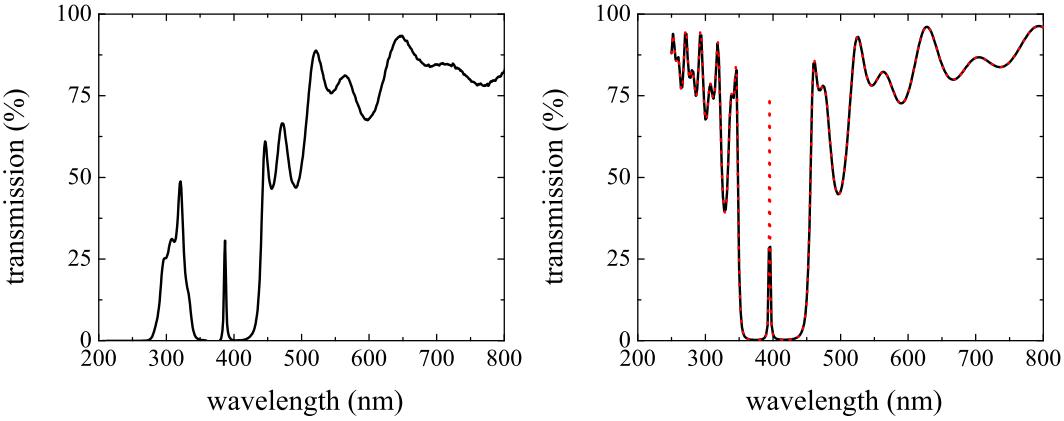

Figure 2.11: Left: Transmission of a dielectric interference filter created by evaporation of $\lambda/4$ optical thickness layers of ZrO_2, SiO_2 with a single longitudinal mode inside of the stopband of the two mirrors. Right: Simulation of the cavity with steps of 2 nm to simulate low resolution measurement (black), and steps of 0.1 nm (red, dotted). All layers were simulated without absorption and only with a real refractive index.

The optical cavity presented in Fig. 2.11 is produced by layers of different refractive indices using electron beam evaporation. If the resonator is illuminated at normal incidence to the surface, only light of a certain energy fulfils the roundtrip condition and is transmitted to the other side. The cavity presented is the shortest possible with a cavity spacer of $\lambda/(2n_{\text{spacer}})$ optical length. This ensures that only one cavity mode forms in the stopbands of the DBRs. For thick spacers the FSR reduces and other modes are formed in the resonator. The low transmission at 300 nm and below is due to the absorption of the substrate which is a standard microscopy slide, made from soda-lime glass. The transmission maximum of the resonator mode is lowered because of the measurement resolution of 1 nm. This effect is reproduced in our numerical simulations, Fig. 2.11. Other effects such as surface roughness can affect the transmission as well. The transfer matrix method (TMM) simulation has clear similarities to the experimentally measured spectrum, but for some oscillations the difference is quite strong. This is due to changes in the optical thicknesses, which arise to some extent from non-ideal thickness control during the evaporation process and differences in material stoichiometry depending on substrate temperature, background oxygen and pressure. Since the sample temperature is chosen low and an oxygen poor atmosphere is used, a non-constant percentage of

monoxides of the dielectrics is introduced in the DBR layers.

The resonance condition is given by

$$r_1 r_2 e^{i2n_{complex}kL} = 1. \tag{2.5}$$

Hereby, r_i are the reflection field amplitudes of the mirrors and a complex phase factor represents the changes due to phase jumps and refractive index inside the cavity. $n_{complex} = n + i\kappa$ is the complex refractive index, which can either imply absorption or gain depending on its imaginary part. k is the k-vector of the light and connected to the wavelength by $|\mathrm{k}| = 2\ \pi/\lambda$ and L is the cavity length. $\kappa = \frac{\alpha\lambda}{4\pi}$ with α being the absorption/gain, depending on the algebraic sign. This makes the separation of 2.5 into a real and imaginary equation possible.

$$\text{real part:} \quad r_1 r_2 e^{-2\kappa kL} = r_1 r_2 e^{g_{th}L} = 1 \tag{2.6}$$

$$\text{imaginary part:} \quad 2kLn = 2\pi \Rightarrow 2Ln = \lambda m \tag{2.7}$$

From equation (2.7) we see that a cavity should have a length of a multiple of $\lambda/(2n)$. Only for cavities smaller than $\approx 10\ \mu$m (at 400 nm) this phase has to be considered in cavity design, since for longer cavities the mode spacing falls to values so small, that there is no need and possibility to control the spectral position.

From the real part equation (2.6) we can calculate the threshold gain $\mathrm{g}_{th} = 1/\mathrm{L}\ \ln(1/(r_1 r_2))$ at least if other forms of losses except the mirror reflectivity can be neglected.

From this follows that there are three different parts of this equation, which can be influenced by the sample design. The reflectivity of the mirrors can be tuned, the length (thickness) of the active material can be increased and the optical amplification can be tuned by the pump energy. All these parameters are more or less limited depending on the material system used.

To excite such a system over its lasing threshold, the losses have to be compensated by the gain. In the present case losses are scattering processes due to the roughness of layers, absorption in the mirrors or cavity material and the out-coupled light. For the ideal system discussed above, we assumed no scattering and roughness effects and that the dimension of the gain material is bigger than the optical mode.

Only a partial overlap of optical mode and gain material is used in the gain measurement in a leaky waveguide configuration [43, 44, 45]. Such an experiment can be performed with a stripe excitation on a sample with a thin layer, whose refractive index is at least slightly higher than that of the substrate. By that a guided mode in the layer is formed, which is enhanced due to the gain in the excited stripe. Since the refractive index contrast between substrate and layer is small, a large part of the optical mode extends into the substrate, where no gain is possible. That means that only partial amplification of the mode can be measured, the so called modal gain g_{modal}.

Fig. 2.12 on the left depicts a simple Fabry-Pérot cavity with a gain medium inside and on the right a leaky waveguide system used for gain measurements in chapter 5. Such a configuration with improved reflectivity at the interfaces and light emission perpendicular to the growth direction is used in many semiconductors lasers to have a greater length of the gain material. This type of laser is called edge emitter and the main choice for high power semiconductor lasers.

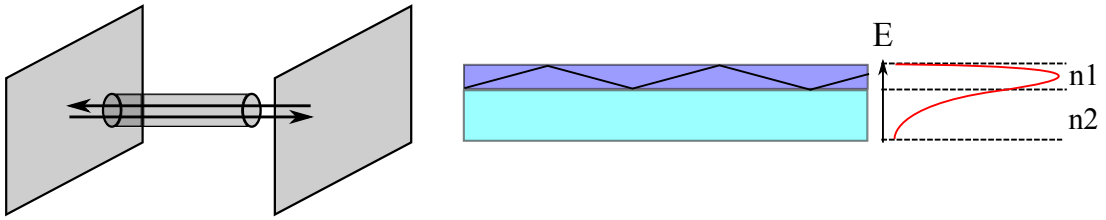

Figure 2.12: Left: Fabry-Pérot cavity with a gain medium inside. Right: Leaky waveguide for measuring optical gain of a material with a schematic to visualize the modal gain by the guided wave and the evanescent field in the substrate material ($n_1 > n_2$).

The electric field in the material can be calculated, but in many cases it is sufficient to get a rough estimate since most of the gain measurements are not performed at the gain maximum, because a thermal destruction of the sample is quite likely. Such experiments are mostly a proof of concept that inversion is possible and gain can be achieved at a certain spectral position. It can be interpreted as a minimum value, while higher values are possible (even likely). A cavity designed for such a gain will work with high probability. The experimental technique for such a modal gain measurement is described in detail in chapter 5.

2.3.3 Cavity tuning

The experiments on strong coupling rely on the tuning of one resonance to another. The tuned resonance can either be the material resonance or the cavity resonance. While tuning of the material resonance is very limited it can be done in semiconductors using their temperature shift. In most cases the cavity resonance has a much higher tuning range. It is possible to use a cavity with a wedge in the middle, which can be filled with the active material [15]. Another common technique uses the angular dispersion of the cavity. If the angle of incidence of a Fabry-Pérot cavity is changed, its optical resonance is shifted to the blue.

Such a dispersion can be modelled by one over cosine dependency. We separate the incident k-vector in a component perpendicular to the surface k_z and in-plane $k_{inplane}$ with the cavity.

In general

$$k^2 = \sqrt{k_z^2 + k_{inplane}^2} \tag{2.8}$$

and

$$k_z = k \cdot \cos(\alpha) \quad \text{and} \quad k_{inplane} = k \cdot \sin(\alpha) \tag{2.9}$$

The energy of the cavity photon is then given by

$$E_c(k) = c\hbar k \Rightarrow E(\alpha) = c\hbar \frac{k_z}{\cos(\alpha)} = \frac{E(k_z)}{\cos(\alpha)} \text{ with } E(k_z) = E(\alpha = 0) \tag{2.10}$$

The k_z component is a conserved quantity for a certain cavity and proportional to the energy. This energy is also called the cut off energy of a cavity. The simple formula above is only true for a constant refractive index, but in most cases the angle of incidence is measured in air, while the cavity has a quite complex refractive index profile. This will change the angle inside the cavity. In many cases this can be approximated by an effective refractive index of the complete structure, which changes the angle inside following the Snell's refraction law.

$$n_{\text{out}}^2 \sin^2(\alpha_{\text{out}}) = n_{\text{in}}^2 \sin^2(\alpha_{\text{in}}) \tag{2.11}$$

$$\frac{n_{\text{out}}^2 \sin^2(\alpha_{\text{out}})}{n_{\text{in}}^2} = 1 - \cos^2(\alpha_{\text{in}}) \tag{2.12}$$

With $n_{\text{out}} = 1$ and $n_{\text{in}} = n_{\text{eff}}$ follows

$$\cos(\alpha_{\text{in}}) = \sqrt{1 - \frac{\sin^2(\alpha_{\text{out}})}{n_{\text{eff}}^2}} \tag{2.13}$$

So we can model the angular dependent dispersion of a microcavity with:

$$E(\alpha) = \frac{E(0)}{\sqrt{1 - \frac{\sin^2(\alpha_{\text{out}})}{n_{\text{eff}}^2}}} \tag{2.14}$$

The n_{eff} will differ slightly, depending on the polarisation.

Fig 2.13 shows the angular dispersion of an empty microcavity. The dots represent the minima of the reflection spectrum in steps of 1°. The fit (red, solid line) is given by Eq. (2.14) with the fit parameters $E_0 = 3.06$ eV and $n_{\text{eff}} = 1.86$.

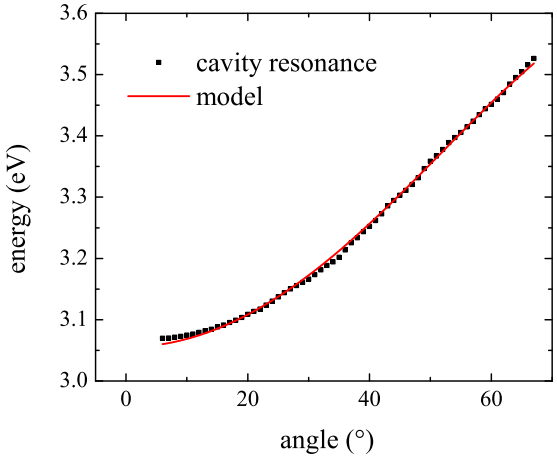

Figure 2.13: Energy of a Fabry-Pérot cavity depending on the angle of incidence. Position of the reflection minima (symbols) and fit to the data with the model 2.14 with $E_0 = 3.06$ eV and $n_{\text{eff}} = 1.86$ (red line).

2.3.4 Feedback by scattering centres

This work presents a feedback mechanism based on scattering centres in a random laser. Such a system has no cavity made of mirrors, but in quite similar way the scatterer have kind of an effective reflectivity. Looking at the simplest case of two scatterers with the gain medium in between, the threshold condition can be written as

$$\frac{\sigma_b}{L_c^{m-1}} e^{gL_c} = 1 \tag{2.15}$$

with m being the dimensionality of the system, L_c the cavity length and $\frac{\sigma_b}{L_c^{m-1}}$ the probability of back scattering in the direction of another particle [46] with σ_b the back scattering cross section for Mie scattering. g is the threshold gain necessary to reach laser operation. This looks quite similar to the threshold condition for a Fabry-Pérot cavity (Eq. (2.6)) with the difference of changing the reflection coefficient for the scattering cross section and the geometrical dependence of a spherical wave (m=3) or a cylindrical wave (m=2).

2.3.5 Dielectric mirrors based on transparent oxides

Dielectric mirrors also known as DBRs are a key element for microcavity structures. Contrary to metal layers as cavity mirrors, the DBRs can reach higher reflectivity values up to almost 100 %, which made them the mirror of choice in most laser systems. These DBRs are created by alternating layers of high and low refractive index with a quarter optical thickness ($d = \lambda/(4n)$) of the design wavelength. They are commercially available for almost every energy range. Depending on the refractive index difference

Material	compound	refractive index (at 550 nm)	transparency
Titanium oxides	TiO_2	2.65[48]	400 - 11000 nm
Tantalum oxides	Ta_2O_5	2.16 [49]	300 - 10000 nm
Zirconium oxides	ZrO_2	2.17 [50]	230 - 7000 nm
Hafnium oxides	HfO_2	2.12 [51]	230 - 8000 nm
Scandium oxides	ScO_3	2.00 [52]	230 - 12000 nm
Yttrium oxides	Y_2O_3	1.94 [53]	250 - 12000 nm
Magnesium oxides	MgO	1.74 [54]	200 - 8000 nm
Aluminium oxides	Al_2O_3	1.77 [55]	190 - 7000 nm
Silicon oxides	SiO_2	1.46 [56]	200 - 3000 nm

Table 2.2: Refractive index values of transparent oxides taken from "refractive index info" website, giving the original publication [57]. The values are typical for crystals, not amorphous layers. The area of transparency was taken from [58].

at the design wavelength, the stopband, is created. The stopband width is bigger for materials with high refractive index contrast and a lower number of layer pairs is needed for high reflectivities. The stopband width can be approximated to be [47]

$$\Delta\lambda = \frac{2\lambda_{\text{centre}}\Delta n}{\pi n_{\text{eff}}} \tag{2.16}$$

with $\Delta\lambda$ being the stopband width, λ_{centre} the stopband centre and n_{eff} the effective refractive index of the DBR material. This effective refractive index is approximated by the arithmetic mean for low refractive index contrast. For high contrast a geometric mean can be used [47]. Since the DBR reaches its high reflectivity with high numbers of layer pairs, it has a penetration depth. This will change the length of a microcavity in comparison to a metal mirror. However a precise fabrication control is of prime importance, since the highly reflecting stopband is limited to a certain wavelength range.

Table 2.2 gives typical values of refractive indices for oxides used in dielectric mirrors, at least for their crystal structures. Most of them will not reach values in amorphous layers and vary depending on the evaporation conditions.

Since our evaporation parameters were adjusted for low temperatures, necessary to protect our active materials, the refractive indices will differ strongly from the crystalline material. Typically the evaporation is done with high substrate temperature and an oxygen background to increase the quality of the dielectric layers. This suppresses material with lower oxidation, introducing stoichiometric fluctuations, and produces homogeneous layers. In Fig. 2.14 the transmission of a DBR grown by electron beam evaporation (dots) and a TMM simulation of the structure (red line) is presented. It is fabricated from 6.5 alternating ZrO_x/SiO_x layer pairs beginning and ending on ZrO_x. Their thickness is quarter of the design wavelength divided by its refractive index ($\lambda/(4n)$). The sample was grown on an a-plane sapphire substrate.

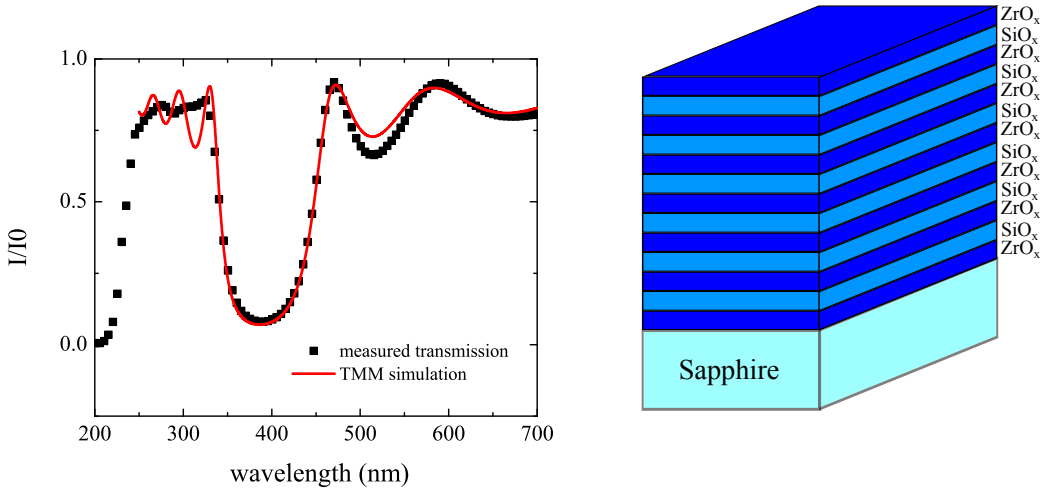

Figure 2.14: Measured transmittance of a dielectric mirror grown on sapphire and the TMM simulation for the same structure using the refractive index modelled by using experimentally identified values for the refractive index.

Since organic molecules degrade at high temperature in oxygen atmosphere, a low temperature evaporation with no oxygen is used. Controlling the optical parameters is more challenging but can be realized, at least for the purposes presented later. This makes a characterization of evaporated material produced under these conditions necessary, to find the actual refractive index for further DBR and cavity designs.

Since a DBR mirror only reaches its high reflectivity if the optical thickness d/n is constant for every layer, it is crucial to hold the thickness and refractive index constant during evaporation to achieve high quality mirrors. For design purposes the reflectivity can be approximated by the Eq. (2.17) assuming quarter wavelength layer thicknesses [59]. For high numbers of layer pairs m this formula breaks down but it is a quite efficient tool in cavity design without using the TMM.

$$R = \left(\frac{(n_0 n_2^{2m} - n_3 n_1^{2m})}{(n_0 n_2^{2m} + n_3 n_1^{2m})} \right)^2 \tag{2.17}$$

With n_1, n_2 the refractive index of the DBR materials and n_0, n_3 the refractive index of air and substrate. Combining two of these DBRs separated by a spacer layer will create a microcavity. Depending on the spacer thickness the spectral distance between two neighbouring longitudinal modes can be tuned. In most cases the spacer is chosen in the order of the wavelength shifting the other modes so far, that they are outside of the stopband.

If two DBRs are evaporated on top of each other, separated by a cavity layer of $\lambda/(2n)$ optical thickness, the smallest possible Fabry-Pérot cavity, a microcavity, is created.

If lower and upper DBR are identical in reflection, an optical resonance is formed in the centre of the stopband and has a transmission of 1 in the case of no losses. The transmission forms a Lorentz like peak with a broadening depending on the reflectivity of the DBRs. Fig 2.11 presents the transmission spectra of an empty cavity following a typical design for a microcavity.

One important parameter in cavity fabrication is the quality factor (Q-factor) depending on the reflectivity of the mirrors. It characterizes the damping of the cavity resonance.

$$Q = \frac{\omega}{\Delta\omega} \tag{2.18}$$

Here $\Delta\omega$ is the full width at half maximum (FWHM) of the cavity resonance. High Q values of a few thousand are reached by using DBRs with reflectivities close to 1 reaching high photon life times. Furthermore, it increases the interaction time between the active materials and the cavity photons.

2.4 Light matter coupling

The strong coupling of light and a material resonance can form a new quasi-particle - the polariton - if the electro-magnetic field couples to a dipole excitation. Such a polariton can be formed for example in a bulk semiconductor at a crossing of the photon line and an exciton resonance. But other coupling types like between photon and phonon/plasmon is called a polariton as well. If the coupling is strong enough, an anticrossing is seen in the dispersion curves in the range, where the photon dispersion and the exciton dispersion would cross. Such an anticrossing is typical for polaritons.

Assuming a single resonance, a harmonic oscillator with negligible damping, the dielectric function can be presented as

$$\epsilon(\omega) = \epsilon_\infty + \frac{4\pi\beta\omega_0^2}{\omega_0^2 - \omega^2} \tag{2.19}$$

with β the polarizability

$$\beta = \frac{e^2 f}{m_0 \omega_0^2 V} \tag{2.20}$$

Hereby, f/V is the oscillator strength per volume. It defines the splitting distance of the upper and lower polariton branch.

In bulk inorganic semiconductors of the Wannier-Mott type the polariton dispersion approximating no k dependence of the material resonance can be calculated by solving [47]

$$\epsilon(k,\omega) = \epsilon_\infty + \frac{4\pi\beta\omega_0^2}{\omega_0^2 - \omega^2} = \frac{k^2}{\omega^2}c^2 \tag{2.21}$$

with ϵ_∞ the background dielectric constant and ϵ_0 the low frequency limit of the dielectric constant ($\epsilon(k,0)$). Hereby the dielectric function is characterized by a single resonance at ω_0 without damping. Plotting the solution as function of k leads to typical anticrossing in the polariton dispersion, presented in Fig. 2.15.

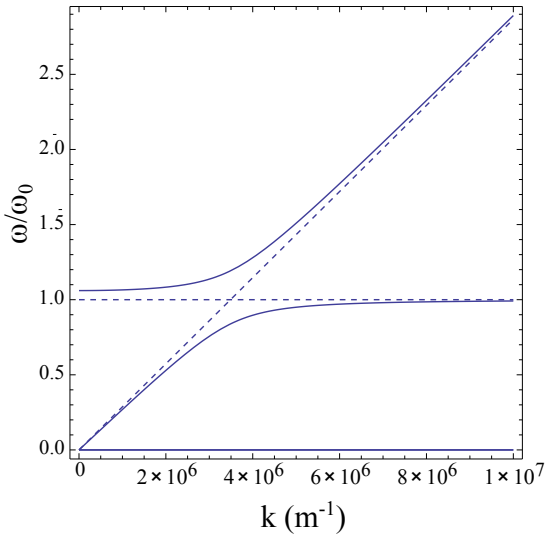

Figure 2.15: Polariton dispersion in bulk semiconductors. The uncoupled photon line and the resonance frequency ω_0 (dashed), upper and lower polariton branch (blue, solid).

The solution results in two frequency values for every k. They are named upper and lower polariton. The horizontal dashed line marks the material resonance ω_0. The other is the photon line given by $\omega = \frac{ck}{\sqrt{\epsilon_\infty}}$. The splitting of the upper polariton and the material resonance for $k = 0$ is known as longitudinal-transverse splitting.

2.4.1 Microcavity polaritons

The same polaritons can be formed in cavities, which alter the dispersion of the photon resonance drastically. Especially for an in-plane k-vector of 0 cm^{-1} the cavity photon has an energy given by the resonance condition of the cavity. This gives the bosonic polariton the possibility of condensation. This condensate emits coherent light called polariton lasing.

The splitting is often called Rabi-splitting in accordance to atomic cavities. It is connected to the Rabi-frequency of an atom emitting into a cavity mode and reabsorbing it.

The semi-classical method of using a dielectric function incorporating the resonance as oscillators is now used for a Fabry-Pérot cavity system.

Semi-classical method

This method uses a dielectric function of Lorentz oscillators to describe the material resonances. For an exciton resonance the following dielectric function can be used [47].

$$\epsilon(\omega) = \epsilon_\infty + \frac{e^2\hbar^2}{m_0\epsilon_0 L}\frac{f}{S}\frac{1}{\hbar^2(\omega_0^2 - \omega^2 - i\gamma\omega)} \tag{2.22}$$

With ϵ_∞ being the background dielectric constant, ω_0 the resonance frequency, γ the damping and f the oscillator strength per unit area S. L is the width of the active layer. Using this dielectric function to calculate the complex refractive index for non-magnetic materials ($n(\omega) = \sqrt{\epsilon(\omega)}$) in combination with a TMM, the dispersion of the polaritons can be calculated in transmission, reflection and absorption. It is a common technique for the simulation of microcavity structures. It reproduces the experimental splitting with high accuracy. It is also possible to calculate the splitting analytically in the high reflectivity limit [60]. This is presented in chapter 6 as preliminary step to a cavity design.

If we assume a $\lambda/2$ cavity with a QW in the centre (the antinode of the field), the Rabi-splitting is given by [61]

$$\hbar\Omega \approx 2\hbar(\frac{2\Gamma_0 c N_{QW}}{n_c L_{\text{eff}}})^{1/2} \tag{2.23}$$

Hereby, N_{QW} is the number of QWs, $\hbar\Gamma_0$ is the radiative width of the free exciton, which is connected to the oscillator strength per unit area, c is the speed of light, n_c is the cavity refractive index and L_{eff} is the effective cavity length [62].

$$\hbar\Gamma_0 = \frac{\pi e^2\hbar}{n_c 4\pi\epsilon_0 m_e c} f/S \tag{2.24}$$

This connects the Rabi-splitting to the oscillator strength of the material. This means for a cavity design, an increase of the oscillator strength by a factor of 2 will increase the splitting by a factor of $\sqrt{2}$, if the cavity has the same length and reflectivities. The same effect is reached with constant oscillator strength and half the cavity length.

2.4.2 Cavity polaritons in second quantization

In the following formalism the exciton-photon coupling is described by a Hamiltonian. It combines the microscopic theory of QWs coupling to the quantised electro-magnetic modes. By diagonalization of the Hamiltonian the polariton modes are obtained. Consider a QW (Wannier-exciton) in a Fabry-Pérot DBR-based microcavity, which is basically identical to the bulk [36]. The cavity only restricts the possible k values.

$$H = \hbar\omega_{\text{ex}}(k_{||})b^\dagger_{k_{||}}b_{k_{||}} + \hbar\omega_{ph}(k_{||})a^\dagger_{k_{||}}a_{k_{||}} + g(b^\dagger_{k_{||}}a_{k_{||}} + a^\dagger_{k_{||}}b_{k_{||}}) \tag{2.25}$$

With $\hbar\omega_{\mathrm{ex}}$ being the exciton energy, $\hbar\omega_{ph}$ the photon energy, $a_{k_{||}}(a^{\dagger}_{k_{||}})$ and $b_{k_{||}}(b^{\dagger}_{k_{||}})$ the exciton and photon annihilation (creation) operator, respectively. In such a structure the transverse momentum $\hbar k_z$ is conserved and the decoupling of different $k_{||}$ modes in the linear regime makes the consideration of one QW and one photon mode possible. The first two terms describe two uncoupled oscillators, the third describes the coupling with V the coupling constant.

Writing this Hamiltonian in matrix form and its basis of eigenvectors brings us to a coupled oscillator model.

$$H = \begin{pmatrix} \hbar\omega_{\mathrm{ex}} & V \\ V & \hbar\omega_c \end{pmatrix} \tag{2.26}$$

Hereby, V is the coupling constant and $\hbar\omega_{\mathrm{ex}}$ ($\hbar\omega_c$) is the resonance of the exciton (cavity). The eigenvalues of the matrix depend on the coupling constant V if they become resonant. This will produce an anticrossing with a distance of $2{*}V$ at the closest point. The squared components of the eigenvectors give a mixing of the resonances, they are also called Hopfield coefficients.

2.4.3 Coupled oscillator model

By far the simplest way to treat coupling between a cavity mode and a material resonance is by tuning one of the resonances to the other one. Therefore, a matrix Hamiltonian for two coupled oscillators can be used to describe the system. The energies corresponding to the resonance frequencies of the oscillators ($E_{\mathrm{ex}}, \hbar\omega_c = E_c$) are on the main diagonal, while the coupling constants V_1 are on the side diagonals.

$$H = \begin{pmatrix} E_{\mathrm{ex}} & V_1 \\ V_1 & \hbar\omega_c \end{pmatrix} \tag{2.27}$$

The coupling constant is connected to the energy splitting $V_1 = \hbar\Omega/2$ and the resonance energies depend on the in-plane wavevector or the angle of incidence. The eigenvalues of this matrix describe the lower and upper polariton branches.

$$E_{\pm} = (E_1 + E_c)/2 \pm \frac{1}{2}\sqrt{(E_1 - E_c)^2 + (\hbar\Omega)^2} \tag{2.28}$$

While this model can be fitted to experimental data very well and can be used to describe the polariton dispersion it has no line broadening at all, which means a coupling constant unequal 0 will always result in an anticrossing. To proof that it can be used for the distinction between the two regimes, we replace the resonance energies E_i with E-(i$\gamma\hbar$), calculate the eigenvalues and focus on the case of resonance $\mathrm{E}_1 = \mathrm{E}_c$.

From this follows:

$$E_{\pm} = \frac{1}{2}(2E_1 - i\hbar\gamma_1 - i\hbar\gamma_c \pm \sqrt{(\hbar\Omega)^2 - (\hbar\gamma_1 - \hbar\gamma_c)^2}) \tag{2.29}$$

Hereby, $\hbar\Omega$ is the splitting and γ_1 (γ_c) is the damping of the exciton (cavity). We recognize the condition for strong coupling in the root. Strong coupling is reached for $\mid \Omega\hbar \mid \geq \mid \hbar(\gamma_1 - \gamma_c) \mid$.

2.4.4 Weak coupling

Depending on the coupling strength between the resonances two regimes of coupling are defined. If the coupling is weak compared to the damping of the oscillators, the dispersion relations of the photon and the exciton cross and do not avoid each other.

If they overlap, an enhancement of spontaneous emission will be visible due to the shortening of the life time. This is called Purcell effect. The change of emission rate is proportional to the Q-factor of the cavity and the mode volume V_{mode}. This is the working regime of lasers like the VCSEL and sometimes is used to enhance the emission of LEDs. If the cavity is not in resonance with the material transition, an increase of the cavity lifetime is reached, partially suppressing the spontaneous emission.

The criterion for weak coupling is given by the absence of a Rabi-splitting [60].

$$2 \cdot V \leq (\gamma_c - \gamma_1) \tag{2.30}$$

2.4.5 Strong coupling

If the light matter coupling is strong, the frequencies of the photonic and excitonic oscillator do not cross each other. A typical anticrossing in the energy dispersion is observed. The anticrossing is visible in different measurement techniques. Depending on the sample parameters the splitting is different for transmission, reflection, absorption and photoluminescence [60].

The spectral splitting is different for all these measures, being smallest for absorption, but not always accessible in experimental observation. Hereby, measuring the transmission can be difficult depending on the transparency of the substrate or because of geometrical difficulties, if the sample has to be in a cryostat system during the measurement. The condition for a splitting in absorption is

$$V^2 > \frac{\gamma_{\mathrm{ph}}^2 + \gamma_{\mathrm{ex}}^2}{2} \tag{2.31}$$

For sufficient Q-factors the difference between absorption and reflection is small and is therefore often used as evidence of the strong coupling regime.

A very high reflectivity should always be beneficial if ideal mirrors are used. In contrast, the increased cavity lifetime makes scattering events more likely. The scattering on

impurities and layer roughness influence the spectra stronger for high Q-factor cavities. It can also be difficult, in case the cavity reaches such a sharp resonance that its width is smaller than the spectral resolution available in the experimental geometry. As shown in Fig. 2.11 the resonances lose contrast.

In chapter 5 samples using DBRs with such characteristics will be introduced. Tests for production of higher Q-factor cavities using evaporated layers of our active material in combination with DBRs of increased layer pairs are presented in section 3.2.2.

This is also the reason why the main investigations of organic materials were first done in metal or half metal cavities. They are easier to produce and have less chance of damaging the organic molecules by oxidation or desorption from the surface [63, 64, 65, 66, 67]. For inorganic materials the coupling constant is normally lower making higher reflectivity mirrors and low damping of the material oscillator necessary. To reduce the material damping high crystal quality is needed, which is quite difficult to realize on metal layers used as bottom mirrors. Furthermore, the DBR production was already at high quality due to the techniques developed for VCSEL production. For materials such as GaAs QWs the strong coupling regime can be reached with coupling constants of only a few meV [68, 69], if the Q-factor of the cavity is high enough and the damping of excitonic resonance can reach values lower than 1 meV at low temperature [70]. That means for a proof of concept, that strong coupling can be achieved, lower reflectivities can be chosen. For the investigation of polariton lasing and parametric amplification [71] the losses have to be reduced further. So it makes sense to use DBRs instead of metals even for low Q-factor cavities since they have at least the potential to reach higher reflectivities.

In some cases an intermediate range is defined in the coupling range between the Rabi-splitting and the absorption splitting. It is sometimes also called the “no ringing” regime [72]. In the case the cavity damping is quite close to damping of the material resonance the condition for the Rabi-splitting can be fulfilled but no splitting in absorption is reached.

$$(\frac{\gamma_{\mathrm{ph}} - \gamma_{\mathrm{ex}}}{2})^2 < \Omega^2 < \frac{\gamma_{\mathrm{ph}}^2 + \gamma_{\mathrm{ex}}^2}{2} \tag{2.32}$$

This gives a possibility to measure a splitting in transmission but not reaching the strong coupling regime. In Fig. 2.16 the regimes are drawn as function of the relative damping to coupling constant ratio. The red area represents the strong coupling, the blue the weak coupling and the white area is the intermediate regime.

Let us assume a high Q-factor cavity with an active material with ten times stronger coupling constant than the line width ($\gamma/V \approx 0.1$). This confines the figure to one vertical line, where only a small area for the intermediate regime is present. At a material damping of about 2 times the coupling, the weak coupling regime is reached and below 1.4 V the strong coupling is present.

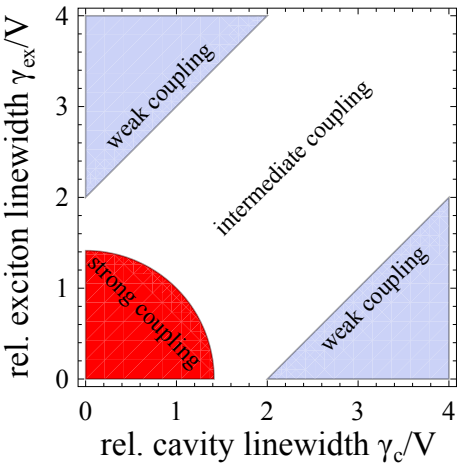

Figure 2.16: Different regimes of coupling depending on the cavity damping or the material resonance damping relative to the coupling constant. Three regimes are visible: Strong coupling (red), weak coupling (blue) and the intermediate regime with similar dampings for both resonances.

3 Experimental techniques

This chapter will give an overview of the experimental techniques for sample fabrication, characterization and measuring. Since several different experimental geometries were used in the optical experiments, only a general description of excitation sources and detection possibilities and their specification are given here. If they are used in a certain way for a single experiment, the measuring geometry will be explained in detail directly in the description of this measurement.

3.1 Sample growth and sample preparation

3.1.1 Molecular beam epitaxy

The ZnO based structures presented here are all grown by radical source beam epitaxy in a DCA-450 apparatus. The substrate crystal used in all samples is a-plane sapphire. The substrate is placed in a high vacuum chamber reaching $\approx 10^{-8}$ mbar background pressure. Elemental Zn, Mg and Cd is used in Knudson cells and is thermally evaporated. Each cell can be closed or opened separately by a magnetically driven shutter made from tantalum. To provide oxygen a radio-frequency-plasma source is used providing a mixture of molecules, atoms and ions. The beam flux of the different materials can be monitored by mass flow controllers.

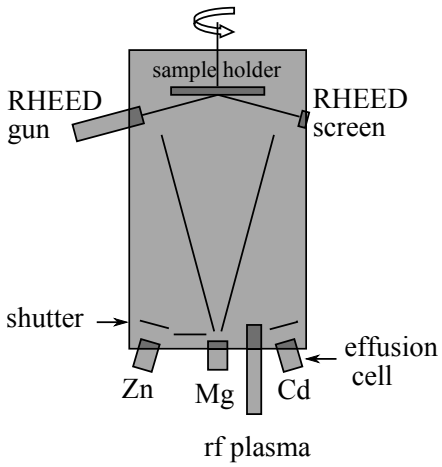

Figure 3.1: Schema of a vacuum chamber with three effusion cells for pure Zn, Mg and Cd with RHEED system for the characterization. This chamber is normally connected to other chambers for more characterization possibilities or different types of evaporation.

By using this technique highly pure crystalline structures can be produced with a high resolution in thickness. A reflective high energy electron diffraction system (RHEED) is used to characterize the crystal quality in-situ. The electrons are reflected by the surface

in a small angle and converted into light by a phosphor screen. On this screen a pattern is formed corresponding to the lattice point scattering hereby giving information about the crystal structure and morphology. The maxima of the scattering follows the Laue condition connecting the k-vector $\vec{k}_0$ of the electrons to the reciprocal lattice vector $\vec{G}$ and the reflected k-vector $\vec{k}$.

$$\vec{k} - \vec{k}_0 = \vec{G} \tag{3.1}$$

For elastic scattering $|\vec{k}| = |\vec{k}_0|$ the scattering maxima can be reconstructed by an Ewald sphere with the radius k. Everywhere it is hitting a point of the reciprocal lattice a maximum in scattering will appear in that direction. This is basically using Bragg reflection in reciprocal space. The RHEED gives a direct information of layer quality and thickness necessary to grow highly defined multilayer structures like DBRs and MQWs. The intensity of a RHEED maximum during growth oscillates, which can be recalculated to the thickness of the grown layer.

3.1.2 Electron beam evaporation

In the investigation of microcavities in chapters 5, 6 at least one of the cavity mirrors is produced by electron beam evaporation. The materials chosen are silicon dioxide (SiO_2) and zirconium dioxide (ZrO_2) because of their high refractive index contrast and their transparency to the UV limited by the absorption of ZrO_2 at 250 nm (4.96 eV).

The evaporator was build by the Kurt Lesker company. The vacuum chamber used is presented in the photograph Fig. 3.2. The setup reaches a vacuum of 10^{-7}Torr, which drops up three orders of magnitude during deposition. The layer thickness and deposition rate is monitored by a quartz micro balance (water cooled). Its readings are the input for a proportional-integral-derivative controller (PID controller) operating the current of the electron beam gun to keep the deposition rate constant. The chamber can be easily opened at the front door making sample and material changes quite convenient. The tungsten crucible holding the evaporation material is placed in a copper revolver. It has four spaces and is rotated to switch the material, keeping the evaporation cone constant for both materials. The samples are placed on a plate at the top of the chamber, which can be rotated at different speeds.

Standard parameters in dielectric mirror production involve high substrate temperatures (350 °C) and an oxygen background. Both of theses conditions are harmful for organic molecules and are avoided in the presented evaporations.

The evaporation processes were carried out at low substrate temperature of about 100 °C to ensure the stability of molecular layers prepared by spin casting or organic molecular beam deposition. In both cases higher temperatures could damage the molecular layer by either dissociation of the molecules, when using a deposited layer, or influence the mechanical stability of the spin coated polymer layer. We also refrain from using a background pressure of oxygen often used as standard for evaporation of dielectric oxides for Bragg reflectors to prevent changes of the active molecule.

Lower temperatures are possible, but heat from the glowing material in the crucible increases the temperature after a few 100 nm of depositing. This creates a gradual change of refractive index in the DBR lowering its homogeneity. Setting the substrate heating to 100 °C ensures a mostly constant temperature during evaporation.

The low sample temperature during the evaporation causes the dielectric layers to consist partially of monoxides and therefore induce different refractive indices than layers produced with high substrate heating. The layers were evaporated at a rate of 0.2 nm/s monitored by the quartz micro balance. Since values of literature could not be used for the evaporation at low sample temperature, single layers of the dielectric material were characterized by optical transmission experiments (see Sec. 3.2.1).

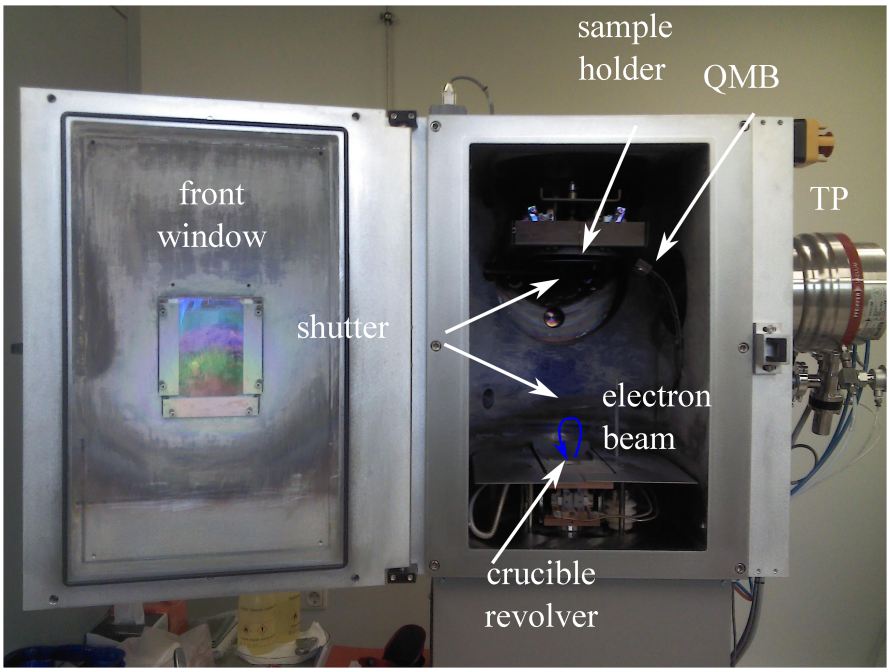

Figure 3.2: Photograph of the electron beam evaporator opened after making a DBR. The front window clearly shows an interference pattern changing its colour depending on layer thickness. The sample holder can be rotated with different velocities and heated up to 380 °C. QMB = quartz micro balance, water cooled for reproducibility, TP = vacuum turbo pump, the crucible revolver, which has four places and is rotated to ensure, that all materials will have the same evaporation cone. It is made of copper and is water cooled.

The parameters shown in table 3.1 are typical values used in the evaporation process. The chosen parameters are a compromise of layer quality and environmental restrictions needed for organic molecules to sustain the DBR deposition.

Table 3.1: Typical parameters used in DBR evaporation.

	SiO_2	ZrO_2
acceleration voltage	10 kV	10 kV
current	14 - 25 mA	65 - 120 mA
deposition rate	0.2 nm/s	0.2 nm/s
pressure during evaporation	$\approx 10^{-5} - 10^{-6}$ Torr	$\approx 10^{-4} - 10^{-5}$ Torr
ramp time	20 s	20 s
soak time	20 s	20 s

3.1.3 Spin coating

Spin coating is a technique to create thin layers from solutions. For the process a substrate is put on the holder of the spin coater. The sample is fixed, typically by a vacuum below the substrate. The sample is covered with a solution, mostly a dissolved polymer. The sample is then rotated with 20 to 60 rounds per second removing all the excess material from the surface. This creates a surface with high flatness and nearly constant thickness. The spin coater used for sample fabrication was a Schaefer Technologie GmbH SCI-20 with adjustable top speed.

The technique is commonly used in electronics fabrication to spin coat photo resists as basis for photo lithography. By adjusting the polymer concentration and rotation speed a variety of layer thicknesses can be produced.

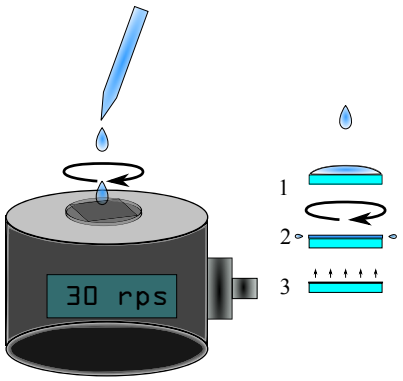

Figure 3.3: Typical geometry for spin coating, which can be separated in three steps: 1. applying the solution, 2. rotation to create a smooth surface and remove excess solution, 3. evaporation of the solvent to create the layer.

Two different polymers, polystyrene and Zeonex 480, are used as matrix for organic molecules depending on further fabrication steps.

3.2 Optical characterization

The optical characterization involved transmission (T), reflection (R) and photoluminescence (PL) spectroscopy. The techniques used were individually chosen to investigate certain aspects of the sample characteristics. Transmission and reflection measurements were used for investigation of layer thickness and refractive index of dielectric layers.

Furthermore, it was used to determine the magnesium content of ZnO alloys and the absorption of active layers. For the investigation of the emission, the samples were optically pumped by laser sources or a 75 Watt xenon lamp with a double monochromator (Gemini 180 Oriel) with two gratings with 1200 lines per mm. The pump sources using laser light were either high repetition lasers of about 80 MHz, with short pulses of 12 ps or 0.2 ps, or a high energy system with repetition rates of a few Hz. The following section explains each technique in detail.

3.2.1 UV-VIS spectroscopy

As a standard characterization method a widely automatic UV-VIS spectrometer (Shimadzu UV-2101PC) was used. It provides a highly reproducible technique for transmission measurements at room temperature. It uses a tungsten lamp for the wavelength range from 360 to 900 nm. For the UV range a deuterium lamp is used as a light source. Both lamps can be automatically changed at the entrance slit of the double monochromator for wavelength selection. The whole scanning rage is 190 to 900 nm. The resolution can be changed and reaches a minimum of 0.1 nm.

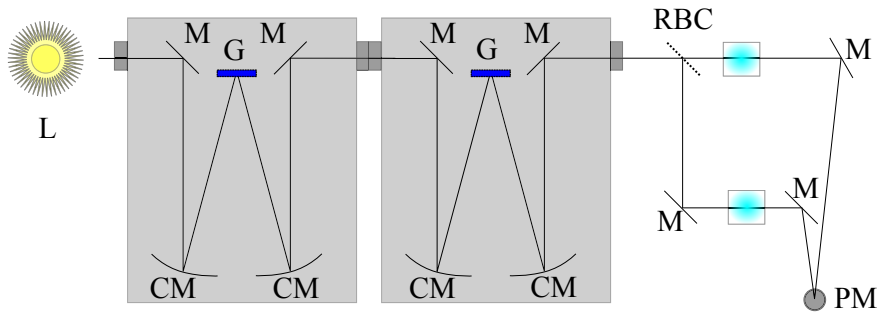

Figure 3.4: Schema of a typical UV-VIS spectrometer optimized for measurement of absorbing solutions. L = Light source, M = Mirror, CM = Curved Mirror, G = Grating, RBC = Reflective Beam Chopper, PM = Photomultiplier.

3.2.2 Thickness calibration of the electron beam evaporator

Because we used the electron beam evaporator in the low temperature regime, a calibration of the optical thickness was necessary. The standard apparatus for this task would be an ellipsometer with spectral resolution. Such a device was not available at all times so the UV-VIS spectrometer was used to calibrate the layers by evaluating its reliable transmission measurements. This spectrometer was used for the calibration of layer thickness by fitting the analytic expression for the transmission of a three layer system to the Fabry-Pérot oscillations of a dielectric layer on sapphire (the following calculation is based on a lecture of Bo E. Sernelius [73]). The Fresnel formula for the transmission and reflection coefficients with an angle of incidence of 0° is used.

$$t_{ij} = \frac{2n_i}{n_i + n_j} \qquad r_{ij} = \frac{n_i - n_j}{n_i + n_j} \tag{3.2}$$

The phase difference between a beam reflected at the first interface and a beam reflected at the second interface is given by

$$\delta_2 = \frac{2\pi d_2 n_2}{\lambda} \tag{3.3}$$

The transmission coefficient is then given by (n_1 is air, n_2 the evaporated layer and n_3 the substrate)

$$t = \frac{e^{i2\delta_2} t_{12} t_{23}}{1 + e^{i2\delta_2} r_{12} r_{23}} \tag{3.4}$$

To calculate the transmission we also need the substrate air interface but assume a thick substrate so the back reflection phase can be neglected.

$$T_s = 1 - (\frac{n_3 - n_1}{n_3 + n_1})^2 \tag{3.5}$$

For a single dielectric layer on a substrate the transmission T is obtained

$$T = \frac{n_3}{n_1}|t|^2 T_s = \frac{n_3}{n_1}|\frac{e^{i2\delta_2} t_{12} t_{23}}{1 + e^{i2\delta_2} r_{12} r_{23}}|^2 \cdot (1 - (\frac{n_3 - n_1}{n_3 + n_1})^2) \tag{3.6}$$

This formula was programmed into a Mathematica script using wavelength dependent refractive indices modelled by the Cauchy formula for the evaporated layer and the substrate.

$$n(\lambda) = A + \frac{B}{\lambda^2} + \frac{C}{\lambda^4} \tag{3.7}$$

The refractive index of air (n_1) was set to 1. Since an automatic fit routine was unreliable, the parameters were put in a "Manipulate" function of Mathematica to match the simulated transmission to the measured one as close as possible by eye.

The plots in Fig 3.5 represent transmission spectra of SiO_2, ZrO_2 (left) and a polystyrene film on a sapphire substrate (right). The precision of this technique is strongly dependent on the layer thickness, since the method relies on the minimum to maximum difference of transmission to adjust the refractive index. While the thickness is then adjusted with this refractive index to the oscillation period, it is strongly dependent on the number of oscillations visible. This makes this method more precise for thicker layers.

For the quartz micro balance calibration single layers of the dielectrics were deposited on sapphire with a thickness of 0.5 to 1 μm. The graph seen in Fig. 3.6 shows in detail the influence of the substrate heating on the refractive index and layer thickness of ZrO_2.

After the investigation of about 20 samples, the typical refractive indices were set as the Cauchy formulas (3.9, 3.10) and for the sapphire substrate (3.8). They are plotted in Fig. 3.7.

$$n_s(\lambda) = 1.75 + \frac{0.65 * 10^{-14} m^2}{\lambda^2} \tag{3.8}$$

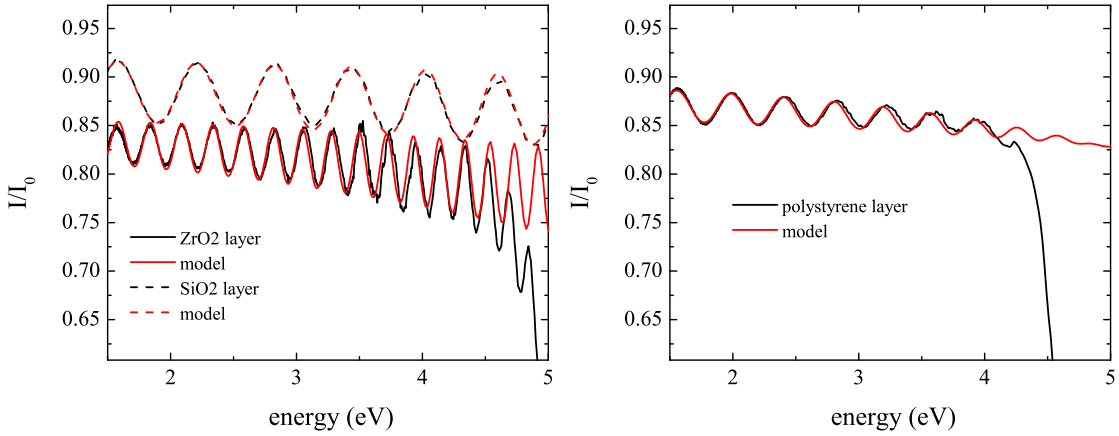

Figure 3.5: Measurement and model for the Fabry-Pérot oscillations of a three layer structure. The refractive index used is presented later. The thickness was adjusted to be 1.218 nm for ZrO_2, 675 nm for SiO_2 and 856 nm for polystyrene. For ZrO_2 the absorption at 4.9 eV causes a mismatch to the model, where no absorption is taken into account. For polystyrene the absorption starts at even lower energies of $\approx$ 4.5 eV.

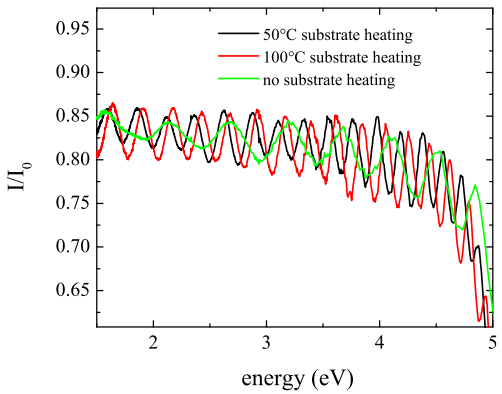

Figure 3.6: The spectra show a comparison of two ZrO_2 layers with the substrate heating at 50 °C (black) and 100 °C (red). The measurement of an evaporated layer, with half the thickness without any heating can not be compared directly. Only the difference in oscillation contrast makes the lower refractive index visible.

$$n_{SiO_2} = 1.45 + \frac{0.2 * 10^{-14} m^2}{\lambda^2} + \frac{1.05 * 10^{-28} m^4}{\lambda^4} \tag{3.9}$$

$$n_{ZrO_2} = 1.89 + \frac{1.71 * 10^{-14} m^2}{\lambda^2} + \frac{0.01 * 10^{-28} m^4}{\lambda^4} \tag{3.10}$$

$$n_{PS} = 1.61 + \frac{1.2 * 10^{-14} m^2}{\lambda^2} + \frac{2.15 * 10^{-28} m^4}{\lambda^4} \tag{3.11}$$

Figure 3.7: Refractive index of the substrate n_s (dashed line), the SiO_2 layer (solid line) and the ZrO_2 layer (dotted line).

The UV-VIS spectrometer was also used to determine the mirror transmission with stopband width and position. Fig. 2.14 presents the transmission spectra for a SiO_2/ZrO_2 based mirror with 6.5 layer pairs on sapphire. It can also be used to determine absorption of the active layer, if the sample is not too complex, by measuring both transmission and reflection. It is therefore an alternative for spectral resolved ellipsometry.

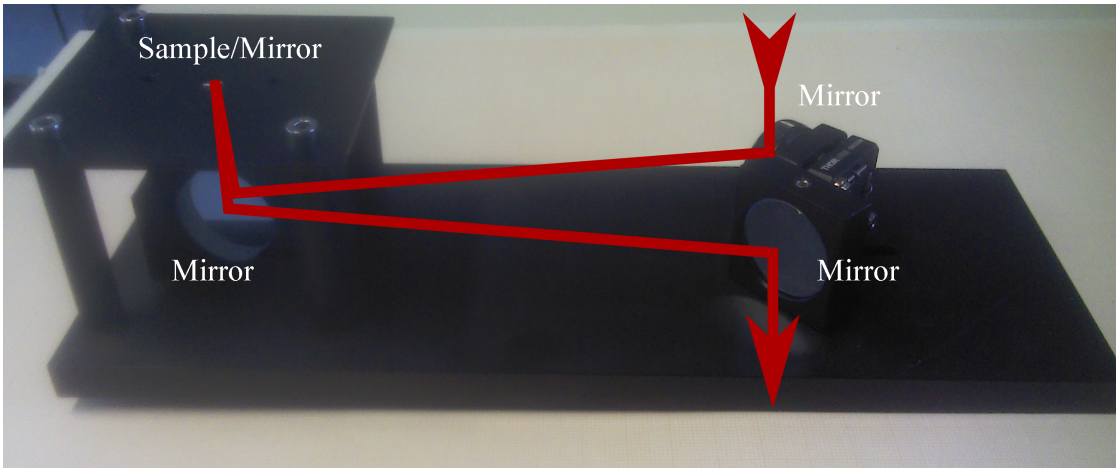

Figure 3.8: Photograph of the insert designed for reflection measurements with the UV-VIS spectrometer.

To have a possibility of measuring the reflectivity of a sample on mainly equal conditions we fabricated an insert to the spectrometer to measure the sample at a given constant angle close to zero. The Fig. 3.8 shows a photograph of the insert consisting on three UV enhanced aluminium mirrors. The insert gives us the possibility to measure the sample at a constant angle of $\approx 6°$. The horizontal sample plate is connected to the metal rods with screws pressing the plate onto metal springs making live adjustment of the reflection signal possible. The design of the insert was done in cooperation with M. Stange, our student worker, who made the technical drawings for the fabrication in the workshop of the institute of physics. To measure the baseline an UV enhanced aluminium mirror serves as reference. Its reflectivity is known from the data sheet of the Thorlabs company and tested with a sapphire substrate as reference. Fig. 3.9 presents an example of a dielectric mirror measured in transmission and reflection. The oscillation left over in the sum of both curves are an effect of the different angle of incidence (0° in transmission, 6° in reflection).

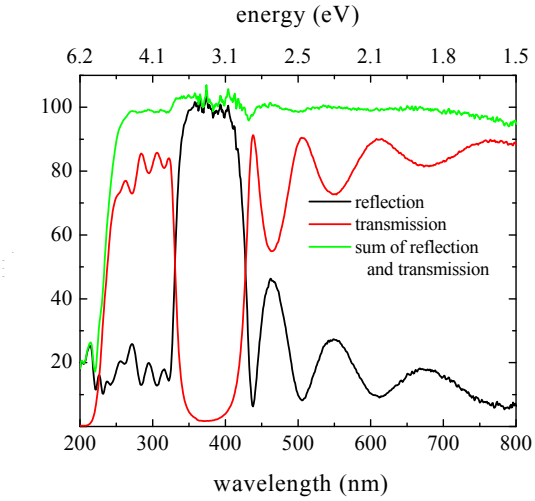

Figure 3.9: Transmission (red) and reflection (black) of a dielectric mirror measured with the UV-VIS spectrometer. For a test both curves were summed (green) to prove that they are 1 in the areas without absorption.

Angular resolved transmission and reflection

Angular resolved transmission and reflectivity is the most commonly used technique for the investigation of light matter coupling in microcavities. The experimental setup was build with a white light source that was closely placed to an adjustable pinhole which was pictured on the sample by using a 100 mm lens far away from the pinhole. A second pinhole is used to reduce the divergence of the beam. The 200 mm lens is not necessary and was just added to collimate the beam making the change of light sources more convenient. The sample was placed on a goniometer table, which allowed rotation of the

sample with a resolution of about 0.5°. The same angular resolution is reached for an optical fibre freely adjustable in distance and angle. The light reflected or transmitted of the sample is collected by blank optical fibre with no collection optics. The other fibre end is pictured by a 60 mm quartz lens on the entrance slit of a Princeton Applied Research monochromator with 500 mm focal length.

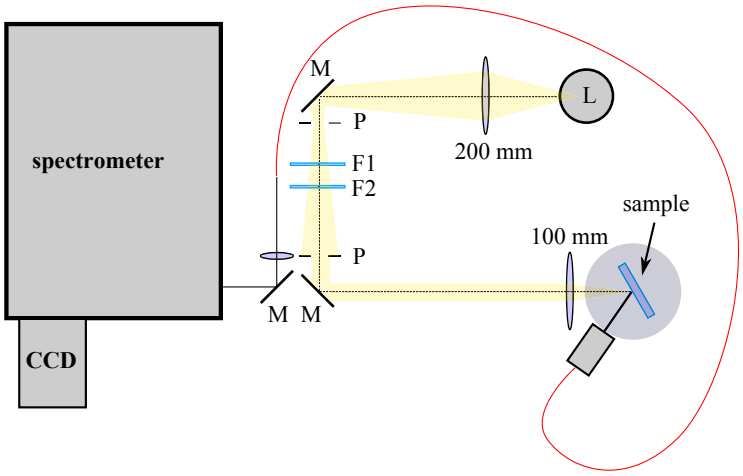

Figure 3.10: Experimental setup for angular resolved reflectivity and transmission. L is the light source, M the mirrors, F the coloured glass filters, P the adjustable pinholes and the two quartz lenses are marked by their focal length.

Two light sources were used in the experimental setup shown in Fig. 3.10. Mostly a tungsten lamp (100 Watts) was used because of its high stability, but it could only be used in the wavelength range above 350 nm. If necessary a xenon lamp (75 Watts) was used for the shorter wavelength range. In both cases colour glass filters were used to adjust the intensity distribution in the measured range. Before every measurement the light beam through the pinholes was adjusted to a constant height from the table and the sample back reflex falls back into the incident beam. Then the fibre end was placed in the beam path after the sample was displaced. The pictured pinhole was adjusted in a way, that the spot size on the sample was below one mm and a flat field of lamp and filters was used to correct the lamps intensity distribution. Fig. 3.11 gives an exemplary lamp spectrum used as flat field for the transmission and reflection measurements. In general, the xenon lamp is more suited for the used wavelength range, but it is less stable over time and their high pressure bulbs have a short lifespan. So for measurements, where the lowest needed wavelength is $\approx$ 350 nm (3.54 eV), the tungsten light source was chosen. The two light sources could be changed easily if needed, even during a low temperature measurement.

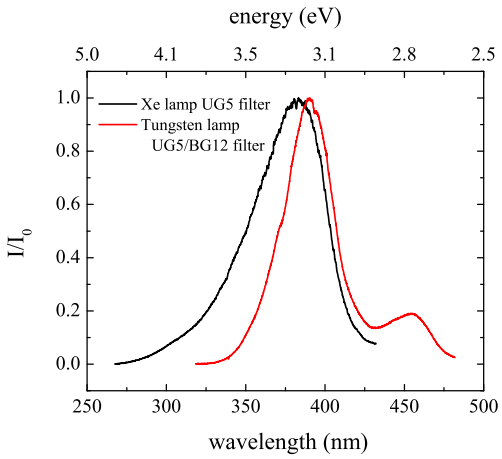

Figure 3.11: Normalized spectrum of a xenon lamp with an UG5 UV filter (black) and a tungsten light source spectrally shaped by an UG5 and BG12 filter (red). Both spectra are **not** spectrally corrected for the detection response, because the losses in the fibre, monochromator and the CCD are important here.

Backfocal plane imaging

Even if this technique was only used in test measurements, the following lines give a short introduction to this experimental method of back focal plane imaging, because of its importance in the area of microcavity polaritons. The technique is a convenient method for angular resolved reflection or photoluminescence measurements. Instead of measuring every angle separately a microscope objective with sufficiently large numerical aperture is used in combination with an imaging spectrograph. Now the microscope objective is adjusted so that the sample is directly in the focal plane. Thereby the different angles are converted to circles around the centre beam of the objective. This is imaged on the entrance slight of the spectrometer. The CCD chip is read out as a 2D image giving spectral and angular resolution (different lines of the CCD chip) at the same time.

The benefits of this technique are quite obvious. Only one image is needed for all angles and there is no risk of mechanical instabilities by the movement of the sample. This technique has also some limitations. Most problematic is the limitation to a maximum angle, depending on the microscope objective, i. e. a numerical aperture of 0.5 gives only a maximum angle of $\pm$ 30°. For a high angle of incidence the technique can not be used with such an objective. An objective with high numerical aperture would help to increase the tuning range. Since the measurements are planed to be possible also at low temperature, the distance to the sample limits the possible numerical aperture.

A second limitation is that the resolution depends on the number of lines on the CCD chip.

Fig. 3.12 shows this measuring technique on a high quality cavity using an evaporated layer of L4P inside the cavity, detuned strongly to the red.

3.2.3 Measurements at cryogenic temperatures

For all measurements presented in this thesis cooling to either nitrogen or helium temperature was possible by using a cryostat. For measurements with a stationary sample

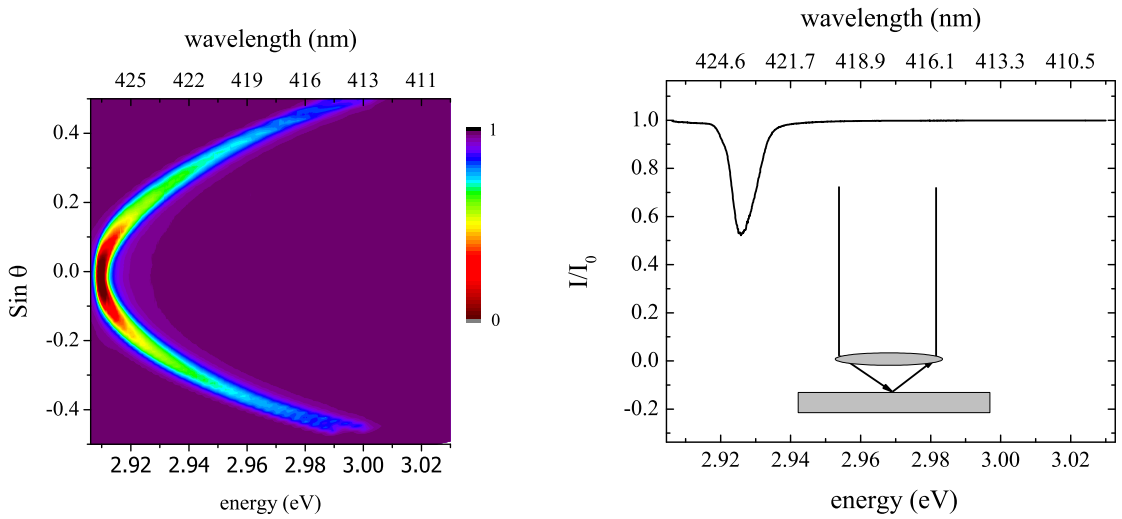

Figure 3.12: Left: Angular resolved reflectivity created by back focal plane imaging with 20x microscope objective of 0.5 NA. Right: An exemplary spectrum collected by one single line of the CCD chip.

a bath cryostat was used. For measurements where the sample had to be positioned differently during the measurement a flow cryostat was used. Because of its smaller size the flow cryostat can easily be mounted on a translation stage and goniometer table. It was mainly used for low temperature transmission and reflection experiments.

The bath cryostat used in the experiments was custom build by the "Klaus Schaefer Gesellschaft fuer Verfahrenstechnik mbH" with three quartz windows of optical access. Since the window to sample distance is fixed to ≈ 3.5 cm, reflection and PL measurements are only possible in a small angular range or by using two different windows of the cryostat. Since a wide angular range can not be probed, a cryostat with smaller distance to the window is beneficial for such experiments.

For this purpose a flow cryostat was used, which was build by Oxford Instruments (Model MicrostatHe2) and is well suited for angular resolved measurements. The cryostat has two quartz windows and the cooling finger is build to bring the sample close to the front window, which gives the possibility for reflection measurements to high angles of incidence of more than 75°. One window of the cryostat is 2 cm in diameter the other one is 1 cm in diameter. The back window is about 2 cm away from the sample surface, which causes the transmission to be limited to a range of 0° to 40° and since the sample is cooled by the contact to the copper holder only a hole of 2 mm in diameter can be used for the transmission experiments.

3.2.4 Excitation sources

High power density systems

For the measurement of optical gain or lasing in the different samples we use mostly high energy excitation. For this purpose a nitrogen laser (LTB Lasertechnik Berlin Model MSG 400) is available, which provides 0.5 ns pulses at a repetition rate of about 10 Hz and a maximum pulse energy of 200 μJ at 337.1 nm.

For excitations with longer pulses an excimer laser (Lambda physics LX 200) pumped dye laser was available. It was possible to use the excimer laser emission at 308 nm (XeCl) directly or use the attached tunable dye laser. As typical for such laser systems the beam profile of the excimer laser is rectangular and has a quite high divergence. The excimer laser has a repetition rate of up to 30 Hz and a pulse energy of 250 mJ. The dye laser has a pulse energy of about 500 μJ depending on the dye. The pulse length is about 20 ns for both systems.

The dye laser system was converted to an amplified spontaneous emission source for one type of measurement. The changes made to the laser system are presented before the experiment in chapter 4. The Table 3.2 gives an overview on the available laser based excitation sources.

Quasi-continuous wave low density systems

The lasers called quasi-continuous wave have a repetition rate of around 80 MHz. They are used for time-integrated PL measurements as excitation sources. The Nd:IVO_4 laser can be used at his main wavelength of 1064 nm, frequency doubled or tripled. Fine tuning of the photon energy to chose between the excitation of QW directly or via its barrier is very useful, but a tunable source is needed. For this purpose we use two synchronized dye lasers (Coherent 700 dye laser) one pumped by the frequency doubled the other one pumped by frequency tripled light. The dye lasers emit in the red and blue range, respectively. Both of them can be frequency doubled to the UV range. This might not be the most efficient excitation source but it is a very versatile and stable system. It can be used in combination with a single photon counting unit or a synchronized streak camera.

A similar system with equivalent repetition rate but shorter pulses is the titanium sapphire laser (Coherent Mira). It produces pulses shorter than 200 fs in a wavelength range from 700 to 980 nm, that can be increased using a different set of laser mirrors. Due to the short pulses the spectral width is $\approx$ 6 nm (FWHM), which has to be considered for excitation of the QWs. This emission is frequency doubled to the UV range for the investigation of the ZnO based samples.

	manufacturer	wavelength (nm)	repetition rate (Hz)	pulse energy	pulse length
nitrogen laser	Laser Technik Berlin	337.1	1-30	$200 \cdot 10^{-6}$J	0.5 ns
Excimer Laser +dye laser	Lambda physics	308 depending dye	1-30	$250 \cdot 10^{-3}$J	20 ns
Nd:IVO_4 + dye laser + freq. doubling	Spectra physics Vanguard	355 (532) depending on dye	$80.6 \cdot 10^6$	$\approx$ 30 nJ	12 ps
Ti:Sa Laser + freq. doubling	Coherent Mira	700-980	$\approx 80 \cdot 10^6$	$\approx$ 30 nJ	200 fs

Table 3.2: Table of the available laser sources used in the experimental investigations.

3.2.5 Streak camera measurements

A streak camera (Model Hamamatsu C 6580) with a single shot unit (Model M5676) was used for the time resolved measurement with the excimer laser system in quasi-steady state excitation conditions. The system can reach up to 2 ps resolution depending on the range chosen for the measurement. The system was also used for calibration measurements on the excitation sources. In the following experiments it was always used in combination with the excimer laser. The streak camera was combined with a home build Rowland-type spectrograph with a focal length of 20 cm and 1200 lines per mm grating. This combination made a spectral resolution of 0.1 nm possible. The maximum sweep range is 50 ns and can be reduced in steps to the shortest range of 0.2 ns

As an example some test measurements done for a calibration control are presented in Fig. 3.13. The emission of the Nd-laser was focused on the streak camera. Since it has a constant frequency of 80.6 MHz it places the pulses 12.4 ns apart. This can be used for the calibration of the longest sweep ranges. For the lower ranges the beam was divided in two beams with a variable delay. This technique can already be seen in the 20 ns range showing two sets of pulses delayed by 3.0 ns by a delay line of 0.9 m.

In general, it is possible to integrate over several excitation pulses to increase the signal to noise ratio. But most of the high energy laser sources and especially the excimer and nitrogen lasers we used in the experiments can not reach a temporal jitter lower than one ns. That means two excitations following each other can not be overlapped directly by the streak camera software. It could be done by fitting the pump pulses with a peak profile and shifting the temporal scale to match in a post-processing step. This was not necessary in the measurements presented here since the single shot emission was strong enough for the signal.

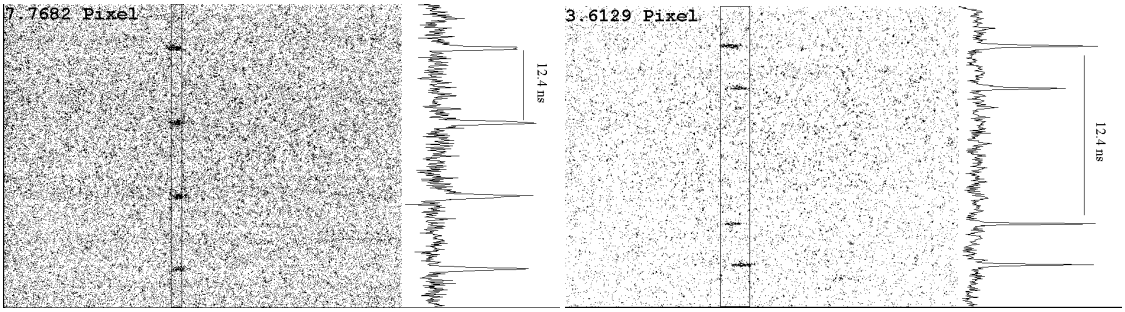

Figure 3.13: Right: Streak camera image in 50 ns range showing 4 pulses of Nd-laser. Left: Streak camera image of the 20 ns range with to beams overlapped with a time delay.

The system could also be combined with a so called synchroscan unit with a sweeping frequency of 80 MHz. This setup is typically combined with the Nd:IVO_4 laser, which was already described before, but could technically also be used with the available Ti:Sa laser system.

4 Dynamics of random lasing

This chapter presents the investigation of emission dynamics of a random laser. Measurements with simultaneous temporal and spectral resolution reveal the complex dynamics of multiple modes, while the time-integrated mode features stay constant from shot to shot. A numerical simulation is used to qualitatively reproduce the experiments. The findings are then interpreted by network theory introducing time depending weights. A network quantifier specially defined for an optical network, the phase sensitive node coherence, reveals the self-organization of the laser field. Feedback with unfitting phases is suppressed due to destructive interference, while fields between other scatterers oscillate coherently. We think, that our findings are representative at least for weakly scattering random lasers and are published in ref. [8].

4.1 Introduction

In a typical configuration a laser is composed of a gain medium providing the optical gain, and a resonator providing the optical feedback as presented in Fig. 4.1 a). In a random laser the optical feedback is realized by a scattering process. This is schematically drawn in Fig. 4.1 b). These types of lasers have attracted quite some interest in the last years, because they are easy to manufacture and cheap to produce.

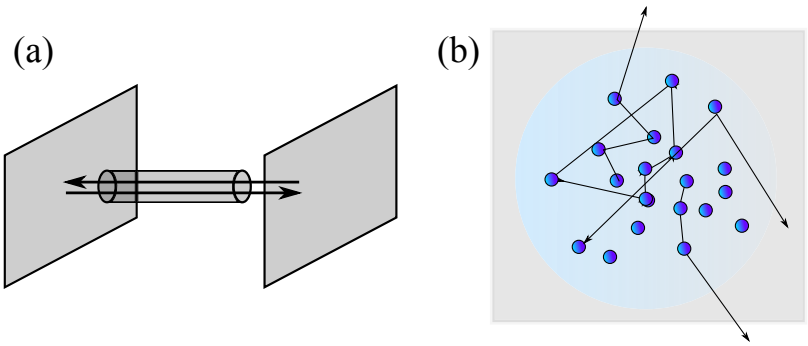

Figure 4.1: a) A Fabry-Pérot cavity with gain medium inside and two mirrors providing the optical feedback. b) A schematic drawing of a random laser is presented. The gain material is filled with scatterers and the light bounces between the scatterers back and forth amplified by the gain medium. The blue shaded area symbolizes the excitation spot.

They were first theoretically proposed in 1966 by Letokhov et al. [74, 75]. The

experimental realization was achieved later in 1986 by Markushev et al. [3] and proved the random lasing of neodymium in sodium lanthanum molybdate powders. Further structures are laser dyes with scattering particles, pellets of semiconductor powders and many more [76, 77]. A general review of random laser investigation is presented by Cao et al. [78], Wiersma [79] and a review focussing on theory by Zaitsev et al. [80]. They can be divided into samples with passive scatterers [81] and active gain material between them, or active particles in a passive surrounding [82].

Even with higher losses and lower coherence a practical use in application fields like medicine [83], speckle-free illumination of microscopes [5], other display applications (like flexible displays) and lasing paint is very promising. The random laser can find appliance in specialized fields, which can not be filled by thermal light sources or laser diodes, where their efficiency is not most important and their emission characteristics are beneficial. Even quite elaborate fabrication techniques like paper based random lasers have already been realized [84] making the printed random laser only a question of time. The chance of application in these fields has drastically increased, since electrically pumped random lasing was achieved [85, 86] with improved efficiency [87, 88].

While there is quite a lot of research on time-integrated emission of random lasers, only few works focus on the dynamics of the random lasing emission [89]. We present a dynamical investigation combined with a new approach of an optical network. Semiconductor laser physics and network theory are well developed fields of their own but their combination is scarce.

Co-lasing of multiple modes, which appear at coincidental wavelengths, is observed in many random lasers like ZnO particles [90, 91], scatterers in a laser dye [92], cold atoms [93], porous glass filled with laser dye [94], semiconductor slabs filled with air holes [4] and even human tissue [83]. A theoretical treatment of the multi-mode operation is given in [95, 96], but it is limited to a stationary state condition. Practically all experiments in random laser research are performed with (short) pulsed excitation. Due to the large pump densities of over 50 $\mathrm{kWcm^{-2}}$ that are needed to overcome the threshold a continuous wave excitation is not possible. The pulsed excitation can reach two different regimes. Hereby, one is the excitation with pulses shorter then the life time of the excited state [97], in contrast, the so called quasi-steady state excitation has pulse lengths longer than the life time. For quasi-steady state condition the excitation not only has to be longer, but also its intensity variation should be small and slow in comparison to the time constant.

By using a quasi-steady state excitation it is possible to reveal the dynamics of the random laser in each spectral feature to prove, that all modes are lasing simultaneously or alternating.

The light travelling between the scatterers seems quite naturally as a link between them, forming a network of light. A random laser as a network would bring a new point of view into this area.

As a network in general we interpret a fishnet, a spider web, a road network or a computer network. These very different things are called network because of their similar structure. They all have nodes connected by links. In science the network has an

important role as a general concept. It finds implementation in subjects like neuronal networks, like the brain, or social networks in the internet.

In laser physics this concept is applicable in the network of multiple coupled lasers. They are a realization of coupled self-sustaining oscillators, which offer an interesting area of research in dynamical phenomena [98, 99].

A random laser can also be deemed as dynamical network of light. Inside the excited area the light travels between the scatterers. This means the light is the link connecting the scattering centres, which are the nodes of the network. The light is amplified on its path, due to stimulated emission. If the amplification on such closed paths, which can be formed by several links, is stronger than the losses, it will lase during the whole excitation time, while others will decay. This makes it a self-organizing network. We call it a lasing network because the whole system of nodes and links is needed for the laser operation. The single nodes cannot lase. This system differs strongly from the network of the lasers mentioned above.

4.2 ZnCdO multi quantum well structures

The sample under investigation is a ZnCdO multi quantum well with the following design. The sample is grown on an a-plane sapphire substrate with a 650 nm thick buffer layer of $Zn_{0.65}Mg_{0.35}O$ by radical source MBE (see 3.1.1). This is followed by ten $Zn_{0.88}Cd_{0.12}O$ quantum wells separated by ZnO barriers. The quantum wells have a thickness of 2.6 nm and the barrier 7.3 nm. The sample is capped with a 225 nm layer of the buffer material (sketched in Fig. 4.4). The buffer layer and cap have a lower refractive index and act as a waveguide for the emitted light. This reduces the sample to a 2D system in the used measuring geometry. The emitting quantum wells contain 12% of Cd, which shifts the emission to the blue range at about 450 nm.

The samples are similar to those presented in the time-integrated investigation of random lasing by Kalusniak et al. [4]. The results presented there, already suggested an interesting dynamical behaviour. The different mode features presented for different integration times, make dynamical changes during the excitation very likely. Furthermore, the random feedback creates a modal gain distribution influencing the dynamics of the emission.

The scatterers in the sample are air filled holes created during growth under special conditions. They are ≈ 1 μm in size and randomly positioned over the whole sample. The investigated sample has a scatterer density of a few hundred per mm^{-2} making the mean free path a few millimetres long. This is much more than the wavelength and even surpasses the excited area on the sample. This means we are in the weakly scattering regime. While lasing capabilities of such structures have been investigated previously [4] we focus now on the dynamics of the random laser.

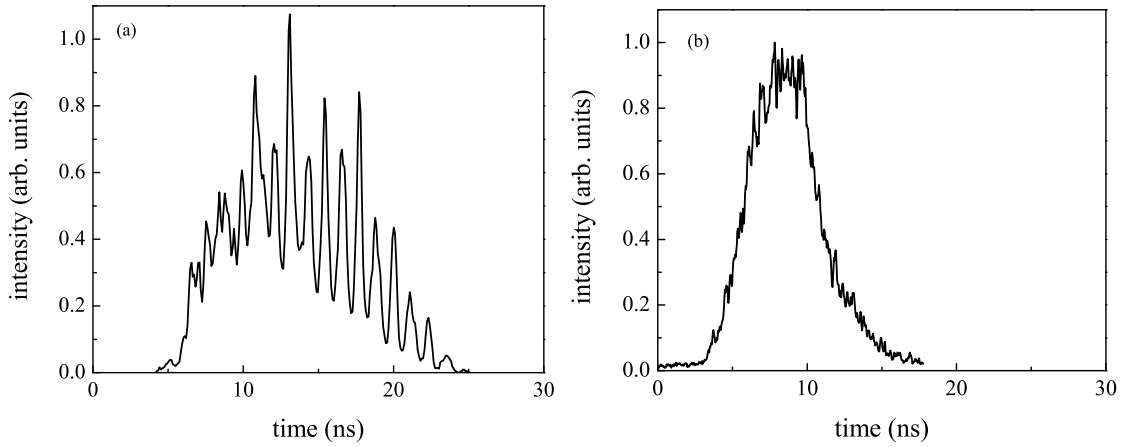

Figure 4.2: Comparison of the standard dye laser to a home build ASE source: a) Temporal profile of the dye laser measured with the streak camera, showing extreme spiking with a period of a few 100 ps. b) Temporal profile of the ASE source using the DMQ laser dye with a smooth temporal profile. Without a spectral selection the source can only be tuned in steps depending on the dye.

4.3 Experimental method

The experimental investigation is based on time and spectral resolved characterization of the emission dynamics during quasi-steady state excitation. As detection a streak camera with a small spectrograph, placed in front of the photo cathode, was used for temporal and spectral resolution in a single shot measurement. The high density excitation source available was an excimer pumped dye laser with pulses of about 20 ns. During calibration measurements it was obvious that the temporal spiking of over 60% would not provide the smooth temporal profile needed in the experiments.

It could not be used as a steady state excitation source. Intensity fluctuation during the laser pulse is common for high energy pulses and there has been put a lot of effort to suppress spiking [100]. To achieve an excitation with a temporally smooth profile for our experiments an amplified spontaneous emission source was constructed. A 6 cm dye cuvette is pumped by the excimer laser (see 3.2.4) focused to a stripe. To enhance the emission, one single laser mirror for 355 nm was placed at the end of the cuvette. Fig. 4.2 presents a comparison of the temporal profile of the dye laser (a) and the amplified spontaneous emission (ASE) source (b) measured with the streak camera. Fig. 4.3 shows the excitation system to create the ASE pulse and its emission spectrum. This ASE source follows the temporal shape of the excimer laser, which was generally smooth, but changed a little depending on the excimer gas quality. This explains the difference in pulse length. A live temporal characterization during all measurements is therefore necessary for comparison of the pump and emission pulse for every streak camera image.

The emission of the ASE is collimated by a 600 mm lens and focussed on a variable slit by a combination of a spherical and cylindrical lens. The slit is then pictured on the

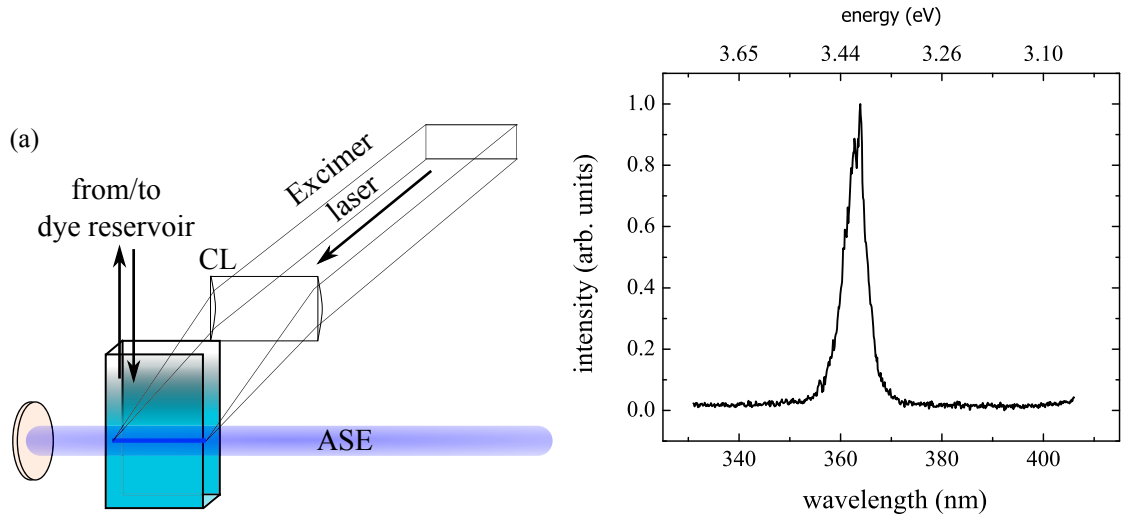

Figure 4.3: Left: Geometry of the ASE excitation source with DMQ as the active dye. Right: Spectrum of the emitted ASE with no spectral selection of the emission centres at 363 nm (3.42 eV) with FWHM of less than 6 nm.

sample surface to a stripe of 2 mm x 0.5 mm near the sample edge to reduce the risk of scattering losses on the way through the sample to the detection system. The emitted light is collimated by an 80 mm lens and focussed on the spectrograph by an identical lens. The spectrograph in front of the streak camera is a Rowland type with a 1200 lines/mm concave grating and a resolution better than 0.1 nm. The streak camera is a Hamamatsu C 5680 with a fast single sweep unit (M5677) with a maximum temporal resolution up to 2 ps. The resolution changes with the time range in use and is $\approx$ 0.5 - 1% of the selected sweep time. To characterize the excitation, a sapphire substrate is used as a beam splitter to couple out $\approx$ 15% of the pump beam, which is directly imaged on the photo cathode of the streak camera, without spectral resolution. The beam path is build to the same length, so both signals reach the streak camera at the same time. The time shift introduced by front and back reflection on the beam splitter is only $\approx$ 3 ps and therefore unproblematic in our measurements.

The camera is triggered by a TTL signal from a computer triggering the excimer laser as well. Since the laser pulse is delayed almost a μs to the triggering signal, the delay line of a HP pulse generator (HP 8082A) is used to overlap sweep time and detection. The whole system is sketched in Fig. 4.4.

Not shown in the schematic drawing is the bath cryostat housing the sample, which gives us the possibility to measure at temperatures from 4 to 300 K.

Fig. 4.5 presents a streak camera image and three methods to look at the given information in more detail. This provides us with a spectral resolution of 0.1 nm and a temporal resolution of $\approx$ 0.1 ns. The measurements presented in [97] reach similar spectral and temporal resolution, but since a picosecond excitation source is used, it

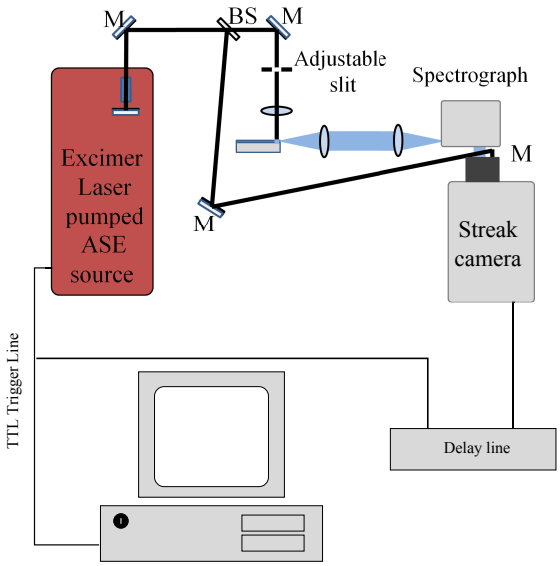

Figure 4.4: Schematic drawing of the measuring geometry for time resolved single excitation measurements of random lasers.

represents the opposite time regime for excitation pulses. In every measurement the temporal evolution of the excitation pulse was simultaneously measured at the edge of the photo cathode, but without spectral resolution. This was necessary to make sure that temporal features of the emission are not simply an artefact created by temporal spikes of the excitation.

A series of different pump fluences was also investigated resulting in a laser threshold of ≈ 5.5 mJcm^{-2}. The panel a) of Fig. 4.5 presents a typical streak camera measurement at a pump fluence of about 10 mJcm^{-2}, which is about twice the threshold. A change of the excited area resulted in different mode features and different emission intensities while the general characteristics stayed.

The exemplary streak camera image in Fig. 4.5 is further separated in different graphs highlighting a certain aspect of the emission. Their temporal profile integrated over all wavelengths is presented in panel b) (red) and for comparison the excitation pulse (black). Panel c) presents what we call time slices of 0.7 ns. It is a stepped integration of this time intervals to visualize the changes of the spectrum over time. Two modes in these spectra are marked and their temporal profile is presented in panel d). The red marked feature starts earlier and ends later, while the black marked one starts later but surpasses the other ones intensity by a factor of two. The detailed investigation shows co-lasing of several modes. Their temporal envelope is different for each mode.

This, of course, is one isolated excitation. The next one could alter this behaviour dramatically.

To prove that these are characteristic features, nine different shots with an excitation fluence of 9-10 mJcm^{-2} are compared in Fig. 4.3. By using highly reproducible, stable

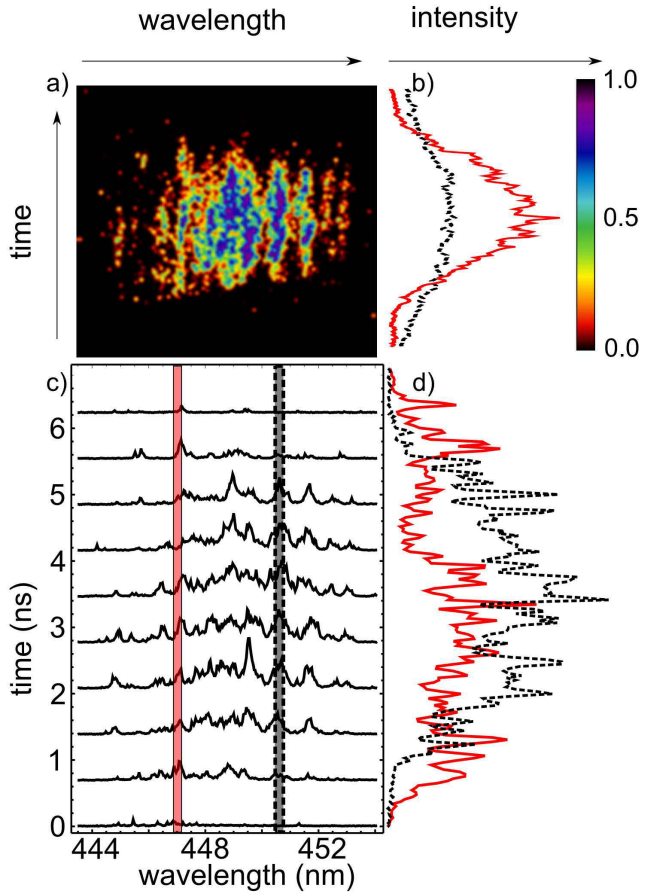

Figure 4.5: a) Typical streak camera image of a single excitation pulse smoothed by a Gaussian filter over two pixels for better visibility. The normalized intensity is linearly colour coded for low (black), middle (green) and high (blue) intensities. b) Spectrally integrated temporal profile of the pump pulse (black) and the emission (red). c) so called time slices integrated over 0.7 ns (0 ns to 0.7 ns, 0.7 ns to 1.4 ns, ...). d) Temporal profile of the marked modes in c) without any averaging.

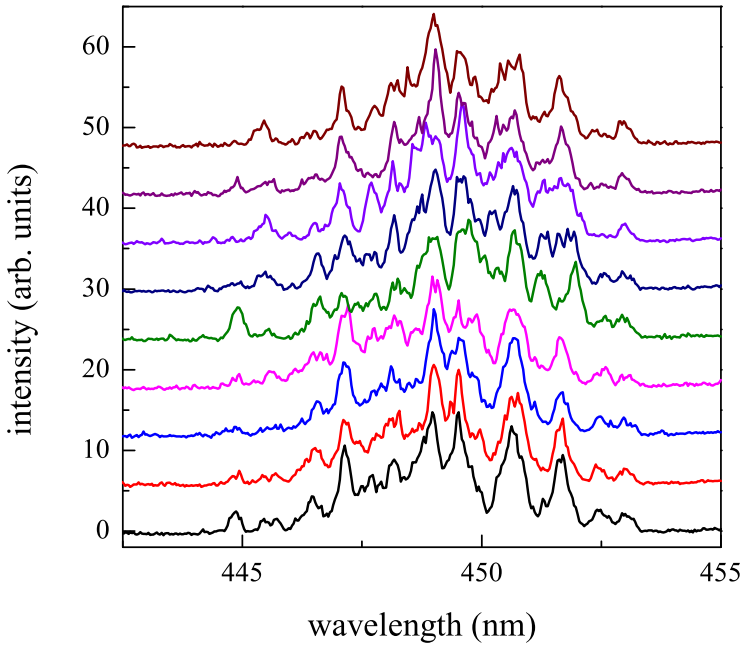

Figure 4.6: The time-integrated emission spectra of nine different excitations of the sample under identical focus and detection conditions, with a pump fluence of 9 - 10 mJcm^{-2}, shifted for clarity.

excitation pulses and a constant scatterer configuration, reproducible spectral features are observed. From this follows, that the features of the spectra are depending on the scatterer positions. This fits to the numerical simulation used to qualitatively reproduce the experiment, which will produce the same spectral features for a constant scatterer configuration. The used model is explained in the following section.

4.4 Numerical simulation

The modelling of such a random laser structure poses some difficulties. Solving the Maxwell-Bloch type equation directly is limited to a small sample size of a few hundred λ^2 [101, 102, 103, 104]. The scale of our experimental configuration is much bigger, over 10^7 λ^2. To tackle this problem we approximate based on the large distance of the scatterers. A second problem arises from the fact, that the actual scatterer configuration during the experiment is unknown and can not be mapped. Therefore multiple different configurations are modelled. A characteristic example is presented to demonstrate their common features.

N scatterers are placed in a planar waveguide. They are connected by $2N(N\text{-}1)$ optical paths (in-plane) through the gain medium. The field was only investigated on the so called rays connecting the scatterers. The amplitude of the light travelling on such a one dimensional ray from scatterer i to j is given by

$$E_{ij}(z,t) = \mathrm{Re}\left\{\mathcal{E}_{ij}(z,t)G(kz)e^{-i\omega_0 t}\right\} \tag{4.1}$$

where z is the position on the ray and G the far-field 2D Green function given by

$$G(kr) = \frac{e^{ikr+i\pi/4}}{\sqrt{8\pi kr}} \tag{4.2}$$

It describes a static amplification including the phase shift of the scattered wave in the medium. This medium is characterized by the background values for the refractive index $\bar{n}$, gain $\bar{g}$ and losses α_0. All these values are effecting the complex wave number k given by

$$k = \frac{\bar{n}\omega_0}{c} - \frac{i(\bar{g}-\alpha_0)}{2} \tag{4.3}$$

The dynamics of the simulation is based on a propagation equation for the slow varying amplitudes and the time dependent equation for the gain distribution. These two equations build the core of the simulation:

$$(\partial_z + \frac{1}{c}\partial_t)\mathcal{E}_{ij}(z,t) \quad = \left[\tfrac{1-i\alpha}{2}(g(z,t)-\bar{g}) - \tfrac{\alpha_0}{2}\right]\mathcal{E}_{ij}(z,t) \tag{4.4}$$

$$\tau_n \frac{d}{dt} g_d(t) \quad = g_0(t) - g_d(t)\,[1 + S_d(t)] \tag{4.5}$$

The equation (4.4) describes a plane wave travelling on the ray, which is a good approximation, as long as the distance between the scatterers is large $\approx 10\mu$m, so wavelength and scatterer size ($\approx 1\mu$m) are small in comparison. It incorporates the standard amplitude phase coupling known in semiconductor lasers [105].

The rate equation (4.5) is used to calculate time and space dependent gain. Hereby, τ_n is the inversion lifetime, $g_0(t)$ the unsaturated gain or pump term and S_d the average intensity of domain d. The gain equation separates the excited area in different domains of constant gain. This takes into account, that sub-wavelength variation, due to multi-wave interference, are smoothed by the charge carrier diffusion.

This introduces spacial hole burning to the simulation, which is very likely responsible for the multimode emission. Without spacial hole burning introduced by the domains the system would lase on a single optical mode defined by the scatterers furthest apart. They have the lowest threshold gain [4].

The scattering process is introduced through the boundary condition of the equation given by

$$\mathcal{E}_{ij}(0,t) = \sum_{j'} A_{ijj'}[\mathcal{E}_{jj'}(l_{jj'},t)G(kl_{jj'}) + \beta_{spon})] \tag{4.6}$$

Hereby, $A_{ijj'}$ are the scattering amplitudes describing the scattering from ray jj' into ij. Since the scatterers are larger than the wavelength, these amplitudes are generally angle dependent (Mie scattering [106]). The spontaneous emission is simulated by a small Langevin force, while all other noise sources are disregarded.

Exemplary simulation

The simulation used less scatterers in comparison to the experimental data, 20 point scatterers randomly positioned in the 0.4 mm * 0.2 mm excitation stripe. Despite having a smaller number of scatterers and area, it is still suited because of the qualitatively similar spectral and temporal features. The other necessary parameters were chosen to be λ_0 = 450 nm centre wavelength of the emission, $\bar{n}$= 2 as background refractive index and an amplitude phase coupling of α = -5. The inversion lifetime was set to be 0.5 ns. The scattering amplitude was set to the maximum possible elastic point scattering A = 4i, resulting in a scattering process, that is isotropic and not depending on scatterer size or shape. From this follows a scattering cross-section $\sigma = |\mathrm{A}|^2\ \lambda_0\ /8\ \pi\bar{n} \approx 100\ \mu$m. With this cross-section and the scatterer density ρ of $\approx 250\ \mathrm{mm}^{-1}$ we get the mean free path $\mathrm{l}_{free} = 1/(\sigma\rho) \approx 4$ cm. If we calculate an effective reflectivity for the scatterer $R_{\mathrm{eff}} = \sigma/(2\pi L) = 4.6 \cdot 10^{-5}$, it is obvious, that such a small feedback would need a high gain to reach the threshold. It can be calculated by

$$g_{th}(L) = \frac{1}{L} ln \frac{1}{R_{\text{eff}}} \tag{4.7}$$

and reaches quite high values of over 250 cm^{-1}, which can still be realized easily in semiconductors with pulsed excitation [45]. The simulated excitation pulse is 12 ns long and increases linear to the maximum value in the first half of the pulse. Then it returns to zero decreasing with the same slope.

Fig. 4.7 shows an exemplary simulation result. a) presents the optical spectra: Black line: time-integrated spectrum in arbitrary units and log scale. It shows an irregular mode spacing typical for random lasers.

Furthermore, Fig. 4.7 a) represents the 90° turned equivalent of the streak camera image. We see multiple modes change over time qualitatively in accordance with the experiment. Even with the symmetric rise and lowering of the pump the mode spectrum is not mirrored. This indicates long time scale mode competition or multi-stabilities. The thin vertical lines divide the transient into different epochs, where certain modes are emitting. In panel b) we observe that at ≈ 1.8 ns the threshold is reached and that the mode at $\lambda = 452.6$ nm starts lasing with damped relaxation oscillations, which can be seen in the rapid fluctuations of the maximum intensity S_{max}. These oscillations are present in all simulated configurations but are not observed in the experimental data. This may be because of the limited temporal resolution in the experiment or due to underestimation of the damping of relaxation oscillation in the simulation, due to non-linear gain saturation. In panel c) the outlines of the grey area mark the maximum and minimum gain in the domains. The inset gives the geometrical representation of the gain distribution with differently coloured domains. Minimal and maximum gain differ during laser operation up to a factor of 5. This is due to the large spacial hole burning, which depletes the gain for the lasing mode and another mode takes over ($\lambda = 448.7$ nm). This is similar to Fabry-Pérot lasers with low reflectivities, which are also known for large spacial hole burning. The mode jumps are simultaneous to changes in gain and intensity. The short time variations in S_{max} are introduced by mode beating, which disappears in periods of single mode emission. They are not resolved in the experiment, due to limited temporal resolution.

The numerical simulation gives a qualitative representation of our experimental system, so that the simulation data can be used as input for a network theory approach.

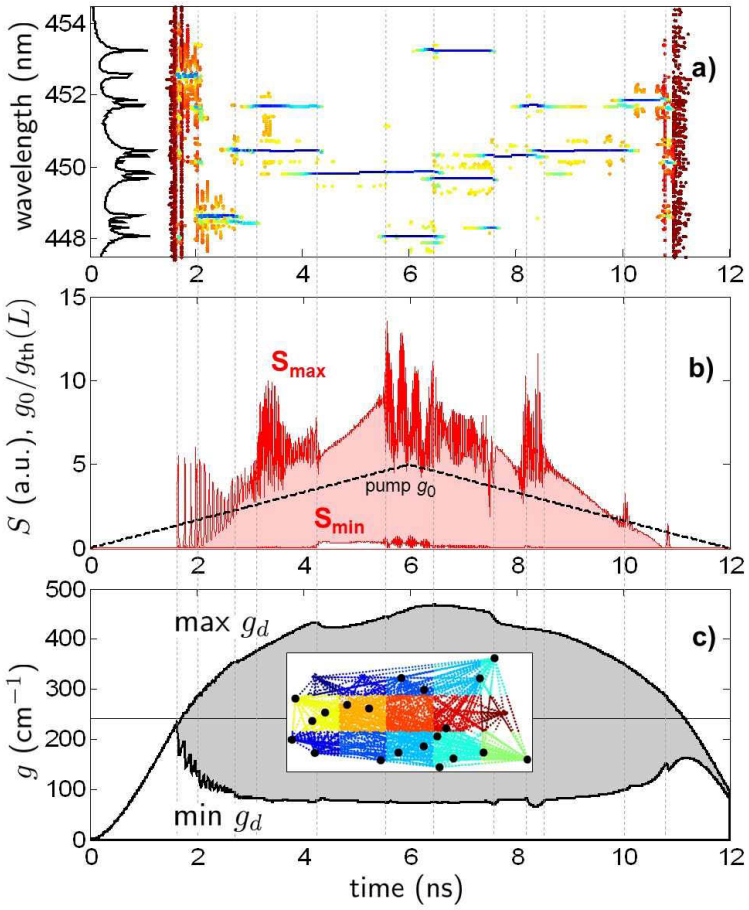

Figure 4.7: Example configuration of 20 scatterers as presented as inset in c). a) Time-integrated spectra (black line, log scale) and simulated equivalent of streak camera image plotted with colour coded intensity (logarithmic, high = blue, red = 40 dB less, peaks lower than 44 dB are not shown). The spectra are calculated in a time window of $\approx$ 77 ps. In each window the amplitudes $\mathcal{E}_{jj'}(l_{jj'}, t)$ are calculated and averaged. The spectral peaks are plotted in the centre of the window. b) Variation of the pump (g_0) as percentage of g_{th} from Eq. (4.5) (black dashed), maximum (dark red) and minimum (light red) of the intensity S. The dashed black line corresponds to the temporal profile of the pump in Fig. 4.5 b) (black) and the S_{max} corresponds to the profile of the emission (Fig. 4.5 b)(red)). c) Presents the maximum gain of any domains and its minimum, the area between is coloured grey, the solid black horizontal line marks the threshold. Inset: Top view of the excitation spot (0.4 mm * 0.2 mm) with the scatterers (dots) and the differently coloured domains, connected by the rays (dotted).

4.5 Network analysis

Now the random laser is interpreted as static fully connected, weighted network [107]. Such weighted networks have been successfully applied to road networks [108] and trade streams [109]. Its dynamics lie in the time dependent weighted links. We assume the random laser as fully connected weighted network of scatterers with active links (the rays) between them. To evaluate the dynamical change, we have to introduce appropriate weights from scatterer i to j. Subsequently, we discuss two different types of weights representing the spatio-temporal inversion distribution and the light intensity. The first, more general one, is not phase sensitive (typical for other networks), while the second one incorporates a phase sensitivity, important in the optical regime.

Amplification as a weight

A quite natural choice for weighting the links between the scatterers is the amplification along the connecting ray from scatterer i to j. It is given by

$$w_{ij}(t) = |A \cdot G(kl_{ij}) \exp(\frac{1}{2} \int_{ij} g(z,t)dz)| \tag{4.8}$$

and reaches 1 if the scattering losses are equal to the amplification. This can be interpreted as reaching the pair threshold, at which the lasing process could be sustained by only this one link. Its dynamics are given by the time dependent gain evolution of every link over time. The weight contains a single scattering process by the scattering amplitude A. Since there are N(N-1) of these links, if N is the scatterer number, they are too many to be considered individually. So we introduce a network quantifier like presented in [110, 111, 107, 112]. We can now define such a network quantifier adapted for laser physics. One possibility is to investigate the feedback of closed loops. We define

$$f_i^{(n)} = \sum_{i_2 \ldots i_n}{}' w_{ii_2} w_{i_2 i_3} \ldots w_{i_n i} \tag{4.9}$$

as sum over all n-loops starting and ending at the scatterer i. The prime symbolizes that no node index occurs twice. If the maximum of f for $n = 2$ is above 1 at all times, it would imply, that the system is equal to a pair scatterer system and only the most distant scatterers hold the lasing process. If it is below 1, another feedback from a higher n-loop is needed to reach the threshold condition. The sum incorporates no interference effects, hereby giving the maximum possible feedback of all n-loops in constructive superposition. But even in such a system, which is for sure overestimating, the two scatterer loop is not sufficient for sustaining the lasing process. The Fig. 4.8 shows the maximum of this quantifier for $n = 2$ and $n = 3$, corresponding to the node strength and cluster coefficient. Since the 2-loop feedback is only slightly below 1 adding the 3-loop feedback is enough to reach the threshold at any given time. To gain more information, we are plotting the maximum feedback for a single loop. It shows, whether

the lasing is mainly carried on a few links in the system. The maximum amplification on such a single loop is calculated by

$$G_{nloop} = max' w_{i_1 i_2} w_{i_2 i_3} ... w_{i_n i_1} \tag{4.10}$$

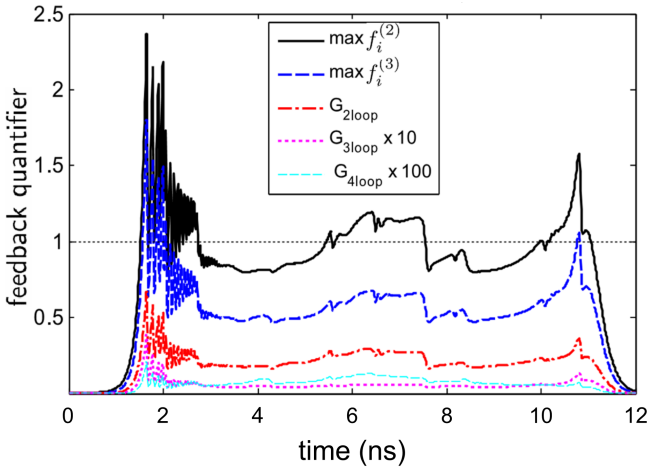

Figure 4.8: Temporal evolution of the maximum f for n loops (n=2 (black, n=3 (blue))). It represents the sum of feedback magnitude on all n-loops. G_{nloop} is the maximum feedback of all n-loops (n=2 (red, dashed-dotted), n=3 (magenta, dotted), n=4 (cyan, dashed)). The quantifier reaches threshold at 1 (dotted line).

Since the maximum feedback from a single loop is only about a fourth of the threshold value, a coherent feedback of at least 4 is necessary to reach the lasing process. For higher n the feedback drops dramatically, but the number of loops is also increasing. So by adding this high number of loops up, it could overcome the small value of a single loop. But in this case the sum of all loops are coherently adding to the feedback. This is unreasonable, since some of the loops will be out of phase and cancel each other out.

The optical intensity as a weight

Addressing this problem we defined a new weight not depending on the amplification, but on the intensity of a ray. Of course, this intensity S is connected to amplification, but it is also connected to the intensity at the scatterer, the ray starts from. Since this is given by the complex scattering amplitudes, this weight becomes sensitive to the optical phase. This is an important difference to networks outside the optical regime, where interference effects are scarce. So we define our time dependent weight as

$$w_{ij}(t) = \frac{S_{ij}(t)}{\max S_{ij}(t)} \qquad \text{with} \qquad S_{ij}(t) = \langle |\mathcal{E}_{ij}(t) G(kl_{ij})|^2 \rangle \tag{4.11}$$

The bracket $\langle ... \rangle$ symbolizes the averaging over 50 ps in time to suppress fast oscillations due to mode beating, which is the same order of the streak camera resolution in the used sweep range, and $\mathcal{E}_{ij}(t)$ is the amplitude at the end of a ray. We introduce a new quantifier corresponding to the node strength in network theory as

$$s_i = \sum_{j \neq i} w_{ij}. \tag{4.12}$$

The quantifier can reach a maximum value of N-1, if all weights are the same. So it gives a direct number of the links involved in the lasing process. Fig. 4.9 shows the node strength for the configuration investigated before. If the node strength reaches unity, a single link is holding the lasing process and if it reaches its maximum value, all weights are equally distributed. The node strength is time dependent and shows a clear threshold behaviour. Below the laser threshold the spontaneous emission causes a pretty equal distribution of intensity on the different links resulting in a high node strength, which is drastically reduced, when the lasing process starts. It does not reach its theoretical maximum because the scatterers are not equally distributed. At about half the time to the threshold the node strength maximizes, due to the gain increasing the intensities on the rays competing with geometrical reduction of a circular scattered wave.

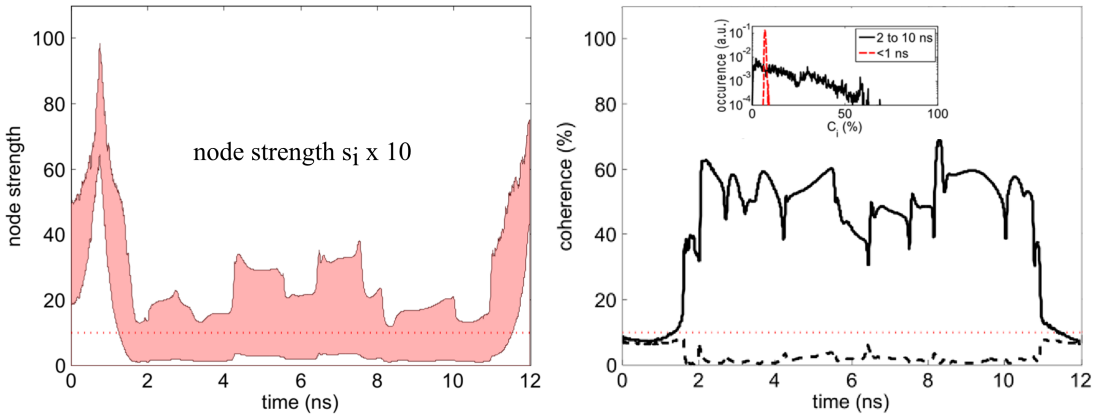

Figure 4.9: Variation of the weighted network quantifiers s_i and C_i using intensity as weight. Left: Node strength s_i x 10 as a function of time, between its maximum values, the upper line, and minimum values, the lower line (filled in red). Right: Coherence C_i in %, the maximum is given by the solid line, the minimum dashed. The inset presents the coherence distribution before threshold (red) and during the lasing process (black).

For the investigation of intensities interfering at a node, we also define a direct measure for the coherence of the node.

$$C_i(t) = \left\langle \left(\frac{|\sum_j \mathcal{E}_{ij}(t) G(kl_{ij})|}{\sum_j |\mathcal{E}_{ij}(t) G(kl_{ij})|} \right)^2 \right\rangle \tag{4.13}$$

This quantifier we call the coherence of scattering at node i. It reaches from 0 to 1 and is a measure of the interference of the impinging light. A constructive interference is represented by high values, destructive interference by low values. It also shows an interesting time evolution with a clear threshold behaviour at least for the scatterers strongly involved in the process. In Fig. 4.9 on the right the maximum of coherence is plotted over time (solid black). Before threshold it is almost identical to the minimum coherence value of $\approx 6\%$. This is close to 100%/(N-1) = 5.3% reached by all rays impinging with random phase, but same magnitude. It can be interpreted as the background spontaneous emission. During the laser operation some scatterers reach coherence levels up to 60%. In the time period between 6 to 8 ns the maximum coherence falls, which is connected to an increase of the active links. This is also visible by a local maximum of the node strength s_i. At threshold some scatterers drop down in coherence almost to 0. These frustrated scatterers are centres of destructive interference and cancelled out.

Since these quantifiers are different for every node, they can be represented by a map of the pumped area of the sample. In Fig. 4.10 a top view of the excited area is presented for certain moments in time with the drawn links corresponding to their intensity (dark is high intensity, light grey is low intensity). The scatterers themselves are symbolized by circles of different sizes with big circles implying high coherence. The crosses show the opposite with big symbols standing for low coherence. In the first panel of Fig. 4.10 the system is below threshold and neither high nor low coherence is visible and the intensity is quite equally distributed except for very short links, which hold higher intensities for geometrical reasons. When the first mode starts emitting, the coherence of the scatterers closest to the edge increases drastically and the highest intensities are carried on long rays in parallel to the excitation stripe. In the following panel another mode starts lasing changing the coherence of the scatterers. The highest coherence is now located at a scatterer, which had barely any coherence before. In the panel 3.6 ns, which corresponds to two emitting modes, we have a few nodes with big crosses showing lower coherence than the statistical value. The almost identical configuration is presented in the panel 9 ns where the identical modes emit. In the epoch of 7 ns a lot of links carry high intensities with less coherent nodes. This is the time were the node strength was quite high, meaning that the network is strongly connected at this point. The changes in the spectrum appear because some modes reduce the gain in the domain so far, that another one takes over, reaching its amplification by depleting other domains. In general, no strong loops are visible, not even 3 scatterer loops. There is always more than one link carrying the lasing process, but their number is small compared to all links present. If we look at scatterers with destructive interference, we see rays with medium intensities impinging on them, while only low intensity is scattered back (panel 7.8 ns upper right scatterer). The connections of this scatterer are weak or even not present like in direction of the lower right scatterer. The network ignores the scatterer, because it

cannot be coherently integrated to the network. This seems similar to frustrated particle packings in condensed matter physics [113].

The model used to calculate this finding used some simplifications, like isotropic scattering, which is certainly not true for our sample. This could modify certain modes but will not influence the whole system. The effects of coherence and node strength, symbolizing the scattering into different links will not be lost. The multimode emission in the calculation is based on the domain grid and a homogeneous gain, while the actual gain could be inhomogeneously broadened and vary on domains of smaller size. This might even be the reason for the higher number of co-lasing modes in the experiment.

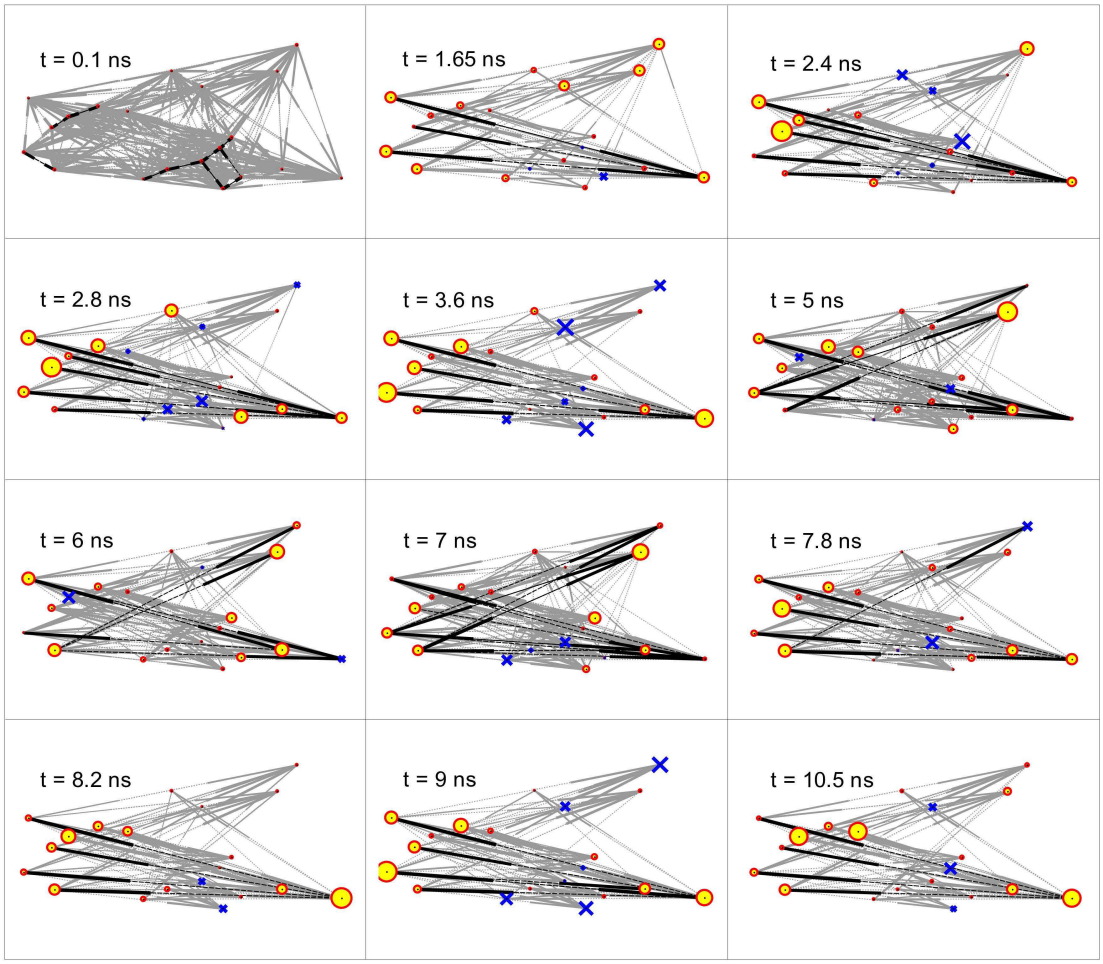

Figure 4.10: Top view of the excited area visualizing the optical network with temporal steps of the evolution during the pump pulse. High weights (dark black, above 0.5), low intensities (light grey). The circles represent coherence, their size is proportional to their coherence. Scatterers with coherence below 5% are symbolized by crosses, their size is proportional to 0.05-C_i. Weights below 0.01 are not plotted.

4.6 Conclusion

Clearly, our combination of the experiment with numerical simulation and interpretation as an optical network gives us a new view on the random lasing process. The network approach deepens the understanding of the modes dynamically evolving in quasi-steady state excitation. For a system of diluted scatterers we could show that smooth and highly reproducible excitation, like the ASE source, causes constant mode spectra from excitation to excitation pulse. From this follows, that the position of the scatterer in combination with certain gain distribution is selecting the lasing modes.

The experimental data could be reproduced qualitatively by a numerical model using approximations based on the scatterer distance and size. A network approach incorporating the specifics of the diluted system is used for the investigation of a fully connected optical network. This gives a direct understanding of the self-organization of the laser field. Especially the coherence is a quantifier graphically showing the importance of the different nodes for the lasing process. It is visualized, that only few scatterers hold the lasing process, while others are basically cancelled out by destructive interference. A generalization for random lasers of other regimes with more densely dispersed scatterers should be possible by using a more complex scattering theory [114, 115].

5 Strong coupling and lasing in organic microcavities

In this chapter a new ladder-type oligo(*p*-phenylene) is the point of interest. The molecule was chemically altered compared to *p*-quaterphenyl, a laser dye, to form a rigid backbone structure. This puts the (0,0) transition of L4P in resonance to ZnO. The absorption of L4P has a well resolved vibronic progression, which is mirrored in emission. The high quantum yield in solution (≈ 1) in combination with the possibility of vacuum deposition based fabrication and spin coating, makes L4P an excellent precursor for hybrid inorganic/organic structures. The following pages present its practical use in short cavities. Experimental data of optical gain is shown and practically applied in a vertical cavity surface emitting laser (VCSEL). This structure serves as an example of weak light matter coupling. In an even shorter cavity the coupling is increased to the polariton regime, producing a room temperature Rabi-splitting of 90 meV. Some of the results presented in the following sections can be found in ref. [116].

5.1 Introduction

Strong exciton photon coupling has been investigated for quite some time, starting with the first realization in an inorganic cavity in 1992 by Weisbuch et al. [68]. But small Rabi-splittings limited the strong coupling regime to cryogenic temperatures [117]. Organic active material with higher binding energies have the potential to create robust polaritons at higher temperatures.

The strong dipole transitions in organic dye molecules enable strong coupling up to room temperature because the coupling constant of this material can surpass the thermal broadening [118, 64]. Even the quite severe inhomogeneous broadening is only of minor concern, since coupling constants over 150 meV have been reported [119]. Coupling constants of that magnitude only need small Q-factors, so the high disorder reducing the cavity quality does not pose a big issue (see 6.5), but constant effort is put into the fabrication of high Q-factor organic microcavities to improve their emission parameters and efficiency. A detailed review on organic materials in strong coupling microcavities is given in the review articles ref. [120, 121, 122].

The first strong coupling of an organic molecule was realized by Lidzey et al. in 1998 [119] by spin coating a thin film of tetra-(2,6-t-butyl)phenol-porphyrin zinc (4TBPPZn) in a polystyrene matrix on a nine layer pair Si_3N_4/SiO_2 DBR. The cavity was completed by thermal evaporation of a silver mirror on top. The cavity reaches a Q-factor of 125. The authors reported a room temperature strong coupling measured by angular

resolved reflectivity with a splitting of 160 meV. After that, other organic molecules were investigated, like perovskites [123] and J-aggregates of cyanine dyes [64, 63]. Due to their robust nature polaritons based on organic molecules have also been investigated for nonlinear effects. Phenomena like polariton mediated energy transfer [66], Bose-Einstein condensation [124, 125, 126] and polariton lasing [127] were experimentally realized. Polariton lasing has been shown in inorganic semiconductors even sooner [128].

The step most important for application, the electrical injection, has been taken for inorganic microcavities in the strong coupling regime as well [11, 129]. For organics this was reached recently in organic light emitting diodes [12].

That is why a novel material in resonance to an inorganic semiconductor (ZnO), which has already shown room temperature polariton lasing [130, 131, 132, 133], is investigated in detail. This ladder-type oligo(*p*-phenylene) has the potential of highly efficient polariton emission in a hybrid system with ZnO. The following pages present an investigation of this single material and its use as light emitter and active material for strong coupling microcavities.

5.2 Preliminary investigations

As preliminary investigation we fabricate Fabry-Perót cavities with L4P-SP2 as an active material. The idea was to use a fabrication technique adjusted for the conditions necessary to create microcavities of high quality with an organic active material. For this task we had to adjust the evaporation parameters for dielectric mirrors for low temperature to keep the organic molecule stable. When the molecule is embedded in a polymer matrix, low temperature secures the mechanical stability of the polymer layer. To create the active layer we chose to spin coat the molecule in a polymer matrix, because of the easily controllable thickness and absorption, as well as small material consumption. Since the molecule was synthesized specially for research purposes at the chemistry institute of Humboldt-University, supply was limited and thermal evaporation of thicker layers would increase the material lost to the chamber walls.

Before creating cavity structures the active molecule was investigated in detail. Room temperature absorption and emission was characterized and is presented in Fig. 5.1. The spectral position, strength of the resonances as well as stability are very important for the cavity design. This was done on polymer/L4P-SP2 films, to see if the matrix environment would influence the optical parameters. Some general information about this molecule was already given in 2.1.2.

Since regular quaterphenyl is used as a laser dye, it made sense to investigate if the chemical alteration would effect the lasing capabilities. A modal gain measurement was used to experimentally determine its amplification in a leaky waveguide structure. This was measured by the so called stripe length method [43] using a low repetition rate nitrogen laser as excitation source 3.2. The nitrogen laser was chosen because of its high density along with its short wavelength (337.1 nm), which is over 60 nm shifted to the emission wavelength. This places it outside the stopband of the dielectric cavity mirror, making an efficient pumping for the completed samples possible. Fig. 5.2 a) shows a

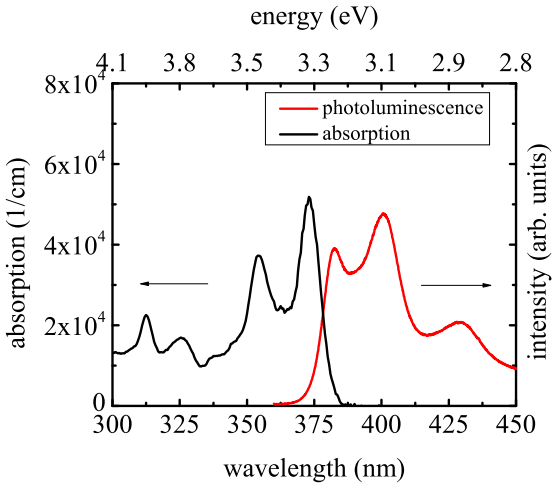

Figure 5.1: Absorption and emission spectra of L4P-SP2 in a polystyrene layer. The PL spectra was measured with a nitrogen laser excitation. The maxima in absorption are slightly red shifted to the pure L4P. The (0,0) emission transition is lowered due to reabsorption, which is much weaker in diluted solutions.

schematic drawing of the experimental technique.

The nitrogen laser is focused onto an adjustable slit by a combination of a spherical and a cylindrical lens. This slit is then imaged on the sample surface creating a stripe with homogeneous illumination and sharp edges. The emission is then collected from the edge of the sample. The idea of this experiment is to measure the intensity as a function of excitation length. If an inversion is created by the pump source the amplified spontaneous emission should increase exponentially with the excitation length. For bulk semiconductors this technique is described in detail in the works of [43, 44] and for ZnO based MQWs produced in our group in [45].

For the gain measurement a layer of polystyrene with 20 wt% of the active molecule is spin coated on a quartz substrate. The concentration of the polymer in solution is chosen to reach approximately a thickness of 120 nm to support the modes in a leaky waveguide created. Since polystyrene has a slightly higher refractive index than quartz, the emitted light is guided in the polymer slab. In such a sample configuration the gain measured is not the material gain but the so called modal gain, which is lowered by the only partial overlap of the mode and gain medium 2.12. Because of the very small refractive index contrast, the penetration into the substrate is quite severe.

The leaky waveguide method has the advantage of lower material consumption and can be produced with the same spin coating technique later used in the cavity structure. The reduced modal gain lowers the demands put on the dimensions of the stripe by increasing the saturation length. For high gain bulk material the used stripe has to be in the order of a few microns to avoid saturation. Such small dimensions can only be realized with

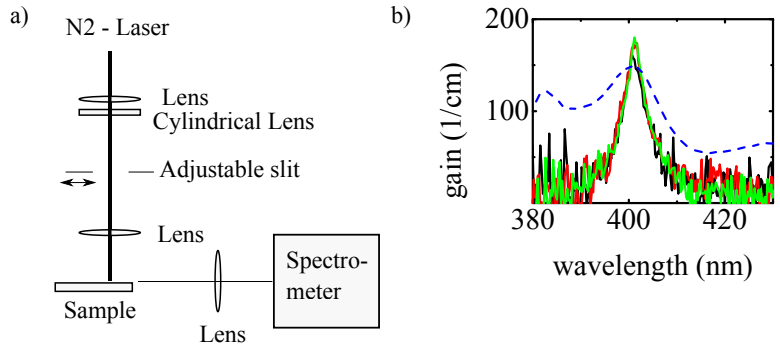

Figure 5.2: a) Measuring geometry and b) consistent gain spectra for three different stripe lengths, pumped with an energy density of 16 mJcm^{-2}. The blue dashed line represents a low density excitation PL spectrum.

high quality imaging systems. Furthermore, this opens up the possibility to measure the intensity of one length and its double. The gain can be calculated analytically in this case, which only works if the double length is not yet in saturation [43, 45].

$$I(E,d) = I_0(E,0)\frac{e^{g(E)d}-1}{g} \tag{5.1}$$

$$\frac{I(E,d)}{I(E,2d)} = \frac{e^{g(E)d}-1}{e^{g(E)2d}-1} = \frac{1}{e^{g(E)d}+1} \tag{5.2}$$

$$\Rightarrow g(E) = \frac{1}{d}ln(\frac{I(E,2d)}{I(E,d)}-1) \tag{5.3}$$

In Fig 5.2 b) the modal gain spectra are plotted for three different stripe lengths and their double lengths giving consistent data of g = (170 ± 10) cm^{-1}. The excitation density was 16 mJcm^{-2}, so even higher gain values should be possible for higher pump densities. The measurement also showed that the stability of L4P was sufficient for such pump energies. The blue dashed line represents a low density excitation PL spectrum. Like expected for molecules with well resolved vibronic transitions the gain maximizes at the spectral position of the (0,1) emission line. The inversion is easier to create at this transition because of the unoccupied ground level 1, making it a four level system.

This experiment clearly showed that a Fabry-Perót laser should be possible by using a high reflective mirror with a high enough thickness of the gain material.

But first we want to focus on the shortest possible cavity. This reduces the gain length but enhances the light matter coupling.

5.3 Coupling

To reach the strong coupling regime in a microcavity, we used the design presented in Fig. 5.3. The cavity was designed as short as possible ($\lambda/2$). The active layer is a polymer (Zeonex 480) with a refractive index of ≈ 1.6. This active layer is surrounded by quarter wavelength layers ZrO_x with higher refractive index producing a phase jump. For the opposite refractive index profile a cavity at least twice as long is necessary.

To create the sample a microscopy slide made from soda-lime glass is used as a substrate. The substrate is build into the evaporation chamber and clamped to a rotating holder. The evaporation is performed from a single crucible position (crucible revolver) creating a cone of material onto the sample surface. The substrate heating is set to 100 °C to ensure a stable temperature during evaporation. Starting with ZrO_x and followed by SiO_x we evaporated 6.5 layer pairs ending again with ZrO_x to create the bottom DBR. Both materials were evaporated at a rate of 0.2 nm per second.

After the bottom mirror is finished the vacuum is broken and the sample put on a spin coater (see 3.1.3). At this point the quality of the lower DBR is checked in the UV-VIS spectrometer, its transmission is shown in Fig. 5.3 (black). The sample is coated by solution of the cyclo-olifin polymer (Zeonex 480) containing 20 wt% of L4P-SP2 and rotated at 30 rps for at least one minute to create a layer of ≈ 120 nm. The polymer used has a high glass transition temperature of 140 °C to ensure mechanical stability during the evaporation of the top DBR. Using polystyrene would create layers with higher flatness because of its better solubility, but the top mirror fractures after the evaporation process of the top DBR due to mechanical stress (see Fig. 5.3). After the spin coating the sample is dried one day and build back into the evaporation chamber. The top DBR is evaporated identically to the lower one. The sample heating is then switched of and cooled to room temperature during the night to avoid stress in the sample layers. The next day the sample is taken out of the vacuum chamber and is characterized with optical transmission and reflection.

For a first characterization transmission is measured in the UV-VIS spectrometer, presented in Fig. 5.3 (red). Then the sample is put on the goniometer table for angular resolved measurements. The experimental setup is presented in Fig. 3.10. For illumination a xenon arc lamp (Müller Elektronik, 75 Watt) is used. A 50 cm focus length spectrograph with a 300 l/mm grating and CCD (Princeton Instrument EM1600pro) for detection is used for the spectral analyses. A colour glass filter (BG12) is used to reduce red stray light (see Fig. 3.11) and shape the lamp spectrum to reach more counts in the range of interest. Fig. 5.4 presents the room temperature angular reflection of such a sample in steps of 1° (left). A zoom of three different angles of incidence presents the pure cavity resonance at 12°, the coupling to the first vibronic transition at 46° and the coupling to both vibronic transition simultaneously at 63°.

After determining the minima of the reflection spectra, they are fitted by the three coupled oscillator model.

The system is modelled by an eigenvalue equation:

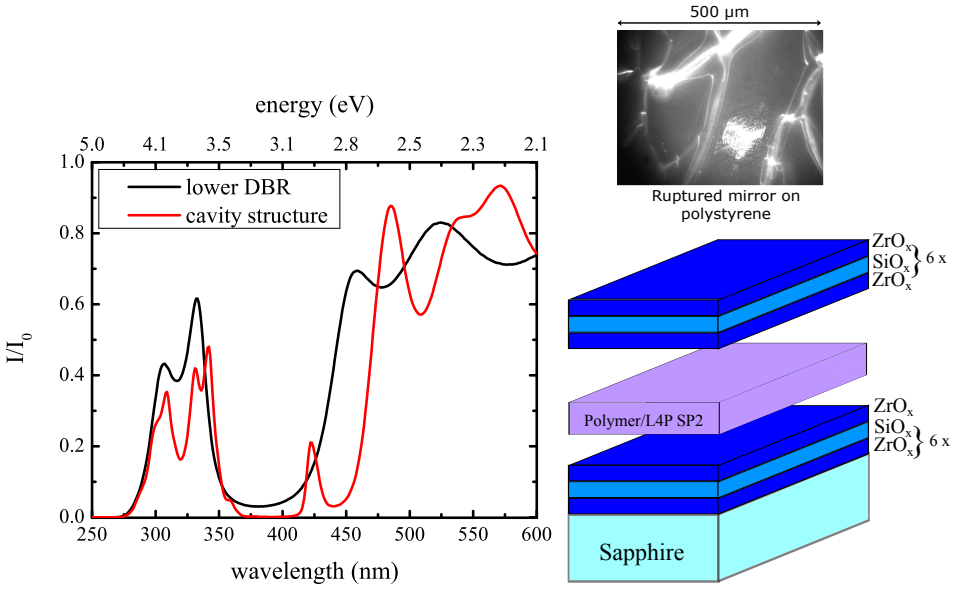

Figure 5.3: Left: Transmission spectra of the lower DBR (Black) and the finished cavity structure (red). Upper right: Microscopy image of a ruptured DBR on polystyrene. Lower right: Schematic drawing of the cavity. The SiO_x/ZrO_x layer are $\lambda/4$ optical thickness and the polymer layer $\lambda/2$.

$$\begin{pmatrix} E_1 & 0 & V_1 \\ 0 & E_2 & V_2 \\ V_1 & V_2 & \hbar\omega_c(\theta) \end{pmatrix} \cdot \begin{pmatrix} v_1 \\ v_2 \\ v_3 \end{pmatrix}_i (\theta) = E_i(\theta) \begin{pmatrix} v_1 \\ v_2 \\ v_3 \end{pmatrix}_i (\theta). \tag{5.4}$$

Hereby, E_1 and E_2 represent two material resonances, in the presented case the (0,0) and (0,1) vibronic transition in the absorption of the molecule, which is 3.32 eV and 3.51 eV, respectively. $\hbar\omega_c(\theta)$ is the angle dependent energy of the cavity resonance ($\hbar$ reduced Plank constant, ω frequency, θ angle of incidence). v_1, v_2, v_3 are the entries of the eigenvectors and i numerates the i-th branch. The cavity dispersion is modelled by the following equation:

$$\omega_c(\theta) = \frac{\omega(0)}{\sqrt{1 - \frac{\sin^2(\theta)}{n_{\text{eff}}^2}}} \tag{5.5}$$

It represents the well known blue shift of the cavity resonance over the increase of the angle of incidence (see 2.3.3).

Fitting the eigenvalues of the coupling matrix to the experimental data is used to determine the coupling constants, the effective refractive index and the energetic position of the cavity resonance for $\theta = 0$. In Fig. 5.5 the symbols are the experimentally

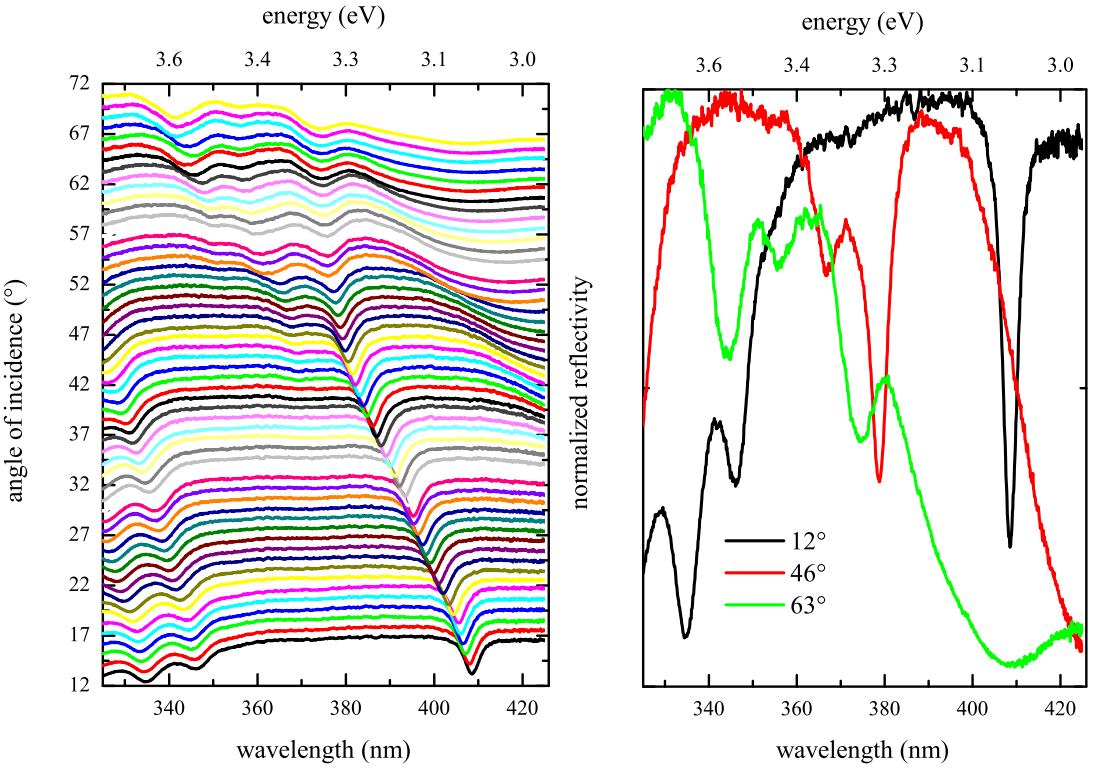

Figure 5.4: Experimental reflection spectra. Left: Angular resolved reflectivity in steps of 1°. Right: Three distinct spectra visualizing the different stages of detuning and how the coupling evolves at 12°, 46° and 63° angle of incidence.

determined minima and the solid lines are the eigenvalues of Eq. (5.4) with $V_{00} = 47$ meV, $V_{01} = 46$ meV, $\hbar\omega_c(0) = 3.02$ eV and $n_{eff} = 1.66$. The effective refractive index is slightly enhanced due to the molecule and mirror layers.

The square of the entries of the eigenvectors are interpreted as weights. Only the middle branch is presented in Fig. 5.5 since the other two show only the mixing with one other resonance and are therefore of minor interest.

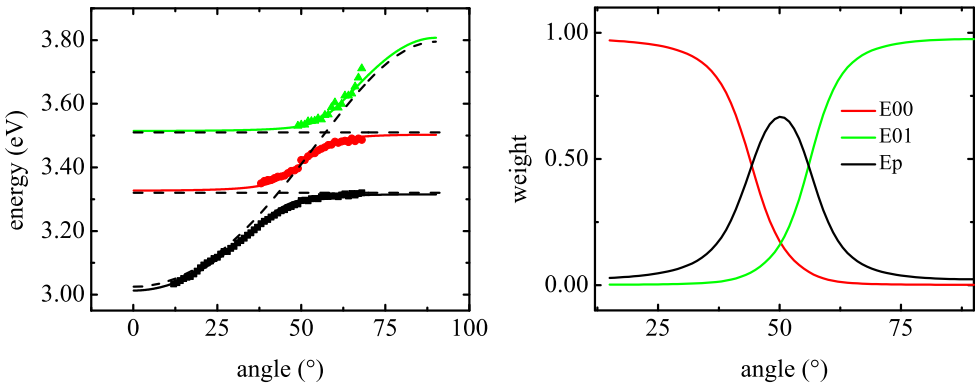

Figure 5.5: Left: Angular dependent eigenvalues of the coupling matrix (solid lines), energetic position of the material resonances and the uncoupled cavity dispersion (dashed lines). Symbols are the experimentally determined reflection minima. Right: Mixing coefficients or weight of the middle branch.

The coupling constants of ≈ 45 meV are strong enough to reach the strong coupling regime at room temperature, visible by a clear splitting of 90 meV in the reflectivity spectra. The cavity resonance for 0° is fitted to be $E_p(\theta) = 3.02$ eV. Further increase of the coupling strength should be possible by using a higher concentration or an evaporated layer of our active molecules.

A second sample, reaching also the strong coupling regime with slightly lower coupling, was also investigated by angular resolved PL measurements with low and high excitation density. The decision to use a second sample for this investigation was made because damage under high density was likely. The sample was placed on the goniometer table and the excitation was focussed on the sample surface by a 75 mm lens. The adjustable fibre was used for detection. For comparison two different types of excitation sources were used. For low density a quasi-continuous-wave 80 MHz system was used (3.2.3) and for high density the nitrogen laser was applied.

The frequency tripled Nd:IVO_4 provides a wavelength of 355 nm (3.5 eV) and pulses of ≈ 12 ps. The excitation spot is around 3 mm in size. It was not stronger focused to use the same excitation arrangement for the nitrogen laser, which reached a 1 mm excitation spot. The different size of the excitation spots is caused by the high divergence of the fibre coupled ps-laser. After the sample was measured at low density excitation the experiment was repeated with high density excitation at a repetition rate of 5 Hz with the nitrogen laser (377 nm, 0.5 ns) to investigate if changes in the relaxation appear

for different excitation densities. The integration time had to be increased for high density measurements since the mean pump power was quite low (below 1 mW). Fig. 5.6 presents the angular resolved spectra which shows a clear TE-TM splitting of the cavity resonance for angles above 45° for both excitations. The emission follows the lower polariton branch. The other branches are not visible, which is common for high absorbing materials. The low density excitation was performed with 50 $mWcm^{-2}$. For the nitrogen laser the excitation fluence was set to ≈ 10 $mJcm^{-2}$. This value is not very precise since the beam profile is not uniform and was only focussed by a 75 mm lens, but it is save to say that the peak power density exceeds a few $MWcm^{-2}$.

In comparison, the angular resolved PL with the Nd:IVO_4 laser as excitation, has its maximum emission intensity at small angles. In contrast, the emission generated by the nitrogen laser has its main maximum at the (0,1) vibrational states of the molecule at about 42° (see Fig. 5.6). High pump densities should help the relaxation process due to scattering processes of polaritons and vibrations, but here the maximum emission corresponds to gain maximum of the molecule. Contrary to the ps-laser, the nitrogen laser can achieve an inversion in L4P-SP2 molecules which characteristically emits from the (0,1) transition of the emission spectrum. This is the identical energy range, where the maximum in the polariton branch is located. If an inversion is created by the high density excitation, the relaxation of the molecule over the (0,1) emission transition is shortened and because of its strong shift to the energy levels involved in the coupling, they can not be reabsorbed.

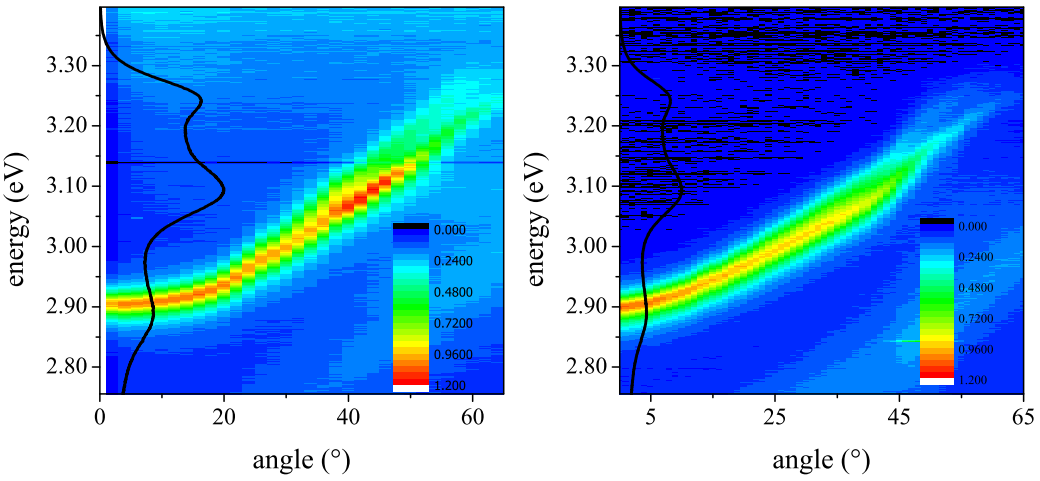

Figure 5.6: Left: Sample is excited by the nitrogen laser at 5 Hz repetition and 337.1 nm with a pulse length of 500 ps. The PL was measured in steps of 2.5°. Right: Excitation at 355 nm with 12 ps-pulses with repetition of 80 MHz measured in steps of 1°. Solid black line represents the Pl spectrum of the molecule on a reference sample under low density excitation.

Even with a pump intensity as high as 20 mJcm^{-2} no photon lasing could be achieved in the presented sample. The overlap of gain spectrum and the cavity mode is very poor, so this comes as no surprise.

High Q-factor cavities

To create a sample with higher Q-factor, the active layer was thermally evaporated. It was produced by a different technique, using a similar design. Instead of the spin cast polymer film the active layer was evaporated thermally. The sample was made by evaporation of 13.5 layer pairs of ZrO_x/SiO_x and 43% thinner SiO_x layer as part of the cavity. After that the sample was taken from the chamber and transported to the organic molecular beam deposition system, where Moritz Eyer, a colleague of mine, evaporated an organic layer with a thickness of 50 nm of L4P-SP3 (another spiro derivative of L4P). Than the sample was build back to the electron beam evaporator and the cavity layers were finished by another cavity layer (25% thinner) and 11.5 layer pairs. The cavity produced reached a Q-factor of $\approx$ 1800. The quality of the sample was certainly good enough but the misplaced cavity mode made it impossible to reach the material resonances. Because of the small sample size of 10 mm x 10 mm a cavity tuning over a thickness gradient was not possible. It serves here as a proof of concept for the fabrication technique.

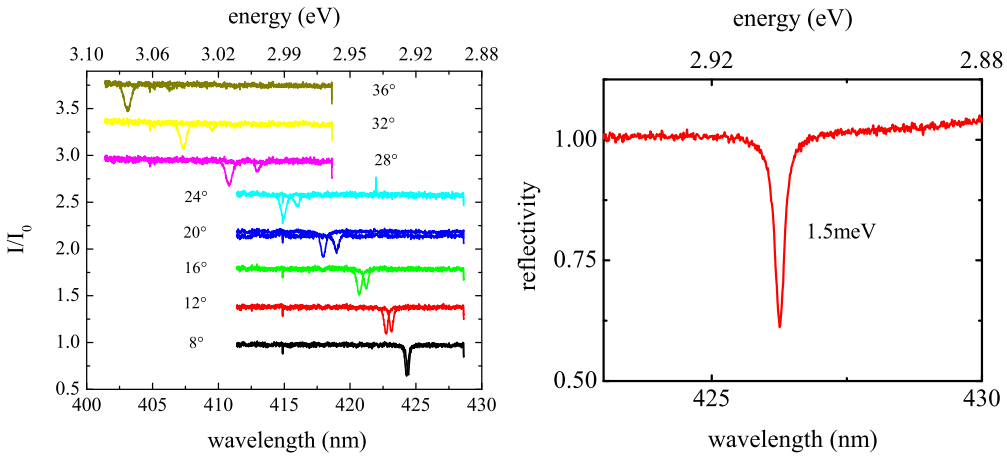

Figure 5.7: Left: High resolution reflectivities measurement of a cavity with an evaporated layer of molecules in steps of 4 degrees. Due to the sharp resonance the TE-TM splitting is already visible at low angles. In TM polarization (peak at lower wavelength) the dispersion is stronger than for TE. Right: Zoom of one reflection spectrum.

The measurement, presented in Fig. 5.7, was performed in the setup for angular resolved reflectivity with a tungsten light source and 1800 lines/mm grating.

The change to use a polymer matrix was mainly done to reduce the amount of material used for one sample since the supply of L4P was limited due to the lack of commercial

availability. Furthermore, it was clear that lower mirror reflectivities would still reach the strong coupling regime.

For studies of the optical emission this approach is more promising due to the lower losses.

5.4 Lasing

The strong coupling samples did not have high enough amplification to overcome the losses on the gain length of only 120 nm. The material needed for evaporation of thick layers (a few 100 nm) for a short cavity VCSEL (Vertical Cavity Surface Emitting Laser) was quite high. We decided for a different approach to create a Fabry-Pérot laser with longer gain length and higher Q-factor of the cavity.

To create the cavity mirror with optically flat surfaces of high reflectivity two microscopy slides are evaporated with 10.5 layer pairs, simultaneously. This creates two identical highly reflective mirrors (99.8%). After the characterization of the mirror to prove the right position of the stopband a solution of polystyrene in toluene with a concentration of 90 gL^{-1} and 20 wt% of L4P-SP2 is mixed. Drops of the solution are scattered over the whole mirror. After the solvent is evaporated the second mirror is placed on top and the whole specimen is clamped together. With the clamps, the whole structure is placed on a heating plate set to 120 °C melting the polystyrene while the clamps press the mirrors together. After a few seconds Newton rings appear on the sample showing that the cavity reached a cavity length in the range of a few micrometers. When the interferences stop to change, the heating is stopped and the cavity hardens in this position. The sample was then characterized by transmission experiments outside the stopband to measure the cavity length presented in Fig. 5.8. Inside the stopband the modes are not visible due to the absorption of the molecule.

The sample was then excited by the nitrogen laser and pump intensity dependent emission was measured to find the laser threshold for this structure. The result is presented in Fig. 5.9. The threshold is 0.8 mJ/cm^2 not counting the reflection losses of the upper mirror, which reduces the pump by about 50%.

By overlapping the cavity mode with the gain profile of the molecule, lasing of a single mode could be achieved. In this working range the divergence is $\pm$ 7° as presented in Fig 5.9 and fitted by a Gaussian profile. The sample was measured on the goniometer table by adjusting the fibre in steps of one degree. With proper adjustment of molecule concentration and cavity length much lower threshold values should be possible. Even with this simple fabrication technique a single mode VCSEL based on L4P-SP2 in a polymer matrix is realized. In all measurements presented with high excitation density the repetition was set to 5 Hz to create an equilibrium of the triplet state occupation. A spike of the emission after blocking the excitation lowering to a constant value makes an involvement of the triplet state likely.

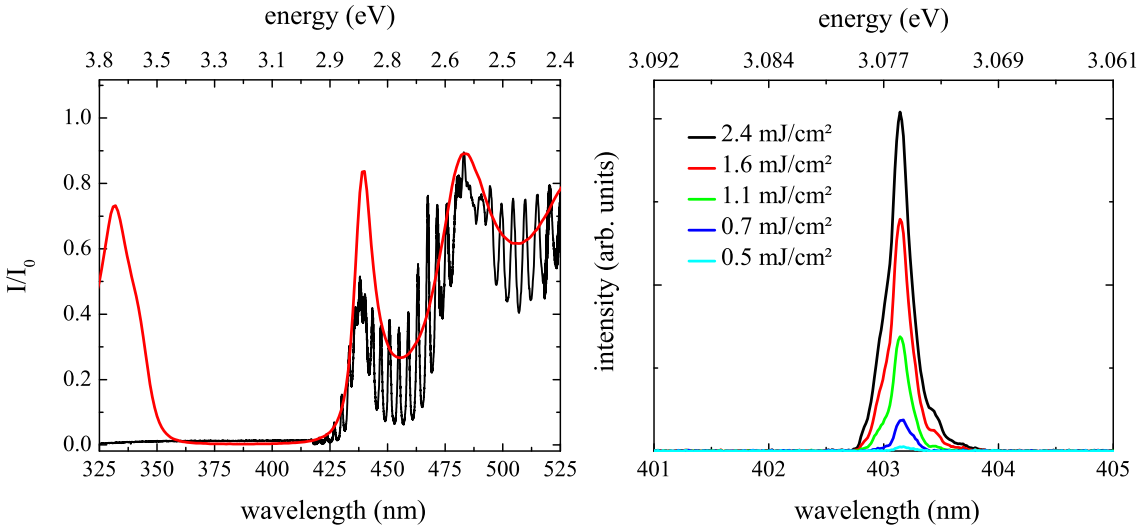

Figure 5.8: Characterization of the VCSEL. Left: Transmission of single cavity mirror (red) and the whole structure (black). Outside the stopband the Fabry-Pérot modes are clearly visible. Right: Emission spectra at different pump fluences, showing the emission from a single cavity mode.

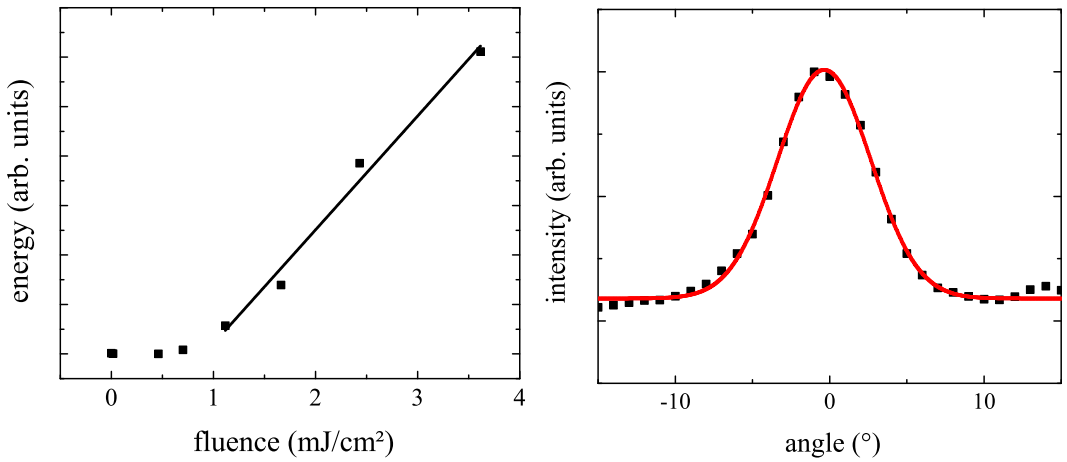

Figure 5.9: Left: Threshold measurement presenting the emitted energy over the pump fluence used to excite the sample. Right: Divergence of the emission, measured in steps of 1° with the fibre at the goniometer table also used in angular resolved reflection experiments.

5.5 Conclusion

The newly synthesized ladder-quaterphenyl is a well suited precursor for microcavities reaching the strong coupling regime. Even with the lowered oscillator strength using a spin coated layer with only 20 wt% of our active molecule a room temperature polariton formation is possible. We observed a splitting of ≈ 90 meV to both vibronic transitions. The coupling can be increased further by using ultra high vacuum deposition producing layers of higher oscillator density.

After its chemical alteration the molecule is still a highly efficient light emitter with high possible gain. This is supported by the threshold of 0.4 mJcm^{-2} (corrected for the top mirror reflection) comparable to other organic VCSEL structures in [134]. The cavities are not yet optimized and a reduction of the losses will most likely result in a further lowering of the threshold.

The presented features are in resonance to ZnO and therefore an important precursor for the realization of inorganic/organic hybrid microcavities reaching the strong coupling regime. The rigid backbone structure pushes its main transition in resonance to ZnO while simultaneously lowering the broadening of the transitions. All these characteristics make the combination of ZnO and L4P a promising material system for engineering the polariton formation by combining the strong coupling of the Frenkel exciton with efficient scattering of the inorganic Wannier-Mott exciton.

6 Strong coupling in ZnO and oligo(p-phenylene) hybrid structures

In the previous chapter was shown that two vibrational resonances of a molecule could be coupled to a resonator resonance. It is known that bulk ZnO [135, 136, 137, 138] and ZnO QWs can be coupled to the resonator mode of a microcavity as well [139, 140]. The combination of both materials could reach interesting characteristics in the strong coupling regime. The theoretical approach to such a system was already published by Agranovich et al. in 1997 [13] and further theoretically studied by Abassi et al. [141]. But practical realization is difficult since inorganic materials rely on good crystal quality to reach high oscillator strength, while inorganic materials bring disorder to the system. Since the growth of high quality QW structures is dependent on well adjusted growth conditions, like high temperatures in the vacuum chamber and an oxygen plasma source, most organics will not survive these necessary conditions of crystal growth. The oxygen plasma would chemically alter the molecules and the high temperatures will damage the molecules. The temperatures used for thermal evaporation of the molecules in OMBD systems range from 80 °C to 100 °C. Even if the chemical structure of the molecule will survive, a desorption from the surface will most probably destroy the prepared layer. The organic layer needs low temperatures to avoid damage and desorption. Even incorporated in a polymer matrix the temperatures are limited for basically the same range and the crystal structure is lost. The following sections present a new approach combining an MBE grown ZnMgO based DBR and MQW active layer with an organic layer on top. The cavity is then closed by an amorphous dielectric mirror. By combining the different materials in a two step process a hybrid inorganic/organic microcavity is created to reach the strong coupling regime. This gives the opportunity to tailor the efficient phonon assisted relaxation of the inorganic Wannier-Mott exciton and the dipole transitions of the organic molecules.

6.1 Introduction

Since the theoretical proposal a lot of effort was put in the experimental realization of such structures to create a polariton mediated energy transfer between the inorganic and organic polariton states. The first realization of such a hybrid system was achieved by Wenus et al. [15] by using ZnTTP (zinc tetraphenylporphyrin) and a perovskite $(C_6H_5C_2H_4NH_3)_2PbBr_4$ (phenylethylamine tetrabromoplumbate). They spin coated two identical SiN/SiO_2 (12 pairs) DBRs with both active materials in a poly(methyl-methacrylate) (PMMA) matrix. The sample was created by putting the two mirrors

together creating a variable air gap to tune the cavity resonance. Position resolved reflectivity and PL revealed the strong coupling of both materials and cavity photons with a Rabi-splitting of 100 meV for both resonances. Both active materials had shown to reach the strong coupling regime before [142, 143], therefore they were a good choice to reach the strong coupling regime in a hybrid cavity.

Another combination of crystalline inorganic semiconductor structure with an organic semiconductor was realized by Holmes et al. [14] with the combination of InGaP QWs and tetraphenylporphyrin (TPP). A further example realized the strong coupling regime using inorganic bulk ZnO and the organic perovskite 5-methyl-2-furanmethanamonium lead bromide (MFMPB) in a microcavity created from an AlN/AlGaN based lower DBR and Al metal upper mirror [144]. Due to the large detuning of the material resonance to the coupling constants, both materials reach high mixing with the photon but are only weakly mixed with each other, shown in helium temperature reflectivity measurements. A similar cavity design using NTCDA and ZnO nanoparticles reached the strong coupling at room temperature [145]. The NTCDA molecule shows two absorption resonances, with the (0,1) transition in resonance with ZnO. By direct comparison of microcavities containing the pure active materials they show an increase of coupling strength for the hybrid cavity to the pure NTCDA cavity. Hereby the pure NDCDA cavity has already three angular dependent branches created by the cavity resonance and (0,0) and (0,1) transition of the molecule. By adding the spin-coated ZnO nanoparticle layer the splitting is increased, but no anticrossing of the ZnO resonance and the (0,1) transition of the molecule is observed.

The following sections present the experimental realization of MBE grown ZnO QWs with a specially synthesized organic molecule, the ladder-quaterphenyl (L4P) already discussed before. Both for ZnO QWs [146] and a spiro derivative of the active molecule [116] strong coupling has been shown in our group, making L4P and ZnO a promising material combination.

6.2 Preliminary measurement and cavity design

Since the cavity using our active molecule in a polymer matrix already reached the strong coupling regime at room temperature and measurements on reference layers showed that the absorption of the spin coated layer was strong enough to match at least six QWs (even at moderate concentration $\approx 25\%$), a change of fabrication technique was unnecessary. The sample needed a longer cavity to support multiple quantum wells, which should match the absorption strength of the organic layer. The inorganic quantum well has to be positioned near the maximum field in the cavity or the influence on the coupling would be weak. The field minimum in the DBR layers of a mirror is always located at the transition from lower to higher refractive index starting form the centre of the cavity. Looking at our ZnMgO based DBR the refractive index is lower for higher Mg concentration (see Fig. 3.7). Keeping typical values for the Mg content of the barrier material results in a high refractive index of the main cavity material, placing a high field amplitude at the edge of the cavity. Since typical QWs (barriers) have a thickness

of 3 nm (8 nm) and six of them will already add up to 66 nm, it will be difficult to place them in a field maximum of a short cavity. That means a longer cavity would be more practical for an efficient positioning of the QWs. So we combined a $\lambda/2$ layer of L4P in the polymer matrix with $5\lambda/2$ space for the quantum wells. This combined with two $\lambda/4$ mirror layers creates a length of 2λ. Since the coupling constant $V \sim 1/\sqrt{L}$, a reduction of the splitting to ≈ 45 meV is expected if the concentration is held constant. This puts the coupling strength near the range we expect for six QW incorporated in a cavity of the same length.

Further we should think about the reflectivities needed in the experiment. Very high numbers of mirror pairs increase the risk of cracks, inhomogeneities and scattering losses. For this an investigation of the splitting depending on the mirror reflectivity will help. One possibility is to calculate this by using the TMM and program certain designs with a different number of layer pairs and evaluate them, but this is quite time consuming.

A second approach in the approximation of high reflectivities is presented in an article by Savona et al. [60]. In this work a model is introduced for the different types of splittings in the strong coupling microcavity. The following equations present the splitting into lower and upper polariton branch for the absorption Ω_A, the transmission Ω_T, the reflection Ω_R and the Rabi-splitting Ω. These are valid in the approximation of high reflectivities for normal angle of incidence.

$$\Omega_T = 2\sqrt{\sqrt{V^4 + 2V^2\gamma(\gamma+\gamma_c)} - \gamma^2} \tag{6.1}$$

$$\Omega_R = 2\sqrt{\sqrt{V^4(1+\frac{2\gamma}{\gamma_c})^2 + 2V^2\gamma^2(1+\frac{\gamma}{\gamma_c})} - 2V^2\frac{\gamma}{\gamma_c} - \gamma^2} \tag{6.2}$$

$$\Omega_A = 2\sqrt{V^2 - \frac{1}{2}(\gamma^2+\gamma_c^2)} \tag{6.3}$$

$$\Omega_{PL} = \sqrt{2\Omega\sqrt{\Omega^2 + 4((\gamma+\gamma_c)/2)^2} - \Omega^2 - 4((\gamma+\gamma_c)/2)^2} \tag{6.4}$$

$$\Omega = 2\sqrt{|V|^2 - \frac{1}{4}(\gamma_c-\gamma)^2} \tag{6.5}$$

From these equations it is possible to calculate different splittings depending on material parameters like damping and the Q-factor of the cavity. Here Ω is the splitting, V the coupling constant, γ the material resonance (homogeneous) damping and γ_c the cavity damping.

A dielectric cavity with ZnO as active material serves as an example. Coupling constants reported in literature differ strongly with typical values between 20 to 60 meV (higher values have been reported, but are not expected in our MQW sample). This should make it possible to reach the strong coupling regime even with lower Q-factor cavities. We adapt the formula for the cavity damping

$$\gamma_c = \frac{1-\sqrt{R}}{\sqrt{R}} c/(n_{\text{cav}} L_{\text{eff}}) \tag{6.6}$$

$$\text{with} \quad n_{\text{cav}} \approx 2 \quad \text{and} \quad L_{\text{eff}} = L_{\text{cav}} + L_{\text{DBR}} \tag{6.7}$$

$$L_{\text{DBR}} = \left(\frac{n_{ZrO} n_{SiO}}{n_{\text{cav}}(n_{ZrO} - n_{SiO})} + \frac{n_{ZnMgOhigh} n_{ZnMgOlow}}{n_{\text{cav}}(n_{ZnMgOhigh} - n_{ZnMgOlow})}\right)\lambda/4 \tag{6.8}$$

Setting these values to $n_{ZrO} = 1.95$, $n_{SiO} = 1.56$, $n_{ZnMgOhigh} = 2.30$, $n_{ZnMgOlow} = 2.02$ and $n_{\text{cav}} = 2.4$ gives a penetration length of $L_{\text{DBR}} = 916$ nm. The cavity length is $L_{\text{cav}} = 720$ nm for a 2λ cavity. Putting this into equation (6.5) the Rabi-splitting can be plotted as a function of the mirror reflectivity. The coupling strength is set to V = 0.025 eV, which is a realistic value for our quantum wells in a microcavity [146]. For a first approximation the exciton damping is set to zero to get the maximum splitting. As expected the Rabi-splitting starts to evolve at low reflectivity of 0.3 and reaches close to its maximum at ≈ 0.6. On the right side the absorption splitting for four different material damping is presented. Here the energetic splitting of the branches is strongly reduced if the damping of the resonances is too high. From experiments on purely monolithic ZnO based cavity a homogeneous broadening of about 10 meV - 20 meV is expected [146]. The homogeneous broadening of the molecular layer is not known since it is always strongly inhomogeneously broadened. The typical homogeneous linewidth of an organic molecule is far lower and the inhomogeneous linewidth dominates the spectral response [147]. The inhomogeneous broadening does not influence the splitting, but will mask it by overlapping so a measurement in angular resolved reflectivity is no longer possible [148].

The graphs in Fig. 6.1 make clear that at least for a proof of concept the mirror reflectivity in a system with high coupling constant does not need high reflectivity cavities with too high Q-factors. For an efficient practical use like for a polariton laser the Q-factor should be higher to reduce the losses and increase the interaction probability.

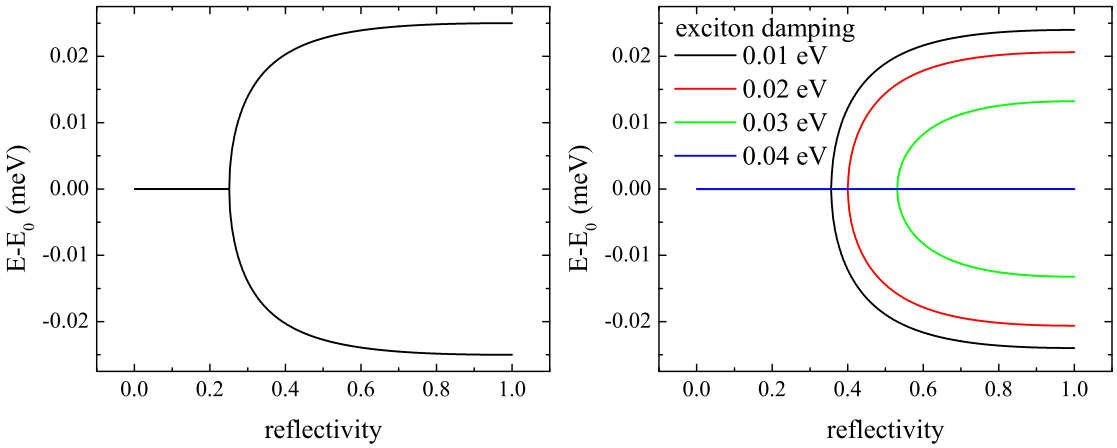

Figure 6.1: Left: Dependence of the Rabi-splitting of the upper and lower polariton-branch as a function of reflectivity. Right: Dependency of the absorption splitting on reflectivity for different exciton damping.

6.3 The ZnO/L4P hybrid microcavity

Our cavity design rests on high quality ZnO/ZnMgO QWs created by MBE growth. To achieve this goal we use an epitactically grown ZnMgO-based DBR, maintaining the crystal structure. This gives us the possibility of growing high quality QWs on top. After this the inorganic cavity part is finished, further steps in sample fabrication are no longer crystalline layers. Since the unfinished sample has to be removed from vacuum anyway, we have the possibility to characterize absorption strength of the ZnO QWs in the sample between the steps. The concentration of the active molecule can be chosen accordingly.

After this first characterization an organic/polymer layer is spin coated on the lower DBR and QWs. The solution is precisely tuned to the oscillator strength of the QWs by adapting the molecule concentration in the layer. The upper DBR is than created by electron beam evaporation. Five layers of SiO_x and ZrO_x are grown on top finishing the cavity with the DBR.

We focussed on proving that strong coupling of the active materials is possible in an angular resolved reflectivity measurement. Therefore, low reflectivity mirrors are used in the cavity design. The number of mirror pairs for the DBRs were chosen high enough to reach the strong coupling but simultaneously give easy optical access for the angular resolved reflectivity measurements. Since we know the coupling strength expected from the former investigation for the pure microcavities [146], the necessary reflectivity to observe the splitting could be calculated (see 6.1). The cavity design is sketched in Fig. 6.2 and will easily overcome these conditions.

After the MBE growth is finished the sample was cooled (77 K) and measured in transmission in a bath cryostat to validate the position of the DBR stopband and the absorption of the ZnO QWs. During this measurement the position dependence of the

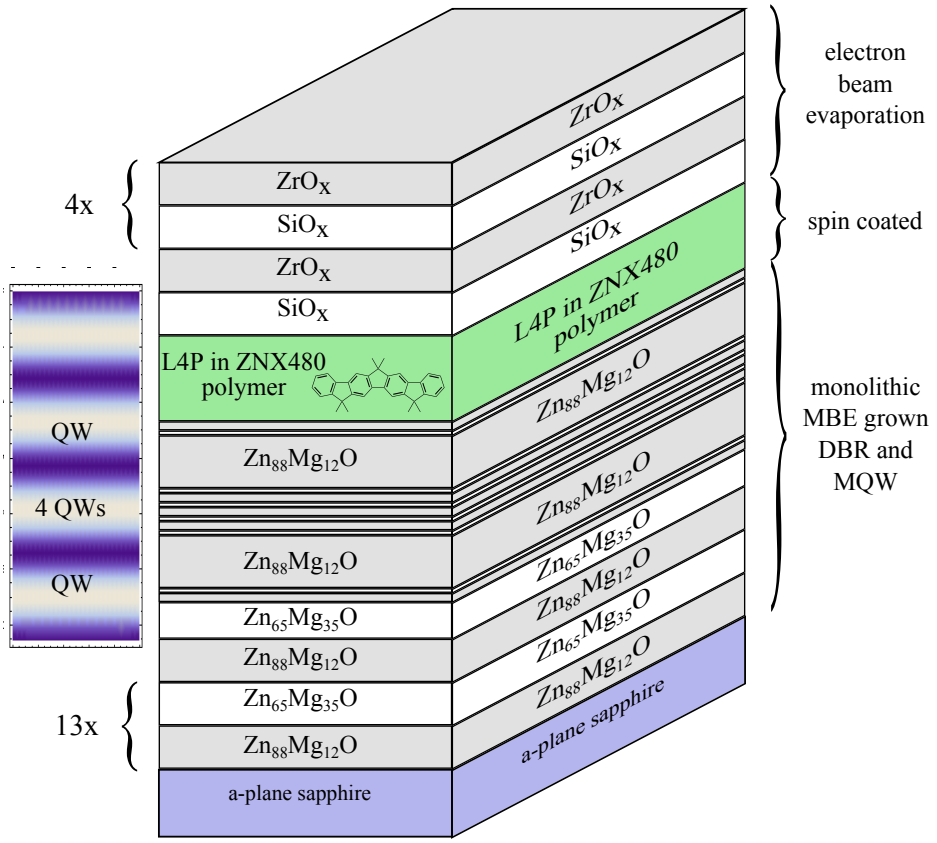

Figure 6.2: Hybrid microcavity design containing six QWs and L4P in polymer matrix as active material. The thicknesses presented are proportional to optical thicknesses. Left of the cavity is a schematic density plot visualizing the intensity distribution inside the cavity (white high intensity, blue low intensity).

DBR and the angular dependent transmission of the structure could be investigated. This is quite interesting since the DBR is grown quite close to the material resonance of ZnMgO meaning its refractive index is strongly energy dependent. That means quite strong reflectivity changes are expected while tuning the sample by changing the angle of incidence.

Fig. 6.4 presents an angular resolved transmission at 77 K of the inorganic part of the structure in steps of 2.5°. The transmission spectra shows two angular independent features, the QW absorption at 366 nm (3.39 eV) and absorption edge of $Zn_{0.88}Mg_{0.12}O$ layers of the barrier and DBR at ≈ 355 nm (3.49 eV). The stopband is centred at 375 nm (3.31 eV). During the blue shift of the stopband the reflectivity increases slightly from 0.7 to over 0.9. This will also slightly differ at even lower temperatures. Above 385 nm (3.2 eV) the angular dependent Bragg modes of the mirror are observed.

After this measurement the sample was spin coated with a solution with a concentration of 17 g/L Zeonex 480 in toluene containing 27 wt% of the L4P molecule. This polymer is the same as in the pure organic cavity because a dielectric DBR is evaporated on top making a high glass transition temperature of 140 °C necessary. The concentration of L4P was chosen to match the oscillator strength of the quantum wells as close as possible. To achieve this absorption data, a typical QW produced in our group, was fitted by a Lorentz oscillator model with three oscillators. The following equation describes its dielectric function:

$$\epsilon(\omega) = \epsilon_{BGR} + \frac{f_1}{\omega_1^2 - \omega^2 + \beta_1 i\omega} + \frac{f_2}{\omega_2^2 - \omega^2 + \beta_2 i\omega} + \frac{f_3}{\omega_3^2 - \omega^2 + \beta_3 i\omega} \tag{6.9}$$

For non-magnetic material the complex refractive index is given by $\tilde{n} = n + i\kappa = \mathrm{Re}[\sqrt{\epsilon(\omega)}] + i\,\mathrm{Im}[\sqrt{\epsilon(\omega)}]$. The imaginary part κ also known as the extinction coefficient reaches a maximum of 1.22 for ZnO and 0.21 for the L4P/polymer layer, giving a ratio of 5.8. This is no coincidence since the thicknesses of the active layers have a ratio of 120/(6*3.5) = 5.7. This adjustment was reached by choosing the concentration of L4P in the polymer and should result in almost equal mixing coefficients.

After a drying time of a few hours the SiO_x/ZrO_x based DBR is evaporated on top. Another sapphire substrate is placed next to the sample to create a reference for the dielectric mirror. During evaporation the sample is heated to ≈ 100 °C providing a good compromise of mirror quality and the mechanical stability of the polymer layer.

The upper DBR, measured on the reference sample, reaches a maximum reflectivity of 0.9 positioned at 400 nm (3.10 eV) (circles) as presented in Fig. 6.4. The transmission of the inorganic part at 77 K is presented for comparison (rectangles) and the reflectivity at 4 K for the finished structure (triangles). It has a clear cavity resonance at 380 nm (3.26 eV). The whole sample is then put in a transmission cryostat and measured in angular reflectivity at helium temperature (setup see Fig. 3.10). The excitation was a tungsten light source. Fig. 6.3 presents the angular reflectivity in TE polarization in steps of 5 degrees vertically shifted for clarity (measured in steps of 1°). The energetic position of the reflection minima are determined and used as input for coupled oscillator

	ZnO QWs	L4P/polymer layer
ϵ_{BGR}	4.84	2.56
ω_1	3.40 eV	3.35 eV
f_1	0.350 eV^{-2}	0.0758 eV^{-2}
β_1	0.0175 eV	0.046 eV
ω_2	3.46 eV	3.53 eV
f_2	0.284 eV^{-2}	0.119 eV^{-2}
β_2	0.0418 eV	0.139 eV
ω_3	3.49 eV	0 eV
f_3	0.667 eV^{-2}	0 eV^{-2}
β_3	0.07 eV	0 eV

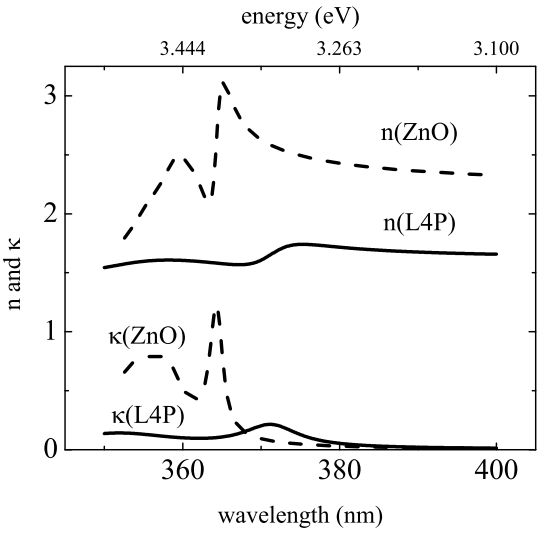

Figure 6.3: Tab.: Fitting values for the dielectric function of ZnO and L4P. Right: The plotted imaginary (κ) and real part (n) of the complex refractive index n + iκ for ZnO (dashed) and L4P (full line).

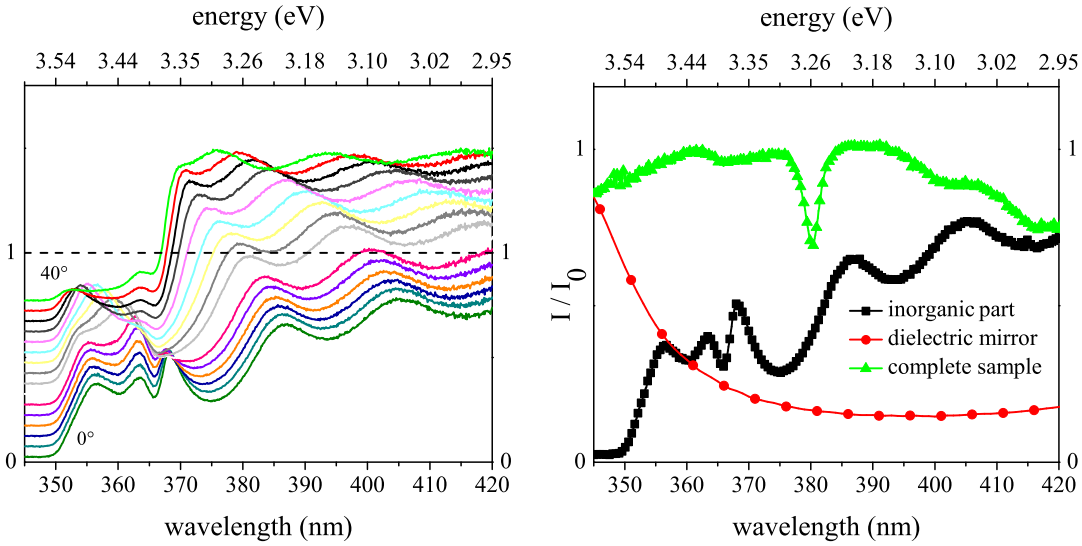

Figure 6.4: Left: Angular resolved transmission at steps of 2.5° of the inorganic structure, shifted for clarity by steps 0.05. The dashed line represent a transmission of 1 corresponding to the first spectrum ($\theta = 0°$). Right: Transmission of inorganic part (77 K), transmission of the dielectric mirror (reference) at room temperature and the reflectivity of the whole structure at an angle of 10° at 5 K.

model following Eq. (6.10). The cavity dispersion is modelled by $E_0/\sqrt{(1-\sin^2\theta/n_{\text{eff}}^2)}$ as before.

$$\begin{pmatrix} E_{\text{ZnO}} & 0 & V_{\text{ZnO}} \\ 0 & E_{\text{L4P}} & V_{\text{L4P}} \\ V_{\text{ZnO}} & V_{\text{L4P}} & \hbar\omega_c(\theta) \end{pmatrix} \cdot \begin{pmatrix} v_1 \\ v_2 \\ v_3 \end{pmatrix}_i (\theta) = E_i(\theta) \begin{pmatrix} v_1 \\ v_2 \\ v_3 \end{pmatrix}_i (\theta) \tag{6.10}$$

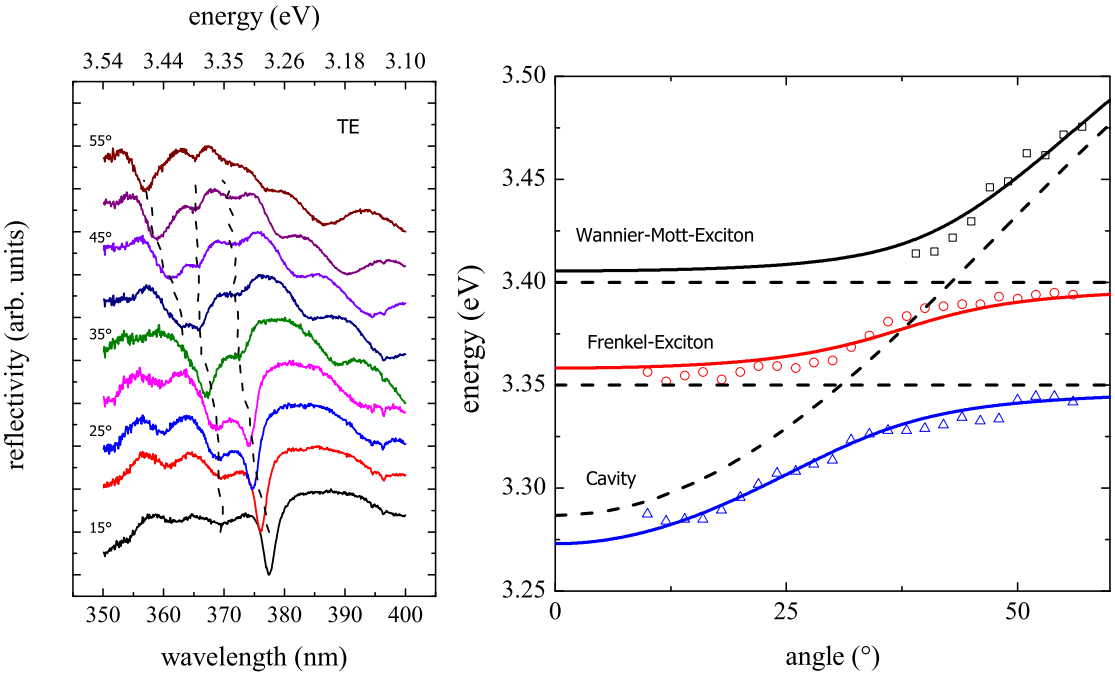

Figure 6.5: Left: Angular resolved reflectivity in five degree steps at T = 5 K. The dashed lines represent the minima of the spectra in steps of 1 degree. Right: The symbols are the experimental values of minima. The solid lines are the eigenvalues of the model for V_{L4P} = 27 meV, V_{ZnO} = 24 meV, $\hbar\omega_c(0)$ = 3.29 eV and n_{eff} = 2.66. The dashed lines represent the undisturbed exciton resonances and the cavity dispersion.

Hereby, V_{L4P}, V_{ZnO}, $\hbar\omega_c(0)$ and n_{eff} are fitting parameters and the material resonances are set to E_{L4P} = 3.35 eV for the molecule and E_{ZnO} = 3.4 eV for ZnO. The model is in good agreement with coupling constants of $\approx$ 25 meV $\pm$ 5 meV resulting in a splitting of $\approx$ 50 meV. This is about double the absorption splitting achieved for a monolithic cavity, which is expected to increase due to the higher number of QWs maintaining the same cavity length [146]. For the spiro derivative of L4P in an organic cavity the coupling constants are about two times higher, most likely because of the smaller mode volume in the λ-half cavity with a similar oscillator strength [116].

Same as before we interpret the square of the entries of the eigenvector as the weight, also known as mixing fraction or Hopfield coefficient, and calculate them for every branch i. We see from Fig. 6.6 that for the middle branch at small angle of incidence the Frenkel excitonic character dominates. For increasing angle, the eigenvalues reduce this character to favour the character of the photon and Wannier-Mott exciton to equal parts. This makes the polariton states, a linear combination of all three resonances with equal weight, a hybrid of photon, Wannier-Mott- and Frenkel exciton. For the middle branch the resonance changes its character from low angles, where it is mostly of the Frenkel type to a mixed state of all three resonances at 35°. At high angles the Wannier-Mott exciton dominates the character. The other two branches show only clear mixing with the neighbour resonance.

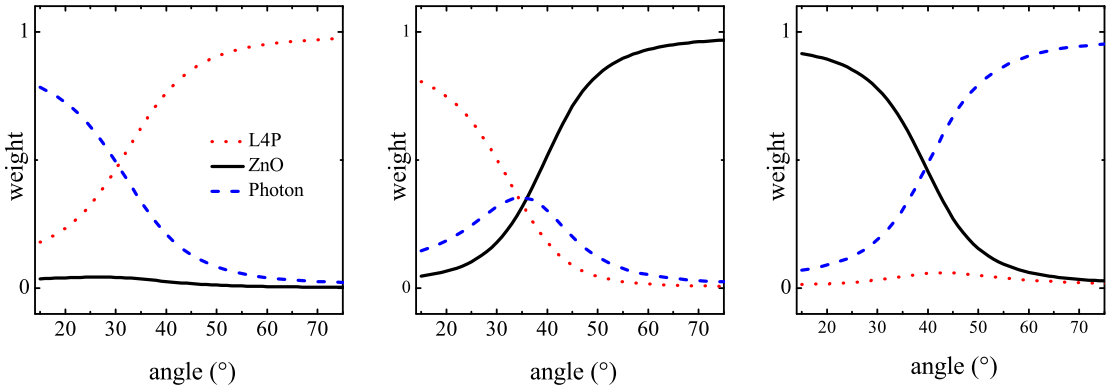

Figure 6.6: Mixing fraction for the lower (left), middle (centre) and upper (right) branch.

6.4 Conclusion

To summarize, we created a hybrid inorganic/organic microcavity based on ZnO QWs and L4P. Low temperature reflectivity gives evidence for strong coupling by a splitting of ≈ 50 meV. The experimental data was fitted by an oscillator model with three resonance and two coupling constants of ≈ 25 meV. The square of the angular dependent entries of the eigenvectors reveals an equal mixing of 0.3 for the middle branch. This is an important precursor for efficient polariton relaxation.

Even with a splitting close to the LO (longitudinal optical) phonon energy of ZnO a slight increase to really match the splitting to 72 meV could enhance the relaxation in emission. This is not only beneficial for the relaxation, but also the needed increase to reach room temperature polariton formation. Room temperature strong coupling with a splitting of about a phonon energy has been observed in bulk ZnO [149]. For the organic cavity the strong coupling was also observed in cavities with lower concentration resulting in a splitting of about ≈ 75 meV still sufficient for room temperature operation. Since the fabrication technique will eventually allow to reach high Q-factor cavities the system is promising to reach polariton lasing operating without cooling.

7 Summary and Outlook

This thesis focusses on the light matter coupling of semiconductor structures. In the weak coupling regime the emission of a random laser and an organic VCSEL are investigated. On the strong light matter coupling side, microcavities based on an organic and hybrid inorganic/organic structures are the point of interest.

While precise fabrication of optoelectronic devices has increased their efficiency, beam characteristics and reliability, the necessary control of resonator geometry limits further price reduction. This makes the investigation of scattering feedback an important field in semiconductor laser research. Especially the dynamical properties of random laser are important for their further use in optical communication. That is the reason we investigate the dynamics of a random laser based on ZnO/ZnCdO multi quantum wells. The feedback is realized by air holes, which develop under certain growth conditions.

Hereby, the dynamical features of the ZnCdO based random laser are the point of interest under quasi-stationary condition. Using highly reproducible excitation pulses in combination with a constant scattering configuration shows an emission with constant mode features. The experimental results are qualitatively reproduced by a numerical model and interpreted with methods of network theory. Based on the scatterer distance, the network is fully connected, with weighted links between the scatterers. Introducing dynamical network measures adapted for an optical network, creates an interesting visual representation of the self-organization in the random laser. The network analysis brings a new method of characterization to the random laser field, which could help engineering the laser emission to special levels of coherence, temporal shape and emission angle. In combination with pump pulse shaping in time and space the random laser could reach its breakthrough because of its cheap production and versatility.

First experiments of adjusting the random laser emission by shaping the excitation has been presented in experiment and theory [150]. This technique in combination with a network analysis on real scatterer configurations could make a control of emission wavelength and its temporal behaviour possible. A spacial light modulator imaged on the sample could make selective pumping of the different domains possible. Further investigation is needed to predict how strong this effect can influence the emission and if the system can be held stable over the complete excitation time. This is only one example why further research in this field is needed. The specialized applications in medicine and speckle free imaging are promising examples that optoelectronic devices based on random lasers will be applied. An understanding and control of the dynamical processes can only be beneficial for these and other practical uses.

While feedback of scatterers lowers production costs, well defined cavity feedback will improve energy consumption and will remain a common choice for semiconductor light emitters. Next to classical inorganic semiconductors, organic molecules can be used

to realize a wide variety of lasers. Their high optical gain makes even strongly diluted systems possible but their electrical excitation is still a challenge. By chemical alteration the energy range of the emission can be shifted as well as optical parameters like damping can be adjusted making these systems very versatile.

This work presents such a chemically altered molecule. Quaterphenyl is altered to a ladder-type structure shifting its transition in resonance to ZnO and reducing the spectral width of the vibrational progressions. To characterize this newly created molecule, measurements of absorption, luminescence are performed and the gain distribution is investigated. By using this information a quite simple laser based on L4P is fabricated. The VCSEL structure is created by using two identical mirrors with an active layer of L4P-SP2 in a polymer matrix. Even with a quite long cavity single mode operation could be realized with a threshold of 0.4 $\mathrm{mJcm^{-2}}$ (corrected for mirror reflection). The emission has a small divergence of $\pm$ 7°. The chemical alteration from a *para*-phenylene to ladder-type molecule has shifted the gain and localized it on the (0,1) transition but it is still well suited for laser operation at a wavelength around 402 nm. The investigated structure was not optimized in reflectivity and dye concentration, making a further reduction in laser threshold possible.

Besides this practical use, the purpose of L4P lies in its combination to ZnO. Our goal here is the strong light matter interaction created in a microcavity. Because of big differences of organic and inorganic semiconductors in structure and binding energy, there are some obstacles to overcome in fabrication. This made a proof of concept study for the pure molecule necessary.

This was achieved in a short $\lambda/2$ cavity with a spin coated layer of L4P-Sp2 in a polymer surrounded by two dielectric DBRs made from SiO_2/ZrO_2. Room temperature reflectivity showed two anticrossings with a separation of about 90 meV reaching a coupling with the (0,0) and (0,1) vibrational transition. This makes L4P a ideal candidate for strong coupling hybrid structures with ZnO.

ZnO has been shown to reach stable cavity polaritons due to its high binding energy more than 2 times larger than the thermal energy. By using not bulk ZnO but a number of ZnO quantum wells in the hybrid cavity we can adjust the oscillator strength of the ZnO. Furthermore a slight tuning with the quantum well thickness is possible. The oscillator strength can be adjusted for the organic material by choosing the right concentration and layer thickness. This resulted in a cavity design incorporating six quantum wells and a $\lambda/2$ layer of L4P with a concentration of 27 wt% to reach equal mixing of all three resonances at a certain angle.

The inorganic/organic system is experimentally investigated by low temperature reflectivity revealing a splitting of $\approx$ 50 meV between all resonances. The energetic positions of the materials with an adjustable oscillator strength in the polymer layer gave the possibility to achieve an equal mixing of all three resonances observed in angular resolved reflectivity. This reveals the equal mixing of inorganic, organic and cavity resonance for the middle branch.

For the investigation of the emission a slightly increased coupling should be beneficial to match the energy of LO phonon of ZnO (72 meV). To still reach the equal mixing

of the three branches a slightly red shifted spiro derivative of L4P could be used. Also other chemical alteration could be used for fine tuning the organic resonance with only minor changes in oscillator strength.

Further investigation of such structures should focus on the emission. This will require a higher reflectivity of both DBRs, which should be reached by a higher number of layer pairs with no technical difficulties. A broader stopband width of the ZnMgO mirror would be beneficial, since the DBRs presented have not yet achieved that limit. While a cavity using a spin coated layer of L4P in a polymer can reach higher Q-factor than presented here, they will not reach the quality factor of the test cavities using an evaporated layer of the molecule. Using the combination of these materials in a high quality microcavity makes reaching polariton lasing at room temperature likely. This would open a completely new field in research of polaritons based on hybrid inorganic/organic systems. It could result in a diverse number of coherent organic light emitters excited by the inorganic semiconductor they are paired with.

Polariton lasing in purely inorganic and organic structures has been achieved with thresholds of one percent of the photon lasing. This makes these coherent light emitters more efficient than their weakly coupling counterpart and could make them an interesting alternative to the well established inorganic semiconductor laser diodes.

Even if there is still some way to go, the applications of these devices in research and technology seem closer to reach than ever.

Appendix

1 Transfer-matrix method

The TMM is an often used technique for the simulation of dielectric layer stack for DBR, etalons and microcavities. It is applicable for homogeneous layers of a constant (complex) refractive index. It is commonly implemented in software tools sold in combination with evaporator systems for mirror design. It can be used in absence of an imaginary refractive index most easily but will also work for absorbing layers. It is hardly applicable to calculate the emission of microcavities with active materials since the plan wave condition is no longer valid.

The presented representation of the TMM is adapted from ref. [151]. The plane wave hits the dielectric stack in z-direction and the electric and magnetic field components follow the equation:

$$\begin{pmatrix} E(0) \\ H(0) \end{pmatrix} = M(z) \cdot \begin{pmatrix} E(z) \\ H(z) \end{pmatrix} \tag{1}$$

Hereby M is called the characteristic matrix and given for TE-polarization with $p = n\ \cos\theta$ as

$$M(z) = \begin{pmatrix} \cos(k_0\ n\ z\ \cos\theta) & -\frac{i}{p}\sin(k_0\ n\ z\ \cos\theta) \\ -i\ p\ \sin(k_0\ n\ z\ \cos\theta) & \cos(k_0\ n\ z\ \cos\theta) \end{pmatrix} \tag{2}$$

This can by done for a high number or material layers like for a DBR mirror just by multiplying the matrices for each layer.

$$\begin{pmatrix} E(0) \\ H(0) \end{pmatrix} = M_1(z_1)M_2(z_2)M_3(z_3)...M_n(z_n) \begin{pmatrix} E(z_n) \\ H(z_n) \end{pmatrix} = M \begin{pmatrix} E(z_n) \\ H(z_n) \end{pmatrix} \tag{3}$$

The reflection and transmission coefficient can be calculated, if we assume a semiinfinite medium on each side of the dielectric stack, with the refractive indices n_1 and n_l incorporated in $p_1 = n_1 \cos\theta_1$ and $p_l = n_l \cos\theta_l$

$$r = \frac{(m_{11} + m_{12}p_l)p_1 - m_{21} + m_{22}p_l)}{(m_{11} + m_{12}p_l)p_1 + m_{21} + m_{22}p_l)} \tag{4}$$

$$t = \frac{2p_1}{(m_{11} + m_{12}p_l)p_1 + m_{21} + m_{22}p_l)} \tag{5}$$

This technique is presented in much more detail and for both polarizations in [151]. Even it was not used in direct comparison to the full structures, its comparison to the DBRs gives a lot of information about the refractive indices of the used layers. If the refractive indices are correct, but there are still strong differences to the TMM simulation, an investigation of surface roughness is advised.

2 Implementation of the random Laser simulation

The simulation was implemented using the program language MATLAB provided by the Mathworks corporation.

The spectral dynamics, centred around 450 nm, are calculated in time steps of dt = 48 fs = $\frac{\lambda_0^2}{2c\Delta\lambda}$ with $\Delta\lambda$ = 7 nm. From this follow spacial steps on the rays of dl = 7.2 μm. The edges of the grid were set at the final scatterer or just beyond. The field is represented by logarithmic amplitudes (ψ= ln($\mathcal{E}(z,t)$)), which are subsequently placed into a large array. They and the domain gain g_d are updated every time step.

First the field is propagated on each ray according the propagation equation (4.4)

$$\psi(z,t) = \psi(z - dl, t - dt) + 1/2[1 - \alpha i(g_d(t - dt/2) - \bar{g}) - \alpha_0]dl \tag{6}$$

The matlab operation CIRCSHIFT, which shift the array elements circularly was used to shorten the calculation time. In a second step the new values are set by

$$\psi_{ij}^{in} = ln \sum_{r'} A_{rr'}[\mathcal{E}_{r'}^{out} G(k, l') + \beta_{spont}] \tag{7}$$

These are the fields produced by instantaneous scattering and injected into a ray r. Linear interpolation is used to get an amplitude for the final scatterer between the last grid points.

This approximation introduces a numerical dispersion to the system, suppressing high frequency modes, which can be used to simulate the “real” gain dispersion.

Then the gain is updated. The time step is shifted by half the size of dt for the fields with identical stepsize. From this follows the integration of the rate equation (4.5)

$$g_d(t + dt/2) = g_d(t - dt/2) + [g_0 - g_d(t - dt/2)(1 + S_d(t))]dt/\tau_n \tag{8}$$

With the average intensity $S_d = \langle |E_s|^2 \rangle_{s \in d}$ estimated as the average over the impinging intensities at all domain scatterers.

Abbreviations

a_B	Bohr radius
ASE	amplified spontaneous emission
CB	conduction band
CCD	charge coupled device
Cd	cadmium
DBR	distributed Bragg reflector
DOS	density of states
E_g	energy band gap
FSR	free spectral range
FWHM	full width half maximum
HOMO	highest occupied molecular orbital
ITO	indium tin oxide
L4P	ladder-quater-phenyl
LUMO	lowest unoccupied molecular orbital
LO	longitudinal-optical
MBE	molecular beam epitaxy
MQW	multi quantum well
OLED	organic light emitting diode
PID-controller	proportional-integral-derivative controller
QW	quantum well
RF-plasma	radio frequency plasma
RHEED	reflection high energy electron diffraction
TMM	transfer matrix method
UV	ultra violet
VB	valence band
VCSEL	vertical cavity surface emitting laser
XeCl	xenon-chloride

List of Figures

List of Tables

Bibliography

[1] E. M. Purcell. Spontaneous emission probabilities at radio frequencies. *Phys. Rev.*, 69:681 B10, 1946.

[2] T. H. Maiman. Stimulated optical radiation in ruby. *Nature*, 187(4736):493–494, August 1960.

[3] V. M. Markushev, V. F. Zolin, and Ch. M. Briskina. Luminescence and stimulated emission of neodymium in sodium lanthanum molybdate powders. *Sov. J. Quantum Electron.*, 16:281–283, 1986.

[4] S. Kalusniak, H. J. Wünsche, and F. Henneberger. Random semiconductor lasers: Scattered versus fabry-perot feedback. *Phys. Rev. Lett.*, 106:013901, Jan 2011.

[5] B. Redding, M. A. Choma, and H. Cao. Speckle-free laser imaging using random laser illumination. *Nat Photon*, 6(6):355–359, June 2012.

[6] J. F. Donges, Y. Zou, N. Marwan, and J. Kurths. Complex networks in climate dynamics. *The European Physical Journal Special Topics*, 174(1):157–179, 2009.

[7] C. Zhou, L. Zemanová, G. Zamora, C. C. Hilgetag, and J. Kurths. Hierarchical organization unveiled by functional connectivity in complex brain networks. *Phys. Rev. Lett.*, 97:238103, Dec 2006.

[8] M. Höfner, H.-J. Wünsche, and F. Henneberger. A random laser as a dynamical network. *New Journal of Physics*, 16(3):033002, 2014.

[9] J. Kasprzak, M. Richard, S. Kundermann, A. Baas, P. Jeambrun, J. M. J. Keeling, F. M. Marchetti, M. H. Szymanska, R. Andre, J. L. Staehli, V. Savona, P. B. Littlewood, B. Deveaud, and Le Si Dang. Bose-Einstein condensation of exciton polaritons. *Nature*, 443(7110):409–414, September 2006.

[10] A. Kavokin. Exciton-polaritons in microcavities: present and future. *Applied Physics A*, 89(2):241–246, 2007.

[11] C. Schneider, A. Rahimi-Iman, N. Y. Kim, J. Fischer, I. G. Savenko, M. Amthor, M. Lermer, A. Wolf, L. Worschech, V. D. Kulakovskii, I. A. Shelykh, M. Kamp, S. Reitzenstein, A. Forchel, Y. Yamamoto, and S. Hofling. An electrically pumped polariton laser. *Nature*, 497(7449):348–352, May 2013.

[12] S. Gambino, A. Genco, G. Accorsi, O. Di Stefano, S. Savasta, S. Patané, G. Gigli, and M. Mazzeo. Ultrastrong light-matter coupling in electroluminescent organic microcavities. *Applied Materials Today*, 1(1):33 – 36, 2015.

[13] V. Agranovich, H. Benisty, and C. Weisbuch. Organic and inorganic quantum wells in a microcavity: Frenkel-Wannier-Mott excitons hybridization and energy transformation. *Solid State Communications*, 102(8):631 – 636, 1997.

[14] R. J. Holmes, S. Kéna-Cohen, V. M. Menon, and S. R. Forrest. Strong coupling and hybridization of Frenkel and Wannier-Mott excitons in an organic-inorganic optical microcavity. *Phys. Rev. B*, 74:235211, Dec 2006.

[15] J. Wenus, R. Parashkov, S. Ceccarelli, A. Brehier, J.-S. Lauret, M. S. Skolnick, E. Deleporte, and D. G. Lidzey. Hybrid organic-inorganic exciton-polaritons in a strongly coupled microcavity. *Phys. Rev. B*, 74:235212, Dec 2006.

[16] C. Klingshirn. ZnO: Material, physics and applications. *ChemPhysChem*, 8(6):782–803, 2007.

[17] L. Yu, Q. Zhu, D. Fan, and Z. Lan. Development in p-type doping of ZnO. *Journal of Wuhan University of Technology-Mater. Sci. Ed.*, 27(6):1184–1187, 2012.

[18] N. M Sbrockey and S. Ganesan. ZnO thin films by MOCVD. *III-Vs Review*, 17(7):23 – 25, 2004.

[19] Ü. Özgür, Ya. I. Alivov, C. Liu, A. Teke, M. A. Reshchikov, S. Dogan, V. Avrutin, S.-J. Cho, and H. Morkoc. A comprehensive review of ZnO materials and devices. *Journal of Applied Physics*, 98(4):041301, 2005.

[20] https://en.wikipedia.org/wiki/Wurtzite_crystal_structure wikipedia, author unknown.

[21] H. Morkoc and Ü. Özgür. *Zinc Oxide Fundamentals, Materials and Device Technology*. Wiley-VHC, 2009.

[22] S. B. Ogale, editor. *Thin Films and Heterostructures for Oxide Electronics*. Springer, 2005.

[23] D. Strauch. CdO: lattice parameters. In U. Rössler, editor, *New Data and Updates for several III-V (including mixed crystals) and II-VI Compounds*, volume 44E of *Landolt-Börnstein - Group III Condensed Matter*, pages 77–79. Springer Berlin Heidelberg, 2012.

[24] A. Janotti, D. Segev, and C. G. Van de Walle. Effects of cation d states on the structural and electronic properties of III-nitride and II-oxide wide-band-gap semiconductors. *Phys. Rev. B*, 74:045202, Jul 2006.

[25] S. Sadofiev. *Radical-source molecular beam epitaxy of ZnO-based heterostructures*. PhD thesis, Humboldt-Universität zu Berlin, 2009.

[26] S. Kalusniak, S. Sadofev, J. Puls, and F. Henneberger. ZnCdO/ZnO a new heterosystem for green-wavelength semiconductor lasing. *Laser and Photonics Reviews*, 3(3):233–242, 2009.

[27] U. Scherf. Ladder-type materials. *J. Mater. Chem.*, 9:1853–1864, 1999.

[28] U. Scherf and K. Müllen. Polyarylenes and poly(arylenevinylenes), 7. a soluble ladder polymer via bridging of functionalized poly(p-phenylene)-precursors. *Die Makromolekulare Chemie, Rapid Communications*, 12(8):489–497, 1991.

[29] B. Kobin, L. Grubert, S. Blumstengel, F. Henneberger, and S. Hecht. Vacuum-processable ladder-type oligophenylenes for organic-inorganic hybrid structures: synthesis, optical and electrochemical properties upon increasing planarization as well as thin film growth. *J. Mater. Chem.*, 22:4383–4390, 2012.

[30] B. Kobin, F. Bianchi, S. Halm, J. Leistner, S. Blumstengel, F. Henneberger, and S. Hecht. Green emission in ladder-type quarterphenyl: Beyond the fluorenone-defect. *Advanced Functional Materials*, 24(48):7717–7727, 2014.

[31] F. Bianchi, S. Sadofev, R. Schlesinger, B. Kobin, S. Hecht, N. Koch, F. Henneberger, and S. Blumstengel. Cascade energy transfer versus charge separation in ladder-type oligo(p-phenylene)/ZnO hybrid structures for light-emitting applications. *Applied Physics Letters*, 105(23):–, 2014.

[32] M. Sparenberg, A. Zykov, P. Beyer, L. Pithan, C. Weber, Y. Garmshausen, F. Carla, S. Hecht, S. Blumstengel, F. Henneberger, and S. Kowarik. Controlling the growth mode of para-sexiphenyl (6p) on ZnO by partial fluorination. *Phys. Chem. Chem. Phys.*, 16:26084–26093, 2014.

[33] D. Fritsch. *Investigation of nitride and oxide semiconductors by means of the Empirical Pseudopential Method*. Engelsdorfer Verlag, 2007.

[34] W.J. Fan, A.P. Abiyasa, S.T. Tan, S.F. Yu, X.W. Sun, J.B. Xia, Y.C. Yeo, M.F. Li, and T.C. Chong. Electronic structures of wurtzite ZnO and ZnO/MgZnO quantum well. *Journal of Crystal Growth*, 287(1):28 – 33, 2006. Proceedings of the International Conference on Materials for Advanced Technologies (ICMAT 2005) Symposium N ZnO and Related Materials Proceedings of the International Conference on Materials for Advanced Technologies (ICMAT 2005) Symposium N.

[35] C. Klingshirn. *Semiconductor Optics*. Springer, 2007.

[36] G. Czycholl. *Theoretische Festkörperphysik*. Vieweg, 2000.

[37] T. Hanada. Basic properties of ZnO, GaN, and related materials. In Takafumi Yao and Soon-Ku Hong, editors, *Oxide and Nitride Semiconductors*, volume 12 of *Advances in Materials Research*, pages 1–19. Springer Berlin Heidelberg, 2009.

[38] I.G. Hill, A. Kahn, Z.G. Soos, and Jr R.A. Pascal. Charge-separation energy in films of π-conjugated organic molecules. *Chemical Physics Letters*, 327(34):181 – 188, 2000.

[39] B. Schweitzer and H. Bässler. Excitons in conjugated polymers. *Synthetic Metals*, 109(13):1 – 6, 2000.

[40] B. E. A. Saleh and M. C. Teich. *Grundlagen der Photonik*. Wiley-VCH, 2007.

[41] X.-Q. Lv, J.-Y. Zhang, L.-Y. Ying, W.-J. Liu, X.-L. Hu, B.-P. Zhang, Z.-R. Qiu, S. Kuboya, and K. Onabe. Well-width dependence of the emission linewidth in ZnO/MgZnO quantum wells. *Nanoscale Research Letters*, 7:605, 2012.

[42] M. Schwoerer and H. C. Wolf. *Organic Molecular Solids*. Wiley-VCH, 2007.

[43] K. L. Shaklee and R. F. Leheny. Direct determination of optical gain in semiconductor crystals. *Applied Physics Letters*, 18(11):475–477, 1971.

[44] K.L. Shaklee, R.E. Nahory, and R.F. Leheny. Optical gain in semiconductors. *Journal of Luminescence*, 7(0):284 – 309, 1973.

[45] J. Cui, S. Sadofev, S. Blumstengel, J. Puls, and F. Henneberger. Optical gain and lasing of ZnO/ZnMgO multiple quantum wells: From low to room temperature. *Applied Physics Letters*, 89(5):051108, 2006.

[46] X. Wu, W. Fang, A. Yamilov, A. A. Chabanov, A. A. Asatryan, L. C. Botten, and H. Cao. Random lasing in weakly scattering systems. *Phys. Rev. A*, 74:053812, Nov 2006.

[47] Y. Yamamoto, F. Tassone, and H. Cao. *Semiconductor Cavity Quantum Electrodynamics*. Springer-Verlag Berlin Heidelberg, 2000.

[48] J. R. Devore. Refractive indices of rutile and sphalerite. *J. Opt. Soc. Am.*, 41(6):416–417, Jun 1951.

[49] L. Gao, F. Lemarchand, and M. Lequime. Reverse engineering from spectrophotometric measurements: performances and efficiency of different optimization algorithms. *Applied Physics A*, 108(4):877–889, 2012.

[50] D. L. Wood and K. Nassau. Refractive index of cubic zirconia stabilized with yttria. *Appl. Opt.*, 21(16):2978–2981, Aug 1982.

[51] D. L. Wood, K. Nassau, and T. Y. Kometani. Refractive index of Y2O3 stabilized cubic zirconia: variation with composition and wavelength. *Appl. Opt.*, 29(16):2485–2488, Jun 1990.

[52] O Medenbach, D. Dettmar, R. D. Shannon, R. X. Fischer, and W. M. Yen. Refractive index and optical dispersion of rare earth oxides using a small-prism technique. *Journal of Optics A: Pure and Applied Optics*, 3(3):174, 2001.

[53] Y. Nigara. Measurement of the optical constants of yttrium oxide. *Japanese Journal of Applied Physics*, 7(4):404, 1968.

[54] R. E. Stephens and I. H. Malitson. Index of refraction of magnesium oxide. *Journal of Research of the National Bureau of Standards*, 49:249, 1952.

[55] M. J. Dodge. *Refractive Index in Handbook of Laser Science and Technology, Volume IV, Optical Materials: Part 2,*. CRC Press, 1986.

[56] I. H. Malitson. Interspecimen comparison of the refractive index of fused silica. *J. Opt. Soc. Am.*, 55(10):1205–1208, Oct 1965.

[57] M. N. Polyanskiy. Refractive index database. Available at http://refractiveindex.info (accessed Feb. 29 2015).

[58] Umicore Thin Film Products AG. Special materials for precision optics and laser coatings. Technical report, Umicore, http://www.thinfilmproducts.umicore.com/Products/TechnicalData/show_precision_laser_e.pdf, 2011.

[59] C. J. R. Sheppard. Approximate calculation of the reflection coefficient from a stratified medium. *Pure and Applied Optics: Journal of the European Optical Society Part A*, 4(5):665, 1995.

[60] V. Savona, L.C. Andreani, P. Schwendimann, and A. Quattropani. Quantum well excitons in semiconductor microcavities: Unified treatment of weak and strong coupling regimes. *Solid State Communications*, 93(9):733 – 739, 1995.

[61] M. S. Skolnick, T. A. Fisher, and D. M. Whittaker. Strong coupling phenomena in quantum microcavity structures. *Semiconductor Science and Technology*, 13(7):645, 1998.

[62] L.C. Andreani, V. Savona, P. Schwendimann, and A. Quattropani. Polaritons in high reflectivity microcavities: semiclassical and full quantum treatment of optical properties. *Superlattices and Microstructures*, 15(4):453 – 458, 1994.

[63] P. Schouwink, H.V. Berlepsch, L. Dähne, and R.F. Mahrt. Observation of strong exciton-photon coupling in an organic microcavity. *Chemical Physics Letters*, 344(34):352 – 356, 2001.

[64] J. R. Tischler, M. S. Bradley, Q. Zhang, T. Atay, A. Nurmikko, and V. Bulović. Solid state cavity QED: Strong coupling in organic thin films. *Organic Electronics*, 8(23):94 – 113, 2007. Coupled States of Excitons, Photons, and Plasmons in Organic Structures.

[65] D. G. Lidzey, D. D. C. Bradley, M. S. Skolnick, T. Virgili, S. Walker, and D. M. Whittaker. Strong exciton-photon coupling in an organic semiconductor microcavity. *Nature*, 395(6697):53–55, September 1998.

[66] D. M. Coles, N. Somaschi, P. Michetti, C. Clark, P. G. Lagoudakis, P. G. Savvidis, and D. G. Lidzey. Polariton-mediated energy transfer between organic dyes in a strongly coupled optical microcavity. *Nat Mater*, 13(7):712–719, July 2014.

[67] D. M. Coles, R. T. Grant, D. G. Lidzey, C. Clark, and P. G. Lagoudakis. Imaging the polariton relaxation bottleneck in strongly coupled organic semiconductor microcavities. *Phys. Rev. B*, 88:121303, Sep 2013.

[68] C. Weisbuch, M. Nishioka, A. Ishikawa, and Y. Arakawa. Observation of the coupled exciton-photon mode splitting in a semiconductor quantum microcavity. *Phys. Rev. Lett.*, 69:3314–3317, Dec 1992.

[69] R. Houdré, C. Weisbuch, R. P. Stanley, U. Oesterle, P. Pellandini, and M. Ilegems. Measurement of cavity-polariton dispersion curve from angle-resolved photoluminescence experiments. *Phys. Rev. Lett.*, 73:2043–2046, Oct 1994.

[70] V. Srinivas, J. Hryniewicz, Y. J. Chen, and C. E. C. Wood. Intrinsic linewidths and radiative lifetimes of free excitons in gaas quantum wells. *Phys. Rev. B*, 46:10193–10196, Oct 1992.

[71] M. Saba, C. Ciuti, J. Bloch, V. Thierry-Mieg, R. Andre, Le Si Dang, S. Kundermann, A. Mura, G. Bongiovanni, J. L. Staehli, and B. Deveaud. High-temperature ultrafast polariton parametric amplification in semiconductor microcavities. *Nature*, 414(6865):731–735, December 2001.

[72] R. Houdré. Early stages of continuous wave experiments on cavity-polaritons. *physica status solidi (b)*, 242(11):2167–2196, 2005.

[73] Bo E. Sernelius. Reflection from a metallic surface.

[74] R. V. Ambartsumyan, N. G. Basov, P. G. Kryokov, and V. S. Letokhov. A laser with a nonresonant feedback. *IEEE Journal of Quantum Electronics*, 2:442, 1966.

[75] V. S. Letokhov. Generation of light by a scattering medium with negative resonance absorption. *Soviet Physics JETP*, 26:1442–1452, 1968.

[76] R.K. Thareja and A. Mitra. Random laser action in ZnO. *Applied Physics B*, 71(2):181–184, 2000.

[77] S. Mujumdar, M. Ricci, R. Torre, and D. S. Wiersma. Amplified extended modes in random lasers. *Phys. Rev. Lett.*, 93:053903, Jul 2004.

[78] H. Cao. Review on latest developments in random lasers with coherent feedback. *Journal of Physics A: Mathematical and General*, 38(49):10497, 2005.

[79] D. S. Wiersma. The physics and applications of random lasers. *Nat Phys*, 4(5):359–367, May 2008.

[80] O. Zaitsev and L. Deych. Recent developments in the theory of multimode random lasers. *Journal of Optics*, 12(2):024001, 2010.

[81] Y. Ling, H. Cao, A. L. Burin, M. A. Ratner, X. Liu, and R. P. H. Chang. Investigation of random lasers with resonant feedback. *Phys. Rev. A*, 64:063808, Nov 2001.

[82] S. Gottardo, S. Cavalieri, O. Yaroshchuk, and D. S. Wiersma. Quasi-two-dimensional diffusive random laser action. *Phys. Rev. Lett.*, 93:263901, Dec 2004.

[83] R. C. Polson and Z. V. Vardeny. Random lasing in human tissues. *Applied Physics Letters*, 85(7):1289–1291, 2004.

[84] I. Viola, N. Ghofraniha, A. Zacheo, V. Arima, C. Conti, and G. Gigli. Random laser emission from a paper-based device. *J. Mater. Chem. C*, 1:8128–8133, 20132013.

[85] X. Ma, P. Chen, D. Li, Y. Zhang, and D. Yang. Electrically pumped ZnO film ultraviolet random lasers on silicon substrate. *Applied Physics Letters*, 91(25):251109, 2007.

[86] C. Wang, H. Jiang, Y. Li, X. Ma, and D. Yang. Comparison on electrically pumped random laser actions of hydrothermal and sputtered ZnO films. *Journal of Applied Physics*, 114(13):–, 2013.

[87] X.-Y. Liu, C.-X. Shan, S.-P. Wang, Z.-Z. Zhang, and D.-Z. Shen. Electrically pumped random lasers fabricated from ZnO nanowire arrays. *Nanoscale*, 4:2843–2846, 2012.

[88] H. Zhu, C.-X. Shan, J.-Y. Zhang, Z.-Z. Zhang, B.-H. Li, D.-X. Zhao, B. Yao, D.-Z. Shen, X.-W. Fan, Z.-K. Tang, X. Hou, and K.-L. Choy. Low-threshold electrically pumped random lasers. *Advanced Materials*, 22(16):1877–1881, 2010.

[89] V. Folli, N. Ghofraniha, A. Puglisi, L. Leuzzi, and C. Conti. Time-resolved dynamics of granular matter by random laser emission. *Sci. Rep.*, 3:–, July 2013.

[90] H. Cao, Y. G. Zhao, S. T. Ho, E. W. Seelig, Q. H. Wang, and R. P. H. Chang. Random laser action in semiconductor powder. *Phys. Rev. Lett.*, 82:2278–2281, Mar 1999.

[91] V.M. Markushev, M.V. Ryzhkov, Ch.M. Briskina, H. Cao, L.A. Zadorozhnaya, E.I. Givargisov, H. Zhong, S.-W. Wang, and W. Lu. ZnO random laser spectra under nanosecond pumping. *Laser Physics*, 17(9):1109–1118, 2007.

[92] H. Cao, Xunya Jiang, Y. Ling, J. Y. Xu, and C. M. Soukoulis. Mode repulsion and mode coupling in random lasers. *Phys. Rev. B*, 67:161101, Apr 2003.

[93] Q. Baudouin, N. Mercadier, V. Guarrera, W. Guerin, and R. Kaiser. A cold-atom random laser. *Nat Phys*, 9(6):357–360, June 2013.

[94] S. Mujumdar, V. Türck, R. Torre, and D. S. Wiersma. Chaotic behavior of a random laser with static disorder. *Phys. Rev. A*, 76:033807, Sep 2007.

[95] H. E. Türeci, L. Ge, S. Rotter, and A. D. Stone. Strong interactions in multimode random lasers. *Science*, 320(5876):643–646, 2008.

[96] H. E. Türeci, A. D. Stone, L. Ge, S. Rotter, and R. J. Tandy. Ab initio self-consistent laser theory and random lasers. *Nonlinearity*, 22(1):C1, 2009.

[97] C. M. Soukoulis, X. Jiang, J. Y. Xu, and H. Cao. Dynamic response and relaxation oscillations in random lasers. *Phys. Rev. B*, 65:041103, Jan 2002.

[98] S. Heiligenthal, T. Jüngling, O. D'Huys, D. A. Arroyo-Almanza, M. C. Soriano, I. Fischer, I. Kanter, and W. Kinzel. Strong and weak chaos in networks of semiconductor lasers with time-delayed couplings. *Phys. Rev. E*, 88:012902, Jul 2013.

[99] M. Nixon, E. Ronen, A. A. Friesem, and N. Davidson. Observing geometric frustration with thousands of coupled lasers. *Phys. Rev. Lett.*, 110:184102, May 2013.

[100] M.D. Dawson, A.S.L. Gomes, W. Sibbett, and J.R. Taylor. Characterisation of the output from a Q-switched/mode-locked cw Nd:YAG laser. *Optics Communications*, 52(4):295 – 300, 1984.

[101] J. Andreasen, P. Sebbah, and C. Vanneste. Nonlinear effects in random lasers. *J. Opt. Soc. Am. B*, 28(12):2947–2955, Dec 2011.

[102] P. Sebbah and C. Vanneste. Random laser in the localized regime. *Phys. Rev. B*, 66:144202, Oct 2002.

[103] H. Liu, J. Liu, J. Lü, and K. Wang. Spectral time evolution of polarized modes under local pumping in a two-dimensional random medium. *Journal of Optics A: Pure and Applied Optics*, 11(6):065202, 2009.

[104] J. S. Liu, Z. Xiong, and W. Chun. Theoretical investigation on polarization-dependent laser action in two-dimensional random media. *Journal of Optics A: Pure and Applied Optics*, 9(7):658, 2007.

[105] G. P. Agrawal and N. K. Kutta. *Semiconductor lasers*. Van Nostrand Reinhold, 1993.

[106] G. Mie. Beiträge zur Optik trüber Medien, speziell kolloidaler Metallösungen. *Annalen der Physik*, 330(3):377–445, 1908.

[107] S. Boccaletti, V. Latora, Y. Moreno, M. Chavez, and D.-U. Hwang. Complex networks: Structure and dynamics. *Physics Reports*, 424(45):175 – 308, 2006.

[108] F. Bono, E. Gutiérrez, and K. Poljansek. Road traffic: A case study of flow and path-dependency in weighted directed networks. *Physica A: Statistical Mechanics and its Applications*, 389(22):5287 – 5297, 2010.

[109] G. Fagiolo, J. Reyes, and S. Schiavo. The evolution of the world trade web: a weighted-network analysis. *Journal of Evolutionary Economics*, 20(4):479–514, 2010.

[110] R. Albert and A.-L. Barabási. Statistical mechanics of complex networks. *Rev. Mod. Phys.*, 74:47–97, Jan 2002.

[111] J.-P. Onnela, J. Saramäki, J. Kertész, and K. Kaski. Intensity and coherence of motifs in weighted complex networks. *Phys. Rev. E*, 71:065103, Jun 2005.

[112] S. N. Dorogovtsev, A. V. Goltsev, and J. F. F. Mendes. Critical phenomena in complex networks. *Rev. Mod. Phys.*, 80:1275–1335, Oct 2008.

[113] D. R. Nelson. Order, frustration, and defects in liquids and glasses. *Phys. Rev. B*, 28:5515–5535, Nov 1983.

[114] D. Felbacq, G. Tayeb, and D. Maystre. Scattering by a random set of parallel cylinders. *J. Opt. Soc. Am. A*, 11(9):2526–2538, Sep 1994.

[115] A. Goetschy and S. E. Skipetrov. Euclidean matrix theory of random lasing in a cloud of cold atoms. *EPL (Europhysics Letters)*, 96(3):34005, 2011.

[116] M. Höfner, B. Kobin, S. Hecht, and F. Henneberger. Strong coupling and laser action of ladder-type oligo(p-phenylene)s in a microcavity. *ChemPhysChem*, 15(17):3805–3808, 2014.

[117] J. Wainstain, C. Delalande, D. Gendt, M. Voos, J. Bloch, V. Thierry-Mieg, and R. Planel. Dynamics of polaritons in a semiconductor multiple-quantum-well microcavity. *Phys. Rev. B*, 58:7269–7278, Sep 1998.

[118] T. Schwartz, J. A. Hutchison, C. Genet, and T. W. Ebbesen. Reversible switching of ultrastrong light-molecule coupling. *Phys. Rev. Lett.*, 106:196405, May 2011.

[119] D. G. Lidzey, D. D. C. Bradley, M. S. Skolnick, T. Virgili, S. Walker, and D. M. Whittaker. Strong exciton-photon coupling in an organic semiconductor microcavity. *Nature*, 395(6697):53–55, September 1998.

[120] R.J. Holmes and S.R. Forrest. Strong exciton-photon coupling in organic materials. *Organic Electronics*, 8(23):77 – 93, 2007. Coupled States of Excitons, Photons, and Plasmons in Organic Structures.

[121] R. F. Oulton, N. Takada, J. Koe, P. N. Stavrinou, and D. D. C. Bradley. Strong coupling in organic semiconductor microcavities. *Semiconductor Science and Technology*, 18(10):S419, 2003.

[122] V.M. Agranovich and G.C. La Rocca. Electronic excitations in organic microcavities with strong lightmatter coupling. *Solid State Communications*, 135(910):544 – 553, 2005. Fundamental Optical and Quantum Effects in Condensed Matter.

[123] Y. Wei, J. S. Lauret, L. Galmiche, P. Audebert, and E. Deleporte. Strong exciton-photon coupling in microcavities containing new fluorophenethylamine based perovskite compounds. *Opt. Express*, 20(9):10399–10405, Apr 2012.

[124] J. D. Plumhof, T. Stöferle, L. Mai, U. Scherf, and R. F. Mahrt. Room-temperature Bose-Einstein condensation of cavity exciton-polaritons in a polymer. *Nat Mater*, 13(3):247–252, March 2014.

[125] K. S. Daskalakis, S. A. Maier, R. Murray, and S. Kéna-Cohen. Nonlinear interactions in an organic polariton condensate. *Nat Mater*, 13(3):271–278, March 2014.

[126] D. Snoke and P. Littlewood. Polariton condensates. *Physics Today*, 63:42, 2010.

[127] S. Kena-Cohen and Forrest S. R. Room-temperature polariton lasing in an organic single-crystal microcavity. *Nat Photon*, 4(6):371–375, June 2010.

[128] S. Christopoulos, G. Baldassarri Höger von Högersthal, A. J. D. Grundy, P. G. Lagoudakis, A. V. Kavokin, J. J. Baumberg, G. Christmann, R. Butté, E. Feltin, J.-F. Carlin, and N. Grandjean. Room-temperature polariton lasing in semiconductor microcavities. *Phys. Rev. Lett.*, 98:126405, Mar 2007.

[129] P. Bhattacharya, T. Frost, S. Deshpande, M. Z. Baten, A. Hazari, and A. Das. Room temperature electrically injected polariton laser. *Phys. Rev. Lett.*, 112:236802, Jun 2014.

[130] H. Deng, G. Weihs, D. Snoke, J. Bloch, and Y. Yamamoto. Polariton lasing vs. photon lasing in a semiconductor microcavity. *Proceedings of the National Academy of Sciences*, 100(26):15318–15323, 2003.

[131] L. Orosz, F. Réveret, F. Médard, P. Disseix, J. Leymarie, M. Mihailovic, D. Solnyshkov, G. Malpuech, J. Zuniga-Pérez, F. Semond, M. Leroux, S. Bouchoule, X. Lafosse, M. Mexis, C. Brimont, and T. Guillet. LO-phonon-assisted polariton lasing in a ZnO-based microcavity. *Phys. Rev. B*, 85:121201, Mar 2012.

[132] D. Xu, W. Xie, W. Liu, J. Wang, L. Zhang, Y. Wang, S. Zhang, L. Sun, X. Shen, and Z. Chen. Polariton lasing in a ZnO microwire above 450K. *Applied Physics Letters*, 104(8):–, 2014.

[133] T.-C. Lu, Y.-Y. Lai, Y.-P. Lan, S.-W. Huang, J.-R. Chen, Y.-C. Wu, W.-F. Hsieh, and H. Deng. Room temperature polariton lasing vs. photon lasing in a ZnO-based hybrid microcavity. *Opt. Express*, 20(5):5530–5537, Feb 2012.

[134] V. Bulovi, V. G. Kozlov, V. B. Khalfin, and S. R. Forrest. Transform-limited, narrow-linewidth lasing action in organic semiconductor microcavities. *Science*, 279(5350):553–555, 1998.

[135] R. Schmidt-Grund, B. Rheinländer, C. Czekalla, G. Benndorf, H. Hochmuth, M. Lorenz, and M. Grundmann. Exciton-polariton formation at room temperature in a planar ZnO resonator structure. *Applied Physics B*, 93(2-3):331–337, 2008.

[136] C. Sturm, H. Hilmer, R. Schmidt-Grund, and M. Grundmann. Observation of strong excitonphoton coupling at temperatures up to 410k. *New Journal of Physics*, 11(7):073044, 2009.

[137] F. Médard, D. Lagarde, J. Zúñiga-Pérez, P. Disseix, M. Mihailovic, J. Leymarie, E. Frayssinet, J. C. Moreno, F. Semond, M. Leroux, and S. Bouchoule. Influence of the excitonic broadening on the strong light-matter coupling in bulk zinc oxide microcavities. *Journal of Applied Physics*, 108(4):–, 2010.

[138] Feng Li, L. Orosz, O. Kamoun, S. Bouchoule, C. Brimont, P. Disseix, T. Guillet, X. Lafosse, M. Leroux, J. Leymarie, M. Mexis, M. Mihailovic, G. Patriarche, F. Réveret, D. Solnyshkov, J. Zuniga-Perez, and G. Malpuech. From excitonic to photonic polariton condensate in a ZnO-based microcavity. *Phys. Rev. Lett.*, 110:196406, May 2013.

[139] J.-R. Chen, T.-C. Lu, Y.-C. Wu, S.-C. Lin, W.-F. Hsieh, S.-C. Wang, and H. Deng. Characteristics of exciton-polaritons in ZnO-based hybrid microcavities. *Opt. Express*, 19(5):4101–4112, Feb 2011.

[140] P. Kelkar, V. Kozlov, H. Jeon, A. V. Nurmikko, C.-C. Chu, D. C. Grillo, J. Han, C. G. Hua, and R. L. Gunshor. Excitons in a ii-vi semiconductor microcavity in the strong-coupling regime. *Phys. Rev. B*, 52:R5491–R5494, Aug 1995.

[141] H. Abassi, S. Jaziri, and R. Bennaceur. Hybrid excitons in organicinorganic semiconducting quantum wells in a microcavity. *Physica E: Low-dimensional Systems and Nanostructures*, 7(34):686 – 692, 2000.

[142] T. Fujita, Y. Sato, T. Kuitani, and T. Ishihara. Tunable polariton absorption of distributed feedback microcavities at room temperature. *Phys. Rev. B*, 57:12428–12434, May 1998.

[143] L. G. Connolly, D. G. Lidzey, R. Butt, A. M. Adawi, D. M. Whittaker, M. S. Skolnick, and R. Airey. Strong coupling in high-finesse organic semiconductor microcavities. *Applied Physics Letters*, 83(26):5377–5379, 2003.

[144] G. Lanty, S. Zhang, J. S. Lauret, E. Deleporte, P. Audebert, S. Bouchoule, X. Lafosse, J. Zuñiga Pérez, F. Semond, D. Lagarde, F. Médard, and J. Leymarie. Hybrid cavity polaritons in a ZnO-perovskite microcavity. *Phys. Rev. B*, 84:195449, Nov 2011.

[145] M. Slootsky, X. Liu, V. M. Menon, and S. R. Forrest. Room temperature Frenkel-Wannier-Mott hybridization of degenerate excitons in a strongly coupled microcavity. *Phys. Rev. Lett.*, 112:076401, Feb 2014.

[146] S. Halm, S. Kalusniak, S. Sadofev, H.-J. Wünsche, and F. Henneberger. Strong exciton-photon coupling in a monolithic ZnO/(Zn,Mg)O multiple quantum well microcavity. *Applied Physics Letters*, 99(18):181121, 2011.

[147] H. de Vries and D. A. Wiersma. Homogeneous bradening of optical transitions in organic mixed crystals. *Phys. Rev. Lett.*, 36(2):91, 1975.

[148] R. Houdré, R. P. Stanley, and M. Ilegems. Vacuum-field rabi splitting in the presence of inhomogeneous broadening: Resolution of a homogeneous linewidth in an inhomogeneously broadened system. *Phys. Rev. A*, 53:2711–2715, Apr 1996.

[149] R. Schmidt-Grund, B. Rheinländer, C. Czekalla, G. Benndorf, H. Hochmuth, M. Lorenz, and M. Grundmann. Exciton-polariton formation at room temperature in a planar ZnO resonator structure. *Applied Physics B*, 93(2-3):331–337, 2008.

[150] N. Bachelard, J. Andreasen, S. Gigan, and P. Sebbah. Taming random lasers through active spatial control of the pump. *Phys. Rev. Lett.*, 109:033903, Jul 2012.

[151] M. Born and E. Wolf. *Principles of Optics*. Pergamon Press, 1959.

List of publications

Parts of this work have already been published in the following articles:

- M. Höfner, H.-J. Wünsche and F. Henneberger, *A random laser as a dynamical network*, New Journal of Physics, 16, 033002, 2014
- M. Höfner, B. Kobin, S. Hecht and F. Henneberger, *Strong Coupling and Laser Action of Ladder-Type Oligo(p-phenylene)s in a Microcavity*, ChemPhysChem, 15, 3805–3808, 2014
- M. Höfner, S. Sadofev, B. Kobin, S. Hecht and F. Henneberger, *Hybrid Polaritons in a Resonant Inorganic/Organic Semiconductor Microcavity*, submitted to Appl. Phys. Lett.

Other publications:

- M. Grehn, T. Seuthe, M. Höfner, N. Griga, C. Theiss, A. Mermillod-Blondin, M. Eberstein and H. J. Eichler, *Femtosecond-laser induced ablation of silicate glasses and the intrinsic dissociation energy*, Optics Materials Express, 4 , 689–700, 2014
- M. Grehn, T. Seuthe, F. Reinhardt, M. Höfner, N. Griga, M. Eberstein and J. Bonse, *Debris of potassium-magnesium silicate glass generated by femtosecond laser-induced ablation in air: An analysis by near edge X-ray absorption spectroscopy, micro Raman and energy dispersive X-ray spectroscopy*, Applied Surface Science, 302, 286–290, 2014
- M. Grehn, T. Seuthe, W. J. Tsai, M. Höfner, A. W. Achtstein, A. Mermillod-Blondin, M. Eberstein, H. J. Eichler and J. Bonse, *Nonlinear absorption and refraction of binary and ternary alkaline and alkaline earth silicate glasses*, Optics Materials Express, 3, 2132-2140, 2013
- T. Seuthe, M. Höfner, F. Reinhardt, W. J. Tsai, J. Bonse, M. Eberstein, H. J. Eichler and M. Grehn, *Femtosecond laser-induced modification of potassium-magnesium silicate glasses: An analysis of structural changes by near edge x-ray absorption spectroscopy*, Appl. Phys. Lett., 100, 224101, 2012
- S. Mahdi, M. Grehn, A. Al-Saadi, M. Höfner, S. Meister and H. J. Eichler, *Facet Preparation of Silicon Nano-waveguides by Cleaving the SOI chip*, Journal of Nonlinear Optical Physics and Materials, 20, 509-523, 2011

- S. Mahdi, M. Grehn, S. Meister, D. Ashkenasi and M. Höfner, *Smooth Surfaces with High Accuracies*, Laser Technik Journal, 9, 36-39, 2012

Talks and posters:

- Talk: *A random laser as a dynamical network*, Workshop on Nonlinear Dynamics in Semiconductor Lasers, Weierstrass Institute for Applied Analysis and Stochastics, Berlin, May 2014
- Talk: *A random laser as a network*, IRTG 1740 Workshop/School, Berlin, September 2013
- Talk: *Strong coupling and lasing of a ladder-type quarterphenyl*, III. Workshop and School on Dynamics, Transport and Control in Complex Networks, São José dos Campos, October 2014
- Poster: *Strong coupling and lasing in ladder-type oligo(p-phenylene)s*, Symposium on hybrid inorganic/organic systems for optoelectronics, Berlin, February 2015

Acknowledgement

At first I like to thank Prof. Dr. Fritz Henneberger for giving me the opportunity to do my PhD in his group. I like to thank him for his support and scientific input. After he suddenly passed away in February 2015, Prof. Dr. Oliver Benson took over the supervision of my work. I want to thank him for making it possible that I could finish my PhD with his support. Prof. Dr. Tiago Pereira I like to thank for his interest and discussion of my work.

I like to especially thank Priv. Doz. Dr. H.-J. Wünsche, his continued support throughout my entire PhD time was essential. His kind supervision in all matters was a great help and I like to thank him further for all scientific and non-scientific discussions.

I further like to thank Dr. Sergey Sadofev for the excellent ZnO based samples and his support in all scientific areas. I am very grateful to Dr. Björn Kobin for his work on the organic molecule, which is a core material of the investigated structures, and for his help and comments in the preparation of the manuscripts. In this context I also like to thank Elfriede Renger for her support in the fabrication of the dielectric mirrors.

I further like to thank everyone, who somehow contributed to my work:

- Dr. Joachim Puls for his support in all experimental matters and the scientific discussions.
- Dr. Sascha Kalusniak for the help in the experiments especially in the beginning of my PhD time.
- Dr. Sylke Blumstengel for her support in the last months.
- Dr. Simon Halm for giving me a deeper understanding of the physics of microcavities.
- Dr. Alexander Kuznetsov for all scientific and nonscientific discussion in our office.
- Dr. Matthias Brandt for the commissioning of the electron beam evaporator.
- My PhD colleagues Francesco Bianchi, Mino Sparenberg, Moritz Eyer and Jungtaek Kim for scientific discussion and general support.
- The student workers in my project Moritz Stange and Kristina Komander for their support in measurements and quality control.
- Christian Kremer for his support in all technical issues.

- All other members of the Photonics group Dr. Peter Schäfer, Dr. Maurizio Roczen, Dagmar Fahnauer, Dr. Nils Ritter and Beatrix Matthes.
- All my colleagues from the IRTG 1740 for the nice times at the workshops and especially Prof. Dr. Jürgen Kurths and David Hansmann for their general support.
- My friends who took the time to read and comment on this manuscript Thomas Wörner, Alfred Dworazik and Florian Eschenbacher.

A very special thanks goes to my family for their general support, which was crucial to my work.

THANK YOU!

Selbständigkeitserklärung

Ich erkläre, dass ich die Dissertation selbständig und nur unter Verwendung der von mir gemäß §7 Abs. 3 der Promotionsordnung der Mathematisch-Naturwissenschaftlichen Fakultät, veröffentlicht im Amtlichen Mitteilungsblatt der Humboldt-Universität zu Berlin Nr. 126/2014 am 18.11.2014 angegebenen Hilfsmittel angefertigt habe.

Ich habe mich nicht anderwärts um einem Doktorgrad im Promotionsfach Physik beworben und besitze keinen Doktorgrad im Promotionsfach Physik.

Die Promotionsordnung der Mathematisch-Naturwissenschaftlichen Fakultät, veröffentlicht im Amtlichen Mitteilungsblatt der Humboldt-Universität zu Berlin Nr. 126/2014 am 18.11.2014 habe ich zur Kenntnis genommen.

Michael Höfner